

# **VICINAL SURFACES AS NANOSCOPIC ECHELETTE GRATINGS FOR ATOMIC WAVES AND THEIR APPLICATION TO He-SURFACE SPECTROSCOPY**

THÈSE N° 1364 (1995)

PRÉSENTÉE AU DÉPARTEMENT DE PHYSIQUE

ÉCOLE POLYTECHNIQUE FÉDÉRALE DE LAUSANNE

POUR L'OBTENTION DU GRADE DE DOCTEUR ÈS SCIENCES

PAR

**HANSJÖRG SCHIEF**

Physicien diplômé de l'Université de Göttingen  
de nationalité allemande

acceptée sur proposition du jury:

Prof. K. Kem, rapporteur  
Prof. R. Monol, corapporteur  
Prof. B. Poelsema, corapporteur  
Prof. J.-P. Toennies, corapporteur

Lausanne, EPFL  
1995

## Résumé

La surface vicinale Pt(997) est introduite en tant que réseau de réflexion nanoscopique à haute performance pour les ondes atomiques. Ses propriétés d'optique atomique, vis-à-vis de faisceaux d'hélium thermiques, sont établies grâce à une étude détaillée de la diffraction d'hélium à haute résolution. Ces propriétés peuvent essentiellement être décrites par analogie avec la diffraction classique de la lumière par des réseaux échelle. Seuls les canaux de diffraction proches de la direction spéculaire des terrasses sont ouverts. Si le faisceau diffracté correspondant à un ordre de diffraction  $n$  ( $n \neq 0$ ) donné est amené à coïncider avec la direction spéculaire des terrasses, la presque totalité de l'intensité réfléchie est concentrée dans cet *unique* ordre de diffraction. Dans ce cas, la surface Pt(997) se comporte comme un analyseur -ou monochromateur- parfait pour les ondes d'hélium. L'efficacité absolue correspondante, c'est-à-dire le rapport entre le nombre d'atomes collectés et le flux incident, varie entre 2% et 20%, selon l'énergie du faisceau et l'ordre de diffraction. Cette valeur est supérieure d'au moins un ordre de grandeur à l'efficacité de toute surface cristalline ionique ou métallique, de faible indice. Afin de permettre une utilisation prolongée fiable et confortable de la surface Pt(997) sous des conditions UHV conventionnelles, un procédé de nettoyage auto-catalytique permanent sous atmosphère mixte oxygène/hydrogène, à 750 K, a été développé. Ainsi, sans autre forme de préparation, la surface Pt(997) peut être utilisée de façon routinière durant plusieurs semaines, sans perte d'intensité significative.

Les données de diffraction d'hélium ont été obtenues à l'aide d'un spectromètre hélium-surface à double axe entièrement original, conçu et réalisé durant cette thèse. Dans ce montage, l'énergie des atomes d'hélium diffusés inélastiquement est analysée par diffraction sur un réseau échelle nanoscopique, en lieu et place de la technique de temps de vol couramment utilisée dans ce but. Afin de tirer tout le profit possible des avantages fournis par un spectromètre à cristale, une multitude de possibilités de balayages angulaires à haute résolution indépendants, sur les deux surfaces, ont été réalisées. Par exemple, l'angle de diffusion sur la surface cible peut être varié entre  $59^\circ$  et  $181^\circ$ , sans rupture du vide. Les balayages angulaires à haute

résolution sur la surface analysatrice sont contrôlés à l'aide d'un système de positionnement spécialement conçu pour la compatibilité UHV. Celui-ci assure une reproductibilité absolue meilleure que  $0.01^\circ$ .

Comme première étape vers l'utilisation systématique de réseaux échelle nanoscopiques dans l'optique atomique et la diffusion d'hélium, un tel réseau a été employé pour la monochromatisation d'ondes d'hélium. Un faisceau légèrement polychromatique ( $\Delta\lambda/\lambda > 1.3\%$ ) est diffusé par le monochromateur; un diaphragme en aval de celui-ci sélectionne un faisceau d'énergie donnée, qui est ensuite analysé par balayage à haute résolution sur la seconde surface. Cette expérience est l'analogue contemporain de l'expérience historique de double diffusion de Stern et Estermann. La monochromatisation résulte en un rétrécissement prononcé des pics de diffraction. L'étude quantitative de ce phénomène requiert une analyse théorique détaillée du processus de double diffusion du faisceau d'hélium. A cette fin, une description de la diffusion multiple dans une expérience de jet moléculaire a été développée, faisant usage du formalisme de l'optique matricielle. Dans la géométrie présente, une monochromatisation active de  $\Delta\lambda/\lambda = 0.6\%$  est réalisée. Des améliorations sont prévues, qui abaisseront cette valeur en-deçà de 1%.

## Abstract

The vicinal Pt(997) surface is introduced as high performance nanoscopic reflection grating (echelette grating) for atomic waves. Its atom-optical properties with respect to thermal He-beams are established by a detailed high resolution diffraction study. They can largely be described in analogy to light diffraction from blazed gratings in classical optics. Only diffraction channels in the close vicinity of the terrace specular direction are open. If the diffracted beam of a certain diffraction order  $n$  is made to coincide with the specular direction of the terraces, almost the total reflected intensity can be concentrated in one single higher diffraction order. Under this condition the Pt(997) surface acts as almost perfect analyser or monochromator for He-waves. The corresponding absolute efficiency, i. e. the amount of collected atoms within one higher diffraction order with respect to the incoming flux, varies between 2% and 20% depending on the beam energy and the diffraction order. It is, thus, at least one order of magnitude larger than the efficiency of any low index ionic or metal crystal surfaces. In order to provide a reliable long-time and comfortable use of the Pt(997) surface under standard UHV conditions a permanent auto-catalytic cleaning procedure at 750 K in a mixed oxygen/hydrogen atmosphere has been developed. The Pt(997) surface can routinely be used during several weeks without any significant intensity loss and without further surface preparation.

The He-diffraction data have been obtained with a completely new He-surface double axis spectrometer that has been designed and constructed during this thesis. In this apparatus the energy analysis of inelastically scattered He-atoms is done by diffraction from a nanoscopic echelette grating, instead of measuring the atom flight velocity as it is done in well established He-surface time-of-flight spectrometers. In order to make full use of the advantages of a crystal spectrometer multiple possibilities of independent high resolution angle scans at the target and at the analyser surface have been realised. For example, the scattering angle at the target can be varied between  $59^\circ$  and  $181^\circ$  with an absolute angular resolution better than  $0.01^\circ$  and without breaking the vacuum. The high resolution

angular scans with the analyser surface are controlled and measured by means of a specially designed UHV compatible positioning system. It again provides an absolute reproducibility better than  $0.01^\circ$ .

As a first steps towards a systematic use of nanoscopic echelette gratings in atom optics and He-surface spectroscopy they have been employed for an active monochromatization of He-waves. A slightly polychromatic beam ( $\Delta\lambda/\lambda > 1.3\%$ ) is scattered of the monochromator. An aperture behind the monochromator skims an energy selected beam which is then analysed by high resolution diffraction scans from a second analyser surface. This experiment is the modern analogue to the classic double scattering experiment of Stern and Estermann. Monochromatization results in a pronounced diffraction peak narrowing. The quantitative analysis of the peak narrowing requires a detailed theoretical analysis of the double-surface scattering event of the He-beam. Therefore, a matrix-optics description of multiple surface scattering in molecular beam experiments has been developed. In the present geometry an active monochromatization of  $\Delta\lambda/\lambda = 0.6\%$  is achieved. Further improvements will drop the resolution below  $1\%$ .

## Table of contents

<b>1</b>	<b>Introduction</b>	<b>1</b>
<b>2</b>	<b>He-surface spectroscopy using dispersive surface gratings</b>	<b>5</b>
2.1	Principles of He-surface spectroscopy	5
2.2	Nanoscopic echelette gratings: concept versus reality	15
2.2.1	The concept of nanoscopic echelette gratings	15
2.2.2	The vicinal Pt(997) surface	19
2.2.3	High resolution He-diffraction from Pt(997)	23
2.3	Mode of operation of Pt(997) echelette gratings	37
2.4	Theoretical energy resolution of Pt(997) echelette gratings	41
2.4.1	Resolution of a Pt(997) monochromator	41
2.4.2	A matrix-optics like description of multi-surface scattering	48
2.4.3	The analyser energy resolution	53
<b>3</b>	<b>Construction of the novel He-surface double axis spectrometer</b>	<b>55</b>
3.1	Introduction and objectives	55
3.2	The vacuum system	60
3.2.1	The beam source	60
3.2.2	The scattering chamber	61
3.2.3	The analyser chamber	62
3.2.4	The detector unit	64
3.3	Scanning possibilities at the sample and the analyser	66
3.3.1	Scattering chamber rotation and detector rotation	66
3.3.2	Ultra high resolution sample positioning in UHV	74
3.3.3	Outlook	85
3.4	Apparatus characteristics	88
3.4.1	He-beam characteristics	88

	3.4.2 Spectrometer resolution in inelastic experiments	92
3.5	Surface and system preparation	94
4	<b>Pt(997) (and Pt(111)) as atom-optical device</b>	99
4.1	The Pt(997) analyser dynamics	99
4.2	The analyser resolution	102
4.3	Consequences of the finite terrace width distribution	104
4.4	Consequences of crystal imperfections	107
4.5	Chemical passivation of Pt(997) and Pt(111)	111
	4.5.1 Hydrogen passivation of Pt(997)	111
	4.5.2 Catalytic passivation of Pt(997)	116
	4.5.3 Hydrogen passivation of Pt(111)	119
	4.5.4 Catalytic passivation of Pt(111)	121
4.6	Absolute efficiency of the Pt(997) echelette grating	123
5	<b>Monochromatization of supersonic He nozzle beams by diffraction</b>	135
5.1	Monochromatization demonstrated with a p(2x2) O/Pt(111) analyser surface	139
5.2	Monochromatization demonstrated with a Pt(997) analyser	148
6	<b>Outlook</b>	155
7	<b>References</b>	157
8	<b>Appendix A</b>	165

## 1 Introduction

Beginning with the pioneering work of O. Stern in the 1920's, atomic and molecular beam methods have evolved into an important tool in many physical and chemical research fields [Sco88]. Supersonic nozzle beams with small velocity spreads are now routinely used in atom- and molecular-physics, cluster physics and surface science. Despite major experimental differences the main object remains similar. The beam is furnished by a nozzle and then directly examined or examined after having interacted with electro-magnetic fields, electrons, gaseous matter or solid surfaces. Among the most commonly analysed beam properties are the constituting beam particles and their velocity distribution. They are mainly determined by mass selecting ionisation detection or by spectroscopic detection methods. Thereby the velocity measurements are either provided by mechanical velocity filters or by different time-of-flight (TOF) methods. All the above mentioned methods make use of the particle properties belonging to the quantum-mechanical objects under consideration.

However, according to the de-Broglie relation  $p = h/\lambda$  the beam we wish to investigate may also be considered as a material wave. It is worth exploiting these wave-properties for an atom-optical manipulation and characterisation of atomic and molecular beams, since this could reveal additional beam characteristics that are not visible using only particle properties. Employing the wave properties for an analysis and state selection of molecular beams can thus be considered as an important application of atom optics that is currently becoming an exciting new field in fundamental physics [Ada94]. For example, recent experiments by Carnal



et al. [Car91a] demonstrated that it is possible to focus an atomic beam by diffraction from transmission Fresnel zone plates . Atom diffraction from free-standing line gratings has also been reported [Kei88, Kei91, Car91b] . The latter has recently been used by Schöllkopf and Toennies for a detailed characterisation of molecular beams by diffraction [Sch94]. They studied the diffraction from He-cluster beams to solve the intriguing question whether or not He-dimers exist in a He-cluster beam. This question could only hardly be answered by means of mass spectroscopy [Luo93, Azi91], because of the inherent dissociation process upon ionisation. The diffraction study, however, clearly demonstrated the existence of the He-dimer by revealing diffraction peaks that can only be assigned to the de-Broglie wavelength of He<sub>2</sub>. In addition the authors demonstrated that diffraction can be used for an active spatial selection of He-cluster beams that only contain one cluster species.

From this and other examples [Mar88, Car92, Pfa93, Sch95] one expects that diffraction techniques in molecular beam experiments will become as important as in classical light optics. The successfulness of atom optics crucially depends on the quality of the corresponding atom optical devices. Typical de-Broglie wavelengths of molecular beam particles are in the range of 0.1 Å to 2 Å requiring the use of challenging nano-structured devices.

In this thesis, high performance nanoscopic echelette gratings, i.e. stepped reflection gratings, for atomic and molecular beams with a certain emphasise on thermal He atom beams are introduced. They allow the analysis and active monochromatization of He atom waves within a novel kind of He-surface double (triple) axis spectrometer.

He-surface scattering which provides information on surface structure and surface dynamics became a powerful tool during the past 15 years due to the

development of monochromatic nozzle beam sources and high performance TOF techniques for energy resolved measurements [Hul92]. Nevertheless, a substantial increase in energy resolution is still necessary in order to approach new physical problems. This requires an active monochromatization of the He-beam and an improved energy analysis of the detection system. Both can hardly be achieved with standard mechanical velocity filters [Hah90] and state-of-the-art TOF detectors [Doa89]. Therefore it has been proposed [Kuh92] to use diffraction from vicinal metal surfaces for an active monochromatization and energy analysis of He beams within a novel Helium-surface triple axis spectrometer. The basic idea of this method, however, refers to the early work of Stern and collaborators. Using He-atom diffraction from LiF surfaces they did not only demonstrate the reality of de-Broglie waves associated with material particles [Est30] but they could also perform active monochromatization of their effusive He beams [Est31]. More than 50 years later Mason and Williams used again LiF surfaces as energy dispersive gratings for inelastic He-surface spectroscopy [Mas78]. But this method was not able to compete with TOF apparatus that came to its own at that time [Bru81]. The main disadvantage of the double axis spectrometer built by Mason and Williams was the use of LiF surfaces that are inappropriate as atom-optical devices which require high reflectivities into higher order diffraction channels. A successful use of He-beam monochromators and analysers in a He-surface spectrometer therefore requires the development of well suited atom-optical diffraction gratings with high reflectivities that can easily be used over long periods under standard UHV conditions.

In Sec. 2.1 of this thesis the main properties of He-surface scattering using the TOF method and dispersive diffraction gratings are discussed. In Sec. 2.2 the concept of nanoscopic echelette gratings based on stepped vicinal metal

surfaces is introduced and confirmed by high resolution He-diffraction measurements. The theoretical description of the energy resolution of surface gratings in molecular beam experiments is discussed in Sec. 2.3 and Sec. 2.4. Sec. 3 is dedicated to the description of the experimental details of our new He-surface double axis spectrometer. In Sec. 4 the special atom-optical properties of Pt(997) and Pt(111) surfaces are presented. Finally, it will be demonstrated in Sec. 5 that nanoscopic echelette gratings can be used for an active monochromatization of already highly monochromatic supersonic He nozzle beams.

## 2 He-surface spectroscopy using dispersive surface gratings

### 2.1 Principles of He-surface spectroscopy

Thermal Helium atoms ( $E < 100$  meV) are generally considered to be the ideal probe particle in a non-destructive scattering experiment in surface physics. Due to their large cross-section they only interact with the outermost layer of a solid surface. No penetration into deeper layers occurs and the classical turning point of thermal energy atoms is usually a few ångströms above the ion cores of the outermost layer. Therefore the scattered atoms only contain information about the surface properties of the solid sample under consideration. Additionally the wavelength of thermal He-atoms matches with typical interatomic distances at surfaces giving rise to interference effects in the scattering process. This is used in pure elastic diffraction experiments for the structural investigation of crystal surfaces [Eng82] and surface defects [Poe89], for the investigation of surface phase transitions [Ker89] and in studies of crystal growth [Mig88]. On the other hand inelastic He-scattering can be used for the investigation of the dynamics of surface vibrations [Toe87] and surface diffusion [Fren92], since the dispersion relation of free Helium atoms overlaps with the dispersion relations of collective excitations and atomic movements at the surface.

Modern state-of-the-art inelastic experiments are exclusively done by means of the TOF technique illustrated in Fig. 2.1.1. A highly monochromatic ( $\Delta\lambda/\lambda < 1\%$ ) thermal He beam ( $E = 5 - 100$  meV) is produced in a nozzle source and directed towards the target where it scatters off. The atoms scattered into a well defined solid angle element  $\Omega$  are measured energy revolved by chopping the beam into short pulses and determining the total

flight time between the chopper and the electron impact ionisation mass detector.

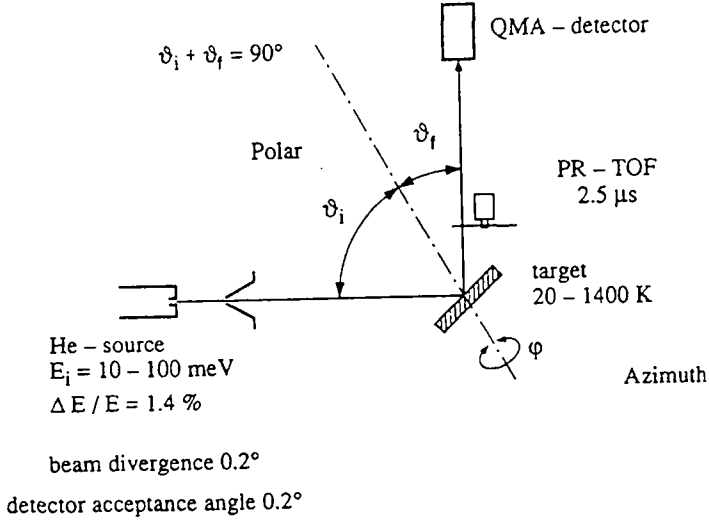


Fig. 2.1.1 : Schematic experimental set-up of a TOF He-surface spectrometer (from [Kuh92]).

Since the primary beam energy and the scattering geometry are known, the energy transfer and the momentum transfer parallel to the surface is straightforwardly determined from the conservation of energy  $\Delta E = E_f - E_i = \hbar\omega$  and parallel wave vector  $\Delta K = K_f - K_i$ . In the case of in-plane scattering, i. e. the target surface is perpendicular with respect to the plane defined by the incoming and outgoing beam, the relation between the

energy and the momentum transfer for the atom-surface scattering process is described by the scancurve

$$\Delta E = E_i \left[ \left( \frac{\sin(\vartheta_i) + \Delta K / k_i}{\sin(\vartheta_f)} \right)^2 - 1 \right] \quad (2.1.1)$$

where  $E_i$  is the primary beam energy and  $\vartheta_i$  and  $\vartheta_f$  denote the angles of the incoming and outgoing beam with respect to the surface normal ( $k_i = \sqrt{2m_{He}E_i} / \hbar$  is the wavevector of the incoming He-atoms).

The energy resolution of a TOF-spectrometer is limited to  $\Delta E/E \sim 2\%$  by the following main contributions to the time spread at the detector [Smi88] : the monochromaticity of the primary beam, the shutter function of the beam chopper, the finite length of the ionisation region and the length of the flight path.

A significant improvement of the energy resolution requires a simultaneous improvement in all these contributions. Whereas the influence of the flight path and the finite length of the ioniser can easily be diminished by increasing the flight path, neither the chopper resolution nor the monochromaticity of the primary beam can easily be increased. Especially an increase of the primary beam monochromaticity is almost impossible. The velocity spread of He nozzle beams at a given nozzle temperature is roughly determined by the product of the nozzle orifice diameter  $D$  multiplied with the stagnation pressure  $P$  [Toe87]. Typical nozzle orifice diameters are 10  $\mu\text{m}$ . Depending on the nozzle temperature stagnation pressures between a few bars at very low temperatures and up to 300 bar at room temperature can be used. Increasing the value of  $D \cdot P$  does not further improve the monochromaticity due to intrinsic limitations imposed by cluster formation [Ker85]. Since condensation roughly scales with  $P^2 \cdot D$  it is in principle possible to achieve smaller velocity spreads by

using lower pressures at greater nozzle diameters. But the nozzle throughput scales with  $P \cdot D^2$  and therefore insurmountable technological problems due to pumping speed limitations arise. This problems can only be solved by using pulsed nozzles [Wan88] which are rather difficult to handle.

A completely different way to increase the monochromaticity of He nozzle beams is provided by actively skimming a selected velocity interval out of the velocity distribution of the nozzle beams. A straightforward solution for this active monochromatization would be the use of mechanical velocity filters, consisting of rotating discs, as they are widely used in various molecular beam or neutron physics experiments [Mei88]. A detailed analysis shows, however, that velocity selectors which provide a velocity spread of  $\Delta v/v = 0.1\%$  are not suitable [Hah90]. A thin blade selector would require a length of more than 1 m, while a thick-blade selector can be as short as 10 cm but at a price of a transmission coefficient which is of the order of one per mille.

Using solid surfaces as grating monochromators is a more promising concept of active monochromatization of He waves. Fig. 2.1.2 demonstrates the application of surface gratings as monochromator and analyser within a hypothetical He-surface triple axis spectrometer. The polychromatic He beam is scattered off a monochromator surface. Atoms with different de-Broglie wavelengths are diffracted in different directions. An aperture behind the monochromator skims an energy selected beam which is further directed towards the target where it can undergo various elastic and inelastic scattering events. The energy distribution of the outgoing beam is then analysed by performing diffraction scans from the analyser surface. It is worth mentioning that He-surface triple axis spectroscopy directly

corresponds to spectrometers in classical light optics using reflection gratings [Ber78]. It is also in close analogy to neutron triple axis spectrometry [Mon83] and inelastic x-ray scattering experiments [Bur87].

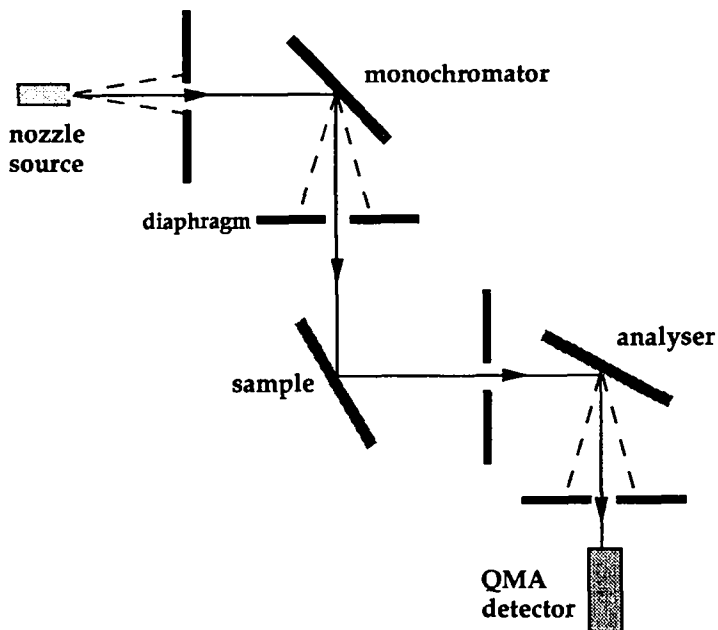


**Fig. 2.1.2** : Schematical experimental set-up of a He-surface triple axis spectrometer.

The energy resolution of a He-surface triple axis spectrometer is entirely determined by its geometry and the mosaic spreads of the monochromator and the analyser surface. A first rough estimation of the resolution can be obtained from the one-dimensional Bragg equation



$$n\lambda = d \cdot (\sin(\nu_f) - \sin(\nu_i)) \quad , \quad (2.1.2)$$

where  $d$  is the surface lattice periodicity. Expanding equation (2.1.2) reveals a relation between the finite velocity spread  $\frac{\Delta v}{v} = \frac{\Delta \lambda}{\lambda}$  and the dispersion smearing  $\Delta \nu_f$ .

$$\frac{\Delta \lambda}{\lambda} = \frac{\cos(\vartheta_f)}{n\lambda} \cdot d \cdot \Delta \vartheta_f \quad . \quad (2.1.3)$$

The value of  $\Delta \nu_f$  can be used as a first measure for the required angular resolution imposed by an aimed energy resolution ( $\Delta E/E = 2.0 \Delta \lambda/\lambda$ , for details see Sec. 2.4). Taking into account typical values for  $d$  (2 ... 20 Å),  $\lambda$  (0.5 ... 1.8 Å) and common scattering geometries ( $\vartheta_f = 45^\circ$ ,  $n = 1 \dots 5$ ), it can be deduced from equation (2.1.3) that the angular resolution of a triple axis experiment has to be of the order of  $0.1^\circ$  to get a resolution of  $\Delta E/E = 1\%$ . This angular resolution corresponds to the angular resolution of most TOF machines. Except for intensity losses due to the multiple-surface scattering events no additional intensity losses with respect to TOF apparatuses occur in a triple axis spectrometer that runs at the same energy resolution as state-of-the-art TOF apparatuses.

A substantial improvement of the energy resolution, say by one order of magnitude, would require angular resolutions of the order of  $0.01^\circ$  that are technologically realisable in molecular beam experiments. The reduced angular resolution causes an intensity loss of about one order of magnitude. It has been mentioned above that mechanical velocity filters providing a monochromatization of  $\Delta v/v = 0.1\%$  have a transmission of the order of one per mille. Therefore any surface grating having a reflectivity into higher order diffraction channels superior to 1% will substantially surpass the performance of mechanical velocity filters. For example, surface gratings with 10% reflectivity used in a triple-axis

spectrometer at  $\Delta E/E = 0.1\%$  will lead to a diminution of the over-all intensity with respect to current TOF machines by a factor of thousand. This is of course not negligible. On the other hand, triple axis spectroscopy provides an important intensity gain with respect to the TOF method. To ensure fast response in a TOF electron impact ionisation detector the ioniser must be operated below the emission level at which space charge in the ioniser results in long ion storage times. Since triple axis spectroscopy does not need time resolved detection this constraint can be removed giving rise to a detector efficiency which is at least one order of magnitude better than those of fast response TOF detectors. Specially designed ionisators might even allow for detection probabilities that are two orders of magnitude better than conventional ionisators used in TOF detectors [Bla95]. Therefore it can be concluded that triple axis spectroscopy offers a promising way for a substantial increase of the energy resolution of inelastic He-surface experiments without dramatic intensity loss.

So far He-surface triple axis spectrometers have not been constructed. The only attempt to use surface diffraction gratings in He-surface spectroscopy was done more than 15 years ago by Mason and Williams. They built a He-surface double axis spectrometer consisting of a standard He nozzle beam and a LiF surface as analyser grating [Mas78]. They were able to carry out several inelastic measurements from various adsorbed gases on both metallic [Mas83a, Mas83b, Mas86] and ionic crystals [Mas84]. They also succeeded in the detection of surface phonons from Cu(001) [Mas81a, Mas81b], but they could not measure them throughout the entire surface Brillouin zone as it is nowadays routinely done with modern TOF-machines. From the inelastic intensity in their experiments Mason and Williams themselves estimated that it was impossible to measure the surface dispersion throughout the whole Brillouin zone. This failure is

mainly due to the bad suitability of LiF surfaces as efficient dispersive gratings. Fig. 2.1.3 shows a typical He-diffraction scan from LiF(100) [Doa81]. The diffracted intensity is distributed into a lot of open diffraction channels, and the reflectivity into a single higher order diffraction peak can be estimated to be less than 1%. An ideal atom-optical grating would exactly feature the opposite diffraction behaviour: only a few higher order diffraction channels would be open giving rise to an enhanced reflectivity into these diffraction orders.

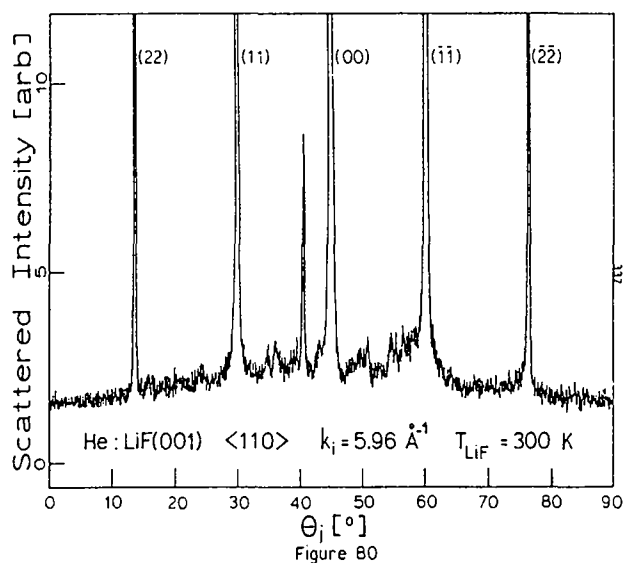


Fig. 2.1.3 : Typical He diffraction scan from a LiF(100) surface (from [Doa81]).

In conclusion it can be said that the success of He-surface triple axis spectroscopy crucially depends on the development of high reflectivity surface gratings. This can be achieved by the introduction of nanoscopic echelette gratings (blazed gratings) based on regularly stepped vicinal metal surfaces as it will be described in the next section. Based on these nanoscopic echelette gratings we have constructed a novel He-surface double axis spectrometer explained in Sec.3. Although this does not yet signify an increased energy resolution (due to the lack of the monochromator) double axis spectroscopy can make full use of a crystal spectrometer. For example, in a diffraction scan only the shear elastic intensity is recorded with a crystal spectrometer. No problems from subtracting an inelastic background as in the case of TOF arise. This can particularly be advantageous in the study of surface structures at high temperatures or for the investigation of surface phase transitions. In inelastic experiments a whole variety of new scanning possibilities exist. Each geometrical configuration of the crystal spectrometer corresponds to a single point in the  $\Delta E$ - $\Delta K$  plane of surface excitations, while in the case of a TOF spectrometer it corresponds to a parabolic line in the  $\Delta E$ - $\Delta K$  plane described by the scan-curve given in equation (2.1.1). A crystal spectrometer, thus, provides the possibility of constant  $\Delta K$  and constant  $\Delta E$  scans at the sample. In particular the constant  $\Delta K$ -scans offer significant advantages in the study of the dispersion and line width of surface phonons. Full use of this advantages can only be made if large angle scanning possibilities at the sample are provided. We therefore constructed an apparatus that allows independent scans of the angle of incidence and the total scattering angle.

A double-surface scattering experiment opens additional possibilities that are not accessible with TOF machines. For example, the first scattering

process can be used for an active monochromatization of molecular beams ( $D_2$ ,  $H_2$ ,  $HD$ ,  $Ne$ ) with inherent bad energy resolution in order to perform high resolution diffraction measurements at the second surface. Also the monochromatization process itself can be a fascinating subject. For example, the simultaneous monochromatization and rotational excitation in  $HD$  beams should reveal information to which extent the change of the internal molecular state causes a loss of spatial coherence.

## 2.2 Nanoscopic echelette gratings: concept versus reality

### 2.2.1 The concept of nanoscopic echelette gratings

The successful use of a He-surface double axis spectrometer requires surface diffraction gratings with high *reflectivities* into only a few (ideally only one) higher order diffraction channels. In classical light optics this can be achieved by stepped reflection gratings, i.e. the so called blazed gratings or echelette gratings [Ber78] illustrated in Fig. 2.2.1. They consist of flat terraces with an almost perfect reflectivity separated by steps which are much smaller than the terrace width.

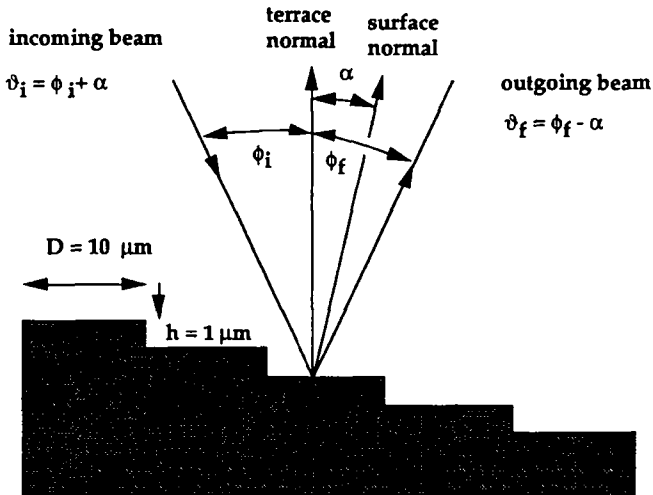


Fig. 2.2.1: Echelette grating in classical light optics.

The diffraction pattern from such a grating is the product of the terrace form factor  $A$  multiplied with the structure factor  $G$  of the grating.

$$I \propto A^2 G^2 \quad (2.2.1)$$

Since  $A$  describes the diffraction from one single terrace it can be treated (within the plane wave approximation) in analogy to the diffraction from a single slit

$$A^2 = \frac{\sin^2\left(\frac{\phi}{2}\right)}{\left(\frac{\phi}{2}\right)^2} \quad (2.2.2)$$

where 
$$\phi = \frac{2\pi}{\lambda} \tilde{D}(\sin(\phi_i) - \sin(\phi_f)) \quad (2.2.3)$$

with the wavelength  $\lambda$  and  $\tilde{D} = D(1 - \tan(\alpha)\tan(\phi_i - \alpha))$  as the not-shadowed part of the terrace.  $\phi_i$  and  $\phi_f$  denote the angle of the incoming and outgoing beam with respect to the terrace normal, and  $\alpha$  is the angle between the terrace normal and the normal of the surface defined by the step grating. The shape of the terrace form factor  $A^2$  is shown in Fig. 2.2.2 for a stepped grating having 10  $\mu\text{m}$  wide terraces and a step height of 1  $\mu\text{m}$ . The wavelength is 0.5  $\mu\text{m}$  (green light) and the chosen angles of incidence with respect to the terrace normal are 41.41°(a), 50.70° (b) and 60.00° (c).  $A^2$  is similar to forward specular scattering from a flat mirror. Its non-zero FWHM and the additional wings are due to the finite size of the terrace. For an infinite perfect grating  $G^2$  is a set of  $\delta$ -functions corresponding to the grating periodicity. Their angular positions are described by the one-dimensional Bragg-equation

$$n\lambda = d(\sin(\phi_f - \alpha) - \sin(\phi_i + \alpha)) \quad (2.2.4)$$

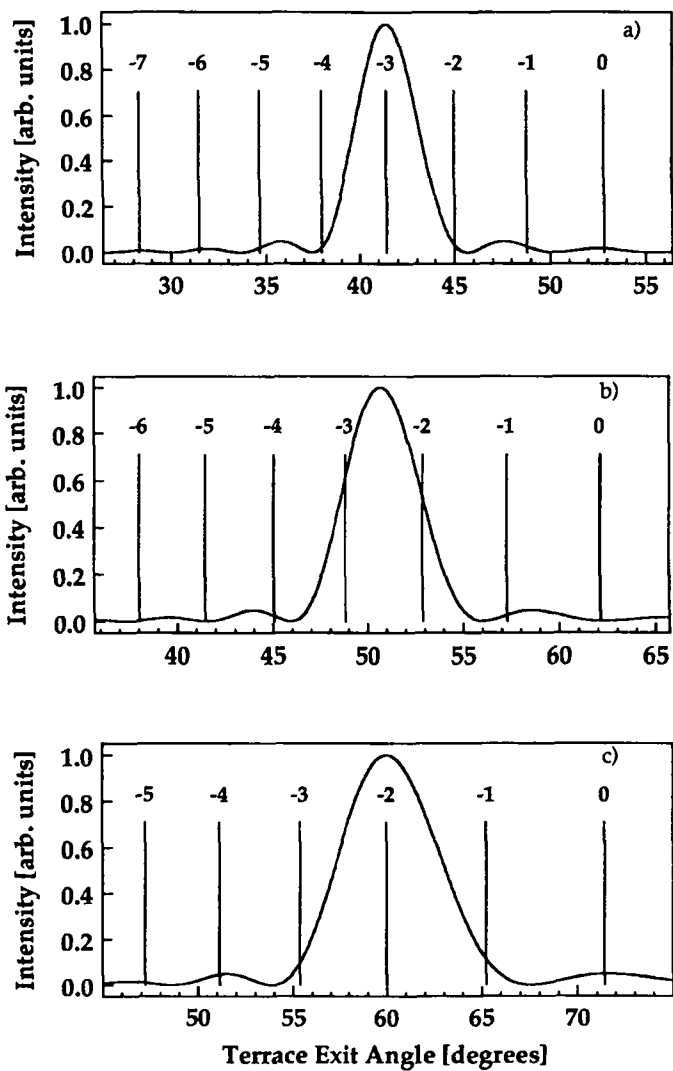


Fig. 2.2.2 : Shape of the terrace form factor of the echelette grating in Fig. 2.2.1 for different incident angles with respect to the terraces; a)  $\phi_i = 41.41^\circ$ , b)  $\phi_i = 50.70^\circ$ , c)  $\phi_i = 60.00^\circ$ . The wavelength is  $0.5 \mu\text{m}$ . Diffraction peak positions are indicated by vertical lines.



and are indicated by the vertical lines in Fig. 2.2.2 (d is the grating periodicity). Only diffraction channels that coincide with the terrace specular scattering direction are open. Therefore the number of intense diffraction peaks from such a grating is limited to 2 due to the truncation by the terrace form factor. In the example of Fig. 2.2.2 b) these two diffraction orders ( $n = -3$  and  $n = -2$ ) have almost the same intensity, because they are symmetrically arranged with respect to the specular direction of the terrace. Variation of the angle of incidence leads to a continuous shift of the positions of the diffracted beams with respect to the specular direction of the terrace. Therefore the diffracted beams of a certain order  $n$  can be made to coincide with the specular direction of the terraces by a suitable choice of the angle of incidence, i. e. the reflected beam intensity can be concentrated in one single higher-order diffraction peak. This is shown in Fig. 2.2.2 a) for a lowered angle of incidence with respect to the example of Fig. 2.2.2 b). Despite the coinciding diffraction channel ( $n = -3$ ) no other diffraction channel is open. In the example of Fig. 2.2.2 c) the incident angle has been increased so that the  $n = -2$  diffraction order coincides with the terrace specular direction. Thus, Fig. 2. a) and c) exactly describe the ideal case of a diffraction grating with a reflectivity close to unity into one higher diffraction order.

The question arises whether this concept of an echelette grating can be transferred to He-diffraction dealing with wavelengths of the order of  $1\text{\AA}$ . Since the grating period must scale with the wavelength, this would demand the fabrication of a stepped grating in the nanometer range. This is a difficult task surpassing the possibilities of current technologies. But nature provides a class of crystal surfaces, i.e. regularly stepped metal surfaces with close packed terraces, which can directly be used as **nanoscopic echelette gratings** [Kuh92]. An example for such a surface is the vicinal

Pt(997) surface consisting of (111) terraces and {111} monoatomic steps. It combines the high specular reflectivity of Pt(111) [Poe82a, Bor88], which exceeds 60% for a well prepared surface with the required step-terrace arrangement of a blazed grating as will be shown in the next section.

### 2.2.2 The vicinal Pt(997) surface

Fig. 2.2.3 a) shows a side view as well as a plane view of the (nominal) structure of the Pt(997) surface. It can be obtained by cutting a surface with an angle of  $6.45^\circ$  misoriented with respect to the (111) face. Its flat (111) terraces consist of 8.5 close packed rows of atoms into the  $\langle 1\bar{1}1 \rangle$  direction. The (macroscopic) periodicity  $d$  is  $20.21 \text{ \AA}$  and the height of the steps amounts to  $2.27 \text{ \AA}$ . For a He-beam with a wavelength of about  $1 \text{ \AA}$  the Pt(997) surface thus directly corresponds to the dimensions of the above described blazed grating in light optics. In the past, this surface has been the object of several experimental studies using diffraction techniques [Com79a, Com80, Com82, Har82, Poe81].

A recent STM investigation [Hah93, Hah94], however, directly revealed its real space structure. Fig. 2.2.3 b) shows a  $600 \text{ \AA} \times 600 \text{ \AA}$  STM image of the clean, well prepared surface. The ordered regular step arrangement can nicely be seen. Nevertheless, a close inspection of this and of similar STM images reveals a finite terrace width distribution which is shown in Fig. 2.2.3 d). This deviation from the nominal structure is not surprising, since it confirms thermodynamic predictions [Bar90].

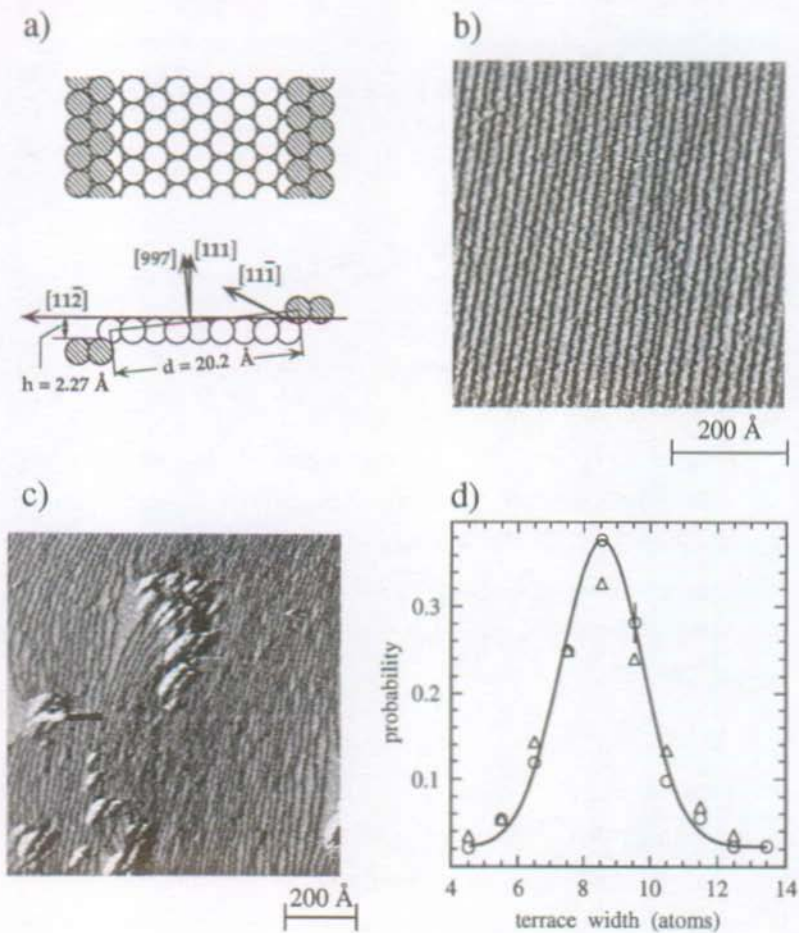


Fig 2.2.3: a) Schematic top- and side-view of the stepped Pt(997) surface; b) 600 Å x 600 Å STM image of the clean, well prepared Pt(997) surface; c) demonstration of step pinning and formation of large terraces upon carbon contamination; d) terrace width distribution of Pt(997) in units of atomic rows obtained by STM [Hah94].

The observed Gaussian-like terrace width distribution with a standard deviation of about 2.9 Å is even small when compared to the results obtained from other vicinal surfaces with comparable mean terrace widths. This can be explained within the model of Williams and Bartelt [Bar90] by the presence of strong elastic and/or dipole step-step interactions leading to the unexpected good step ordering at the surface. Nevertheless, the finite terrace width distribution will in general lead to a diffraction peak broadening and in consequence to a diminution of the resolving power of the Pt(997) nanoscopic echelette grating. This problem can be surmounted by properly adjusting the advantageous scattering condition where the diffracted beam coincidences with the terrace specular direction. Under this condition the scattering from adjacent terraces becomes in-phase and the peak broadening is cancelled out. In their theoretical study using a rough analytical ansatz Kuhnke et al. [Kuh92] claim that even higher standard deviations than 2.9 Å would still allow for a use of the Pt(997) surface as He-beam monochromator or analyser, if only this in-phase scattering condition is fulfilled (see also Sec. 4.2). In the forthcoming parts of this work we will often refer to this *in-phase scattering condition* by using the simple expression "*ideal condition*".

Rather strong deviations from the nominal structure occur in the presence of impurities. As can be seen in the STM image in Fig. 2.2.3 c) step pinning and the formation of large (111) terraces is induced by carbon (cluster) contamination.

Fig. 2.2.4 shows two experimental He-diffraction patterns of Pt(997) measured already more than 15 years ago by Comsa et al. [Com79]. Whereas the lower curve was taken at an incident angle where the terrace form factor covers two diffraction orders ( $n = -4$  and  $n = -5$ ), the upper curve was recorded

under an *ideal condition*. As predicted by the above mentioned optical model the latter case leads to the appearance of one single higher diffraction order ( $n = -6$ ). The residual intensities in the 5th and 7th diffraction order of the upper scan could be explained by being due to the poor energy resolution of the primary beam which was only  $\Delta E/E = 10\%$ . These measurements by Comsa et al. were the starting point for the initial idea [Kuh92] and the following development and construction of the novel He-surface double axis spectrometer presented in this thesis.

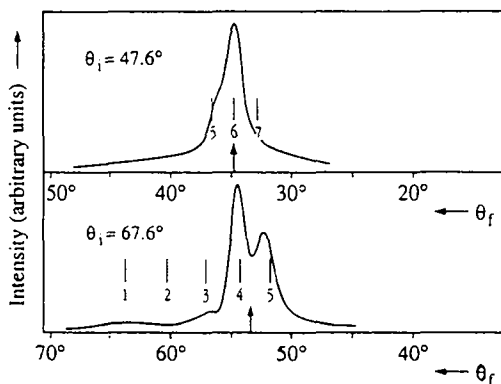


**Fig. 2.2.4 :** Experimental He-diffraction pattern of a Pt(997) surface measured by Comsa et al. [Com79a]. The primary beam energy is 63 meV.

### 2.2.3 High resolution He-diffraction from Pt(997)

The definite proof that Pt(997) surfaces can be used as nanoscopic echelette gratings can of course only be provided by a dedicated high resolution He-diffraction study of this surface. The results of such a study will be presented now. In fact, it has already been performed with our new He-surface double axis spectrometer. The details of the design and construction of this apparatus will be explained in Sec. 3. Nevertheless, there are a few experimental details the reader should be familiar with when reading this section. First of all, he should be aware that the new apparatus permits high resolution (reproducibility  $< 0.01^\circ$ ) detector scans. The total scattering angle at the sample can thereby be varied between  $59^\circ$  and  $181^\circ$  without breaking the vacuum. Although four differential pumping stages are mounted between the scattering chamber and the detector providing the dynamics of current TOF-apparatuses. The highly monochromatic ( $\Delta\lambda/\lambda \approx 1\%$ ) He-beam is furnished by a standard  $10\mu\text{m}$  nozzle beam source. Finally it should be mentioned that the measurements shown in this section have already been obtained within a double surface scattering experiment. The only difference to the final version of the apparatus was the use of a non-dispersive Pt(111)-mirror instead of a dispersive Pt(997) analyser surface. The data presented here are thus not yet energy resolved. All measurements have been performed at  $T = 750\text{ K}$ .

Fig.2.2.5 shows a detector scan (i.e. a scan of the total scattering angle at a fixed angle of incidence) taken with a 22.4 meV beam at a fixed incident angle corresponding to the *ideal condition* of the  $n=-3$  diffraction order. The whole diffraction spectrum consists of one intense  $n = -3$  diffraction peak

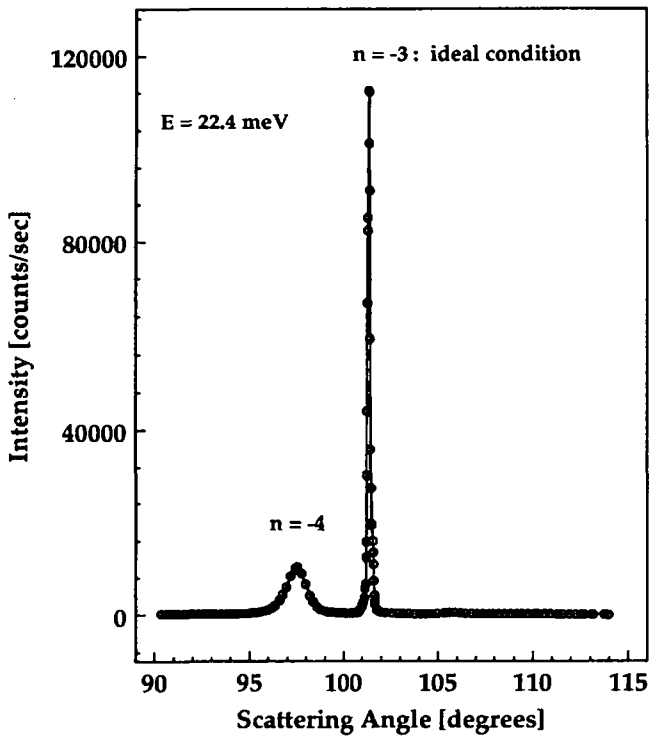


**Fig.2.2.5:** Detector scan with a 22.4 meV beam under the ideal condition for the  $n = -3$  diffraction order ( $\theta_i = 57.1^\circ$ ).

and one small peak of the  $n = -4$  diffraction order. Logarithmic plotting reveals only one additional broad feature for the  $n = -2$  diffraction order. Therefore the basic predictions of the above discussed optical model for He-diffraction from Pt(997) are well confirmed. Only diffraction channels whose Bragg rod matches with the envelope function of the terrace form factor are open. Next Fig.2.2.6 shows a detector scan taken under a non-ideal condition. The incident angle has been lowered so that the terrace envelope shifts towards higher negative diffraction orders. As expected, two intense

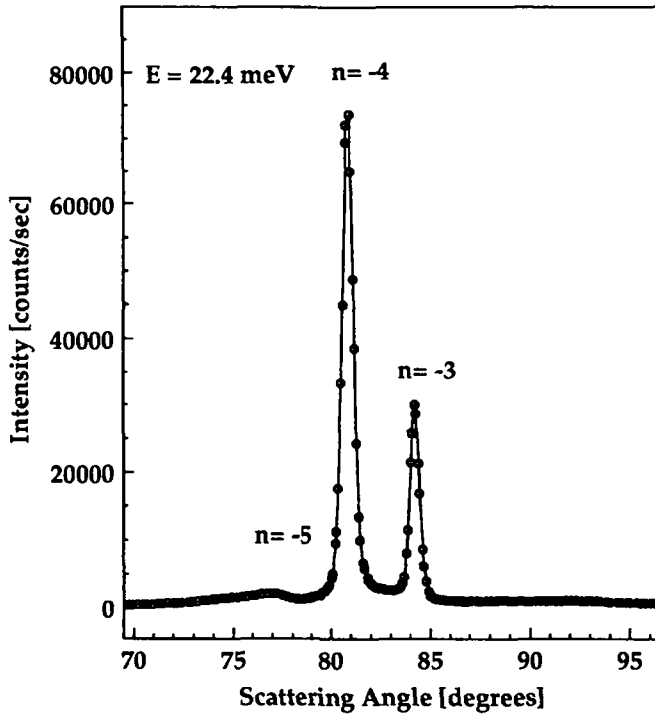
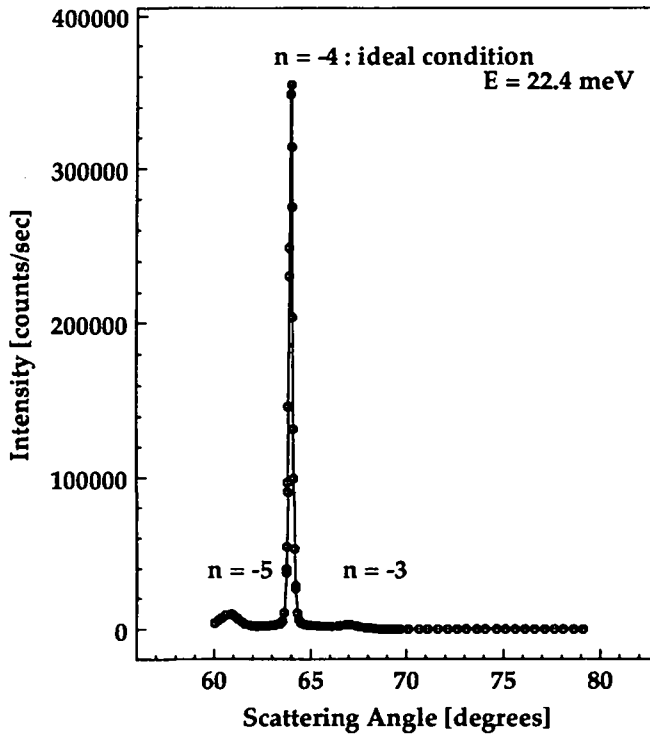


Fig.2.2.6 : Detector scan with a 22.4 meV beam in between the ideal conditions for the  $n = -3$  and the  $n = -4$  diffraction order ( $\theta_i = 47.6^\circ$ ).

diffraction peaks ( $n = -3$  and  $n = -4$ ) appear, since the envelope function now matches two Bragg rods of the surface. A further decrease of the incident angle until the next *ideal condition* (of the  $n = -4$  diffraction order) causes again a diffraction spectrum with one intense peak ( $n = -4$ ) and small satellites, as it can be seen from Fig. 2.2.7. Almost all the diffracted intensity is collected in one higher order diffraction peak. Note, that even the specular peak of the macroscopic surface cannot be observed. This confirms





**Fig. 2.2.7 :** Detector scan with a 22.4 meV beam in the very close vicinity of the ideal condition for the  $n = -4$  diffraction order ( $\delta i = 38.4^\circ$ ). Only one intense diffraction peak occurs .

the basic assumption of the optical model that the scattering is entirely dominated by specular scattering from the terraces.

The results of Fig. 2.2.5 - 2.2.7 are in perfect qualitative agreement with former He diffraction investigations of Pt(997) [Com79, Har82, Mec81]. What is new is the use of a highly monochromatic beam. By this each diffraction peak becomes an isolated feature and the basic suggestion of the optical model that almost all coherently diffracted atoms can be collected within

one higher diffraction order is confirmed. One of the main differences to the optical model is the peak broadening due to the finite terrace width distribution, as it can be seen from the different FWHMs of in-phase and out-of-phase diffraction peaks. Whereas in the spectrum of Fig.2.2.6 taken under a *non-ideal condition* both diffraction peaks are broadened, this is only the case for the satellite diffraction peaks in diffraction scans taken under an *ideal condition* (Fig. 2.2.5 and Fig. 2.2.7).

Besides the peak broadening further deviations from the predictions of the simple optical model occur. Instead of being symmetric, the spectra measured under an *ideal condition* have an intense satellite at the small angle side and a small satellite at the opposite side. This asymmetry is mainly due to the attractive part of the He-surface potential, as it has already been elaborated by Harris et al. [Har82]. In their model of a refraction-like behaviour the incoming He atoms are accelerated towards the surface and hit the terraces with a lowered (effective) incident angle. This gives rise to a shift of the specular peak of the terrace form factor towards smaller scattering angles. Although this model is rather crude it still holds for a qualitative description of our observations. The larger the incident angle the larger is the influence of this effect. This is demonstrated in Fig. 2.2.8 showing a complete series of (normalized) diffraction scans as a function of the parallel momentum transfer. Whereas curves 1), 3), 5) and 7) have been taken at incident angles corresponding to the *ideal conditions* of the  $n = -4$ ,  $n = -3$ ,  $n = -2$  and  $n = -1$  diffraction orders, curves 2), 4), 6) and 8) have been performed at intermediate incident angular positions. As it has been stated by Harris et al., the centre of gravity of the diffraction pattern shifts

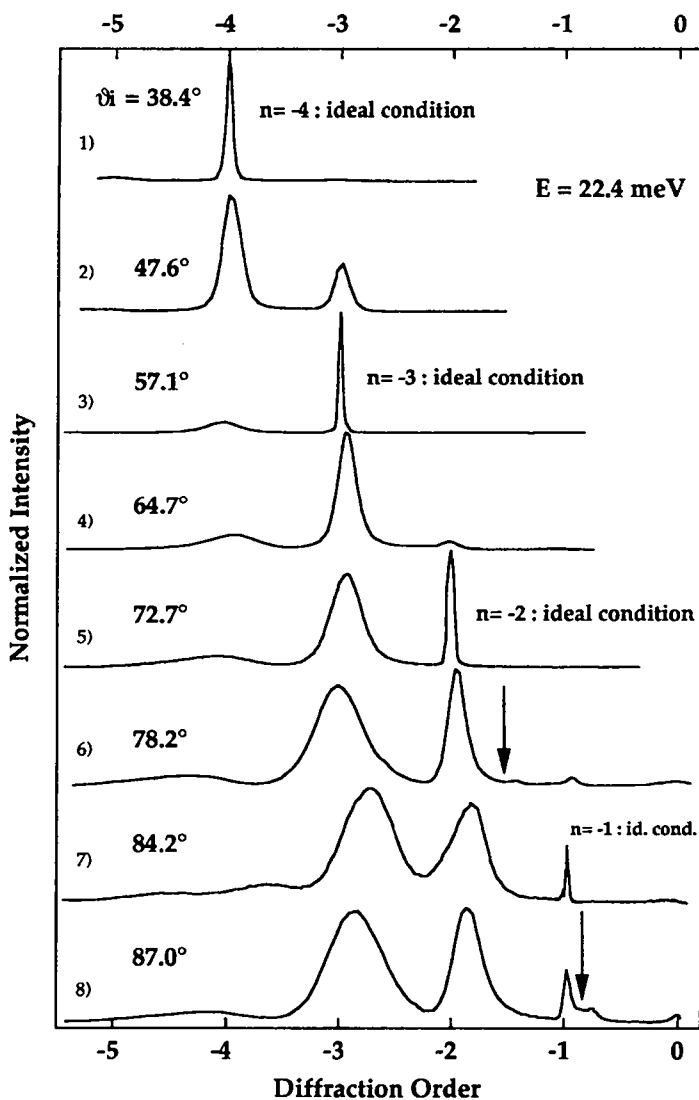


Fig. 2.2.8 : Overview of the diffraction behaviour of a 22.4 meV He- beam as a function of the angle of incidence (see text).

away from the nanoscopic (111)-specular direction towards higher negative diffraction orders (smaller scattering angles), and the optical model can no more be applied. Nevertheless, the alternation between sharp diffraction peaks at *ideal conditions* and broadened peaks at *non-ideal conditions* can still be seen. This is a general kinematical behaviour and is not affected by the special choice of the potential. What is affected, however, is the intensity of the diffraction peaks. As can be seen from Fig. 2.2.8 only a small fraction of the elastically diffracted He-atoms is collected in an in-phase diffraction peak for incident angles greater than  $70^\circ$ . Therefore the use of the Pt(997) surface as blazed grating is limited to a restricted interval of angular position settings.

Additional features appear at incident angles greater than  $80^\circ$ . A broad macroscopic specular ( $n=0$ ) peak becomes visible. It is certainly due to scattering from the steps and, thus, reflects the disorder at the surface. Secondly, a feature at the position of the specular peak with respect to the (111) terraces appears (arrow). This can be explained by the size of the illuminated area of the surface which in this grazing scattering geometry becomes of the order of the surface itself (9 mm). Thus, the probability increases to hit accidentally an area of the surface which has not been properly prepared. Finally, an intensity plateau between this microscopic specular peak and the  $n = -2$  diffraction order of curve 8) can be observed. So far we have no explanation for this. It could be a kind of selective adsorption feature [Hoi91] which is not sharp due to the finite terrace distribution.

Obviously, the data set from Fig. 2.2.8 and similar data that will be performed in the forthcoming of this section contain a lot of interesting information about surface physical aspects of the Pt(997) surface. For instance, the

amount of the peak broadening as a function of the deviation from the *ideal condition* or the systematic shift of the broad diffraction peaks with respect to their nominal positions can only be explained by going beyond [Lap81] the basic models for the simulation of He-diffraction patterns of well ordered surfaces [Rie92]. A simulation of these spectra therefore must take into account a realistic He-surface potential **and** the exact terrace width distribution. A detailed analysis [Aff94, Mar95] reveals that the terrace width distribution seen by He diffraction is significantly larger than what has been deduced from STM. This can be explained by the integrating behaviour of He-scattering whereas STM data evaluation only averages over small surface areas of typically  $500 \text{ \AA} \times 500 \text{ \AA}$ . For a detailed discussion of this "real surface effects" see the references [Aff94] and [Mar95].

The main focus of this presentation, however, are the atom-optical properties of the Pt(997) surface. Instead of asking from which kind of terrace distribution the peak broadening comes from, we try to determine experimentally to what extent the existing broadening will limit the performance of a Pt(997) echelette grating. This will be done in detail in Sect 4.1 - Sec. 4.3. So far the atom optical properties of Pt(997) with respect to He-beams with an energy of about 20 meV can be summarized as follows:

At small enough incident angles the Pt(997) surface acts as nanoscopic echelette grating allowing for a collection of almost all intensity into one higher diffraction order.

The finite terrace width distribution causes a substantial peak broadening which can be suppressed by a consequent adjustments of in-phase scattering conditions.

Despite the peak broadening the diffraction peaks are still isolated features, and the intensity between adjacent diffraction peaks almost attains the constant background level.

One great advantage of a future He-surface triple axis spectrometer with an energy resolution of the order of 0.1% will be the employment of low energy (10 meV) primary beams, since this will provide the spectroscopy of low energy excitations at surfaces with an absolute resolution of the order of 0.01 meV. We therefore examined the diffraction behaviour of Pt(997) with respect to low energy beams. Fig. 2.2.9 shows a series of detector diffraction scans (scan of the total scattering angle at a fixed incident angle) obtained with a 8.8 meV beam. Whereas curves 2) and 4) have been recorded at the *ideal condition* of the  $n = -2$  and  $n = -1$  diffraction order, curves 1), 3) and 5) have been taken at intermediate incident angles corresponding to out-of-phase conditions. A similar scenario as in the case of the 22.4 meV beam is observed. Under the ideal condition almost all the diffracted intensity is collected into one higher diffraction order. The alternation of sharp and broad diffraction peaks can again nicely be seen. Since Fig. 2.2.9 contains a plot of the relative intensities versus the scattering angle, large intensity changes as a function of the incident angle are demonstrated. They will be discussed in detail in Sec. 4.4.

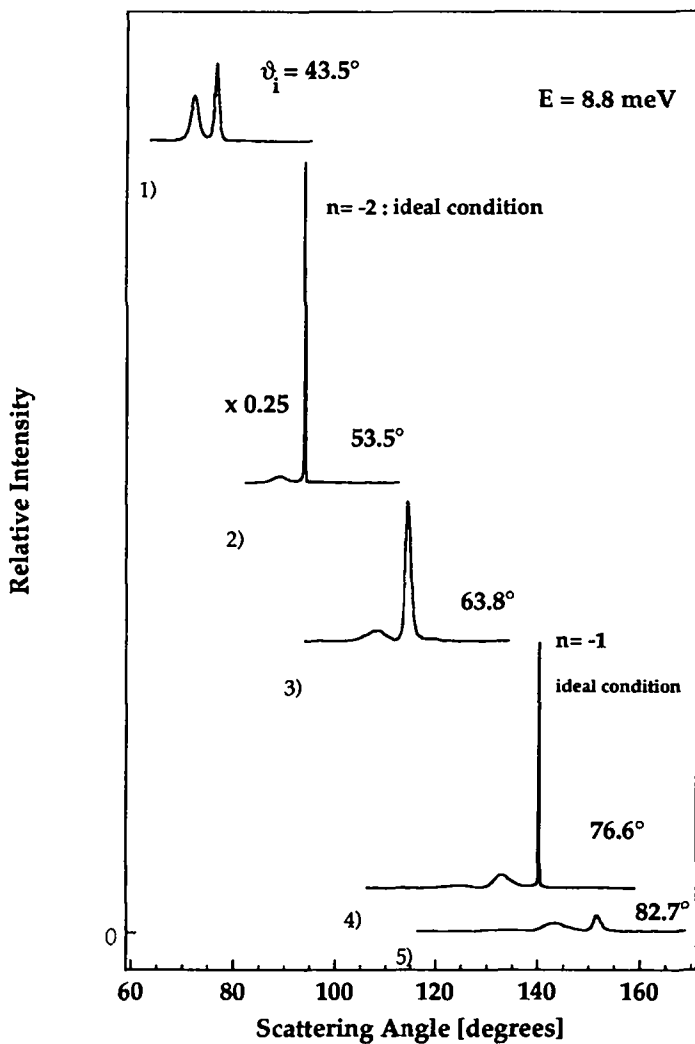


**Fig. 2.2.9** Overview of the diffraction behaviour of a 8.8 meV He-beam as a function of the angle of incidence (see text). The intensity scale is identical for all diffraction scans, except spectrum2 ( $\times 0.25$ ). The Pt(997) surface acts as almost perfect nanoscopic blazed grating.

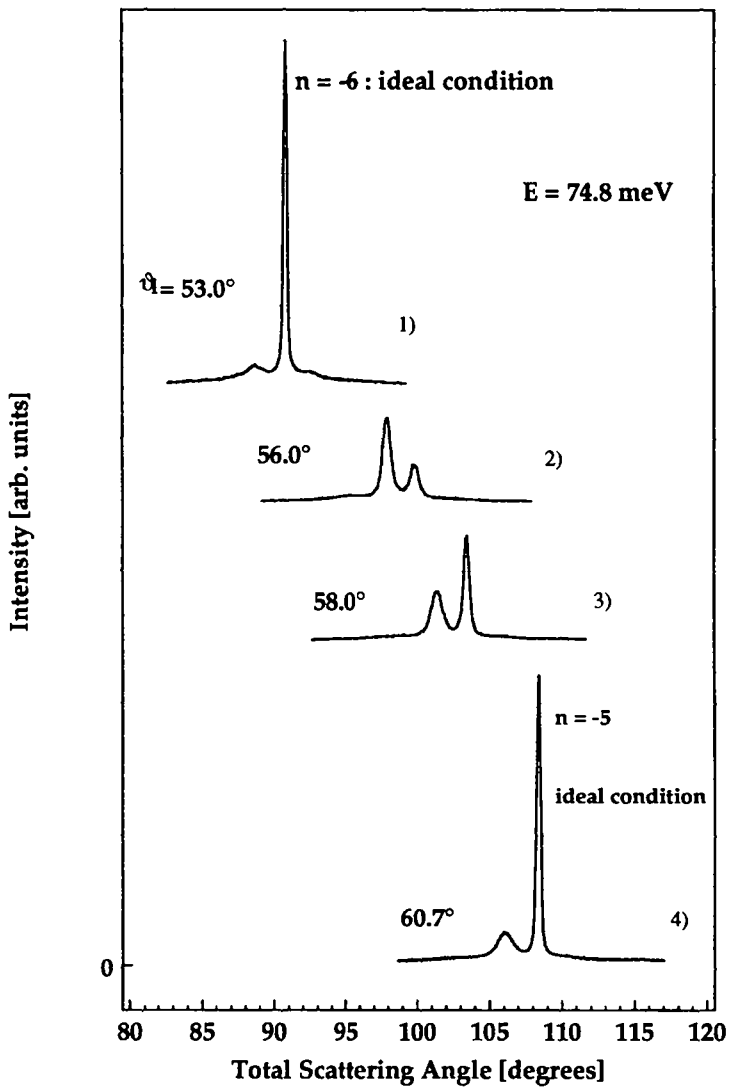


Fig. 2.2.10 : Higher order ( $n = -5$  and  $n = -6$ ) diffraction scans of Pt(997) obtained with a room temperature beam (74.8 meV).



Finally, diffraction from Pt(997) obtained with a (high energy) 74.8 meV beam is shown in Fig.2.2.10 and Fig. 2.2.11. Fig. 2.10 shows diffraction scans at the *ideal conditions* of the  $n = -6$  and  $n = -5$  diffraction order (curves 1) and 4)) and two additional scans at intermediate incident angles. Again the data agree well with the predictions of the optical model and the Pt(997) can even be used at high beam energies as nanoscopic echelette grating. The main difference to the results obtained with low energy beams is the broad base line centred around the microscopic specular direction of the (111) terraces. It is due to inelastic events becoming important at high beam energies.

For the sake of completeness Fig. 2.2.11 shows the continuation of the series of Fig. 2.2.10 for greater incident angles. Curves 6), 8) and 10) were obtained at *ideal conditions* for the  $n = -4$ ,  $n = -3$  and  $n = -2$  diffraction order, whereas the other curves were taken at intermediate incident angles. The principal behaviour is the same as in the case of a 22.4 meV beam already shown in Fig. 2.2.8. The larger the incident angle the smaller becomes the fraction of elastically scattered atoms that are collected in an in-phase diffraction peak. The appearance of a microscopic (111) specular peak already sets in at incident angles larger than  $70^\circ$ . This is due to the low transfer width at this beam energy.

In conclusion, it might be said, that the Pt(997) generally acts as almost perfect nanoscopic blazed grating for He-beams as it has been revealed from various diffraction scans using different beam energies. The above presented measurements were exclusively performed by scanning the total scattering angles at a fixed angle of incidence. The most common way to perform high-resolution diffraction scans within state-of-the-art He-diffractometers is, however, the simultaneous change of the angle of the incoming beam and the outgoing beam with respect to the surface normal

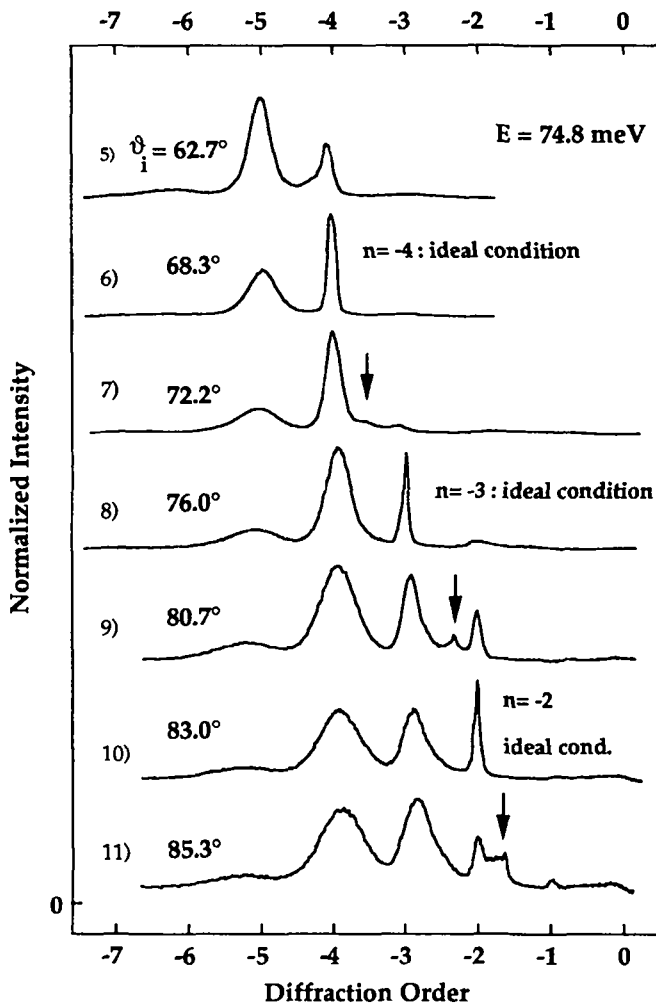


**Fig. 2.2.11** : Overview of the diffraction behaviour of a 74.8 meV He-beam as a function of the angle of incidence showing the limitations of the Pt(997) nanoscopic echelette grating (see text) .

by rotating the sample polar angle. For the sake of clearness we show in Fig. 2.2.12 such a scan that passes the ideal condition of the  $n = -3$  diffraction order. According to the optical model for diffraction from blazed gratings only one intense diffraction peak appears. Perhaps it is worthwhile to recall that this peak is a dispersive higher order diffraction feature and not a standard specular peak from a close packed metal surface.

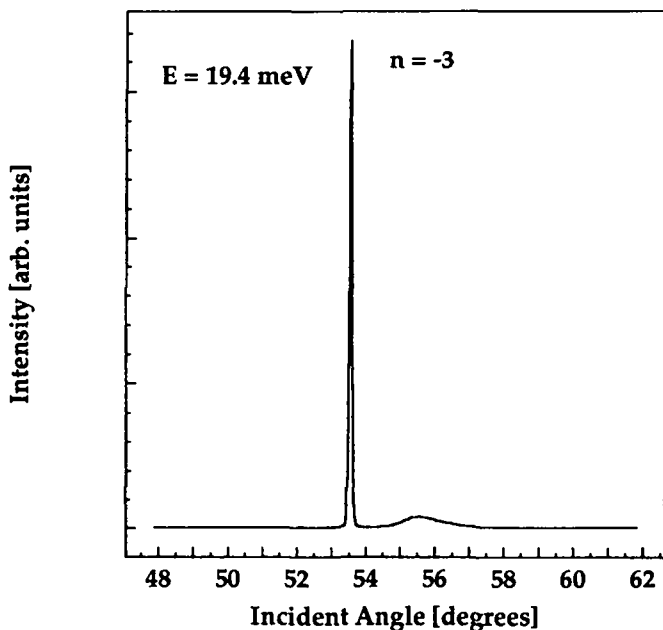


**Fig. 2.2.12:** Diffraction scan at the  $n = -3$  ideal condition (beam energy : 19.4 meV) obtained by rotating the sample polar angle at a fixed scattering geometry.

### 2.3 Mode of operation of Pt(997) echelette gratings

In this section the exact mode of operation of nanoscopic blazed gratings based on the Pt(997) surface will be discussed. As already mentioned above the peak broadening due to the finite terrace width distribution demands for an exclusive adjustment of the in-phase scattering condition. Varying the pass energy of the monochromator or analyser therefore has to be done by simultaneously changing the angle of incidence and the total scattering angle in order to maintain specular scattering with respect to the (111) terraces. This so called  $\Theta/2\Theta$ -scan is similar to energy scans performed with neutron or x-ray monochromators, since one deals in both cases with diffraction from a 3-dimensional arrangement of lattice planes. The pass energy during such a  $\Theta/2\Theta$ -scan can be expressed in terms of the angle  $\phi$  between the incoming beam and the terrace normal, the step height  $h$  and the diffraction order  $n$  by the equations

$$\lambda = \left| \cos(\phi) \cdot \frac{2h}{n} \right| \quad \text{and} \quad E[\text{meV}] \cong 20.63 / (\lambda [\text{\AA}])^2 \quad (2.3.1)$$

$\lambda$  does not depend on the terrace width. This is the reason why the finite terrace distribution does not affect the diffraction pattern under the *ideal condition*. Combining these two equations leads to the simple ready to use formula

$$E[\text{meV}] \cong 1.0 \cdot \frac{n^2}{\cos^2(\phi)} \quad (2.3.2)$$

Fig. 2.3.1 shows the pass energy as a function of the terrace incident angle for diffraction orders up to 8. It had been concluded from the He-diffraction data presented in the preceding chapter that incident angles  $\vartheta_i$  ( $\vartheta_i = \phi + 6.45^\circ$ ) greater than  $70^\circ$  lead to disadvantageous deviations from the diffraction behaviour of echelette gratings. Furthermore, the absolute

diffraction intensities dramatically decrease due to the shadowing by the steps as will be shown experimentally in Section 4. There it will additionally be shown that very small angles of incidence can also cause a decrease of the absolute diffraction intensities. Moreover they would demand for small scattering angles which are hard to realise technologically. Consequently

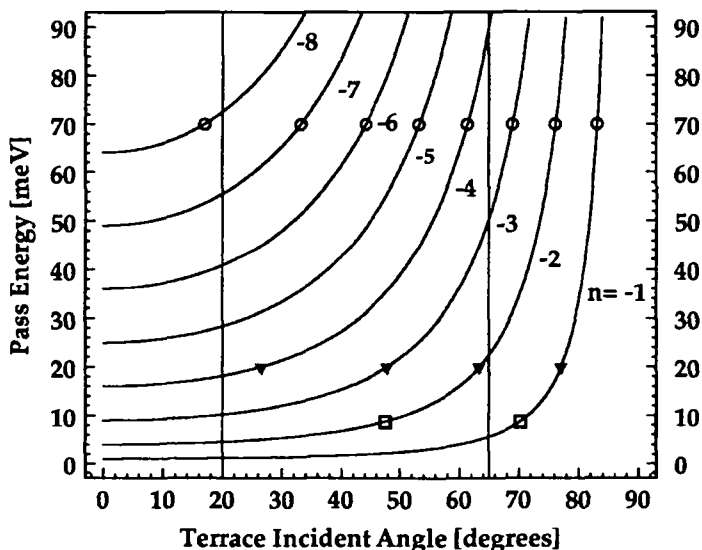


**Fig. 2.3.1 :** Pass energy at the ideal condition as a function of the incident angle with respect to the terrace normal for different diffraction orders.

there remains only a limited angle interval between 20° and 65° for a suitable use of the Pt(997) surface as He beam monochromator or analyser. This is indicated by the vertical lines in Fig. 2.3.1 . This interval of angular settings fortunately turns out to be most appropriate for the performance of inelastic He scattering experiments since any pass energy between 1.1 meV and 100 meV can be adjusted. Moreover the energy ranges of adjacent

diffraction orders overlap so that intensity changes due to changes of the working diffraction order can easily be followed.

The mode of operation of a Pt(997) analyser becomes evident from Fig. 2.3.1 where typical values of primary beam energies are indicated. The open circles indicate the energy of a room temperature beam (70 meV) and the open triangles represent the energy of a liquid-nitrogen cooled nozzle beam (20 meV). Finally, the open squares indicate a low energy beam (8.8 meV). Depending on the kind of inelastic experiment and on the primary beam energy one has to choose an appropriate working diffraction order. Whereas excitation measurements ,i.e. energy loss experiments, should be performed in such a way that the diffuse elastic peak is measured at the large angle side of the accessible interval, de-excitation will be observed with the primary energy measured at the small angle side of this interval. In both cases energy scans are taken along the curves of Fig. 2.3.1 by performing precise  $\Theta/2\Theta$ -analyser scans.

The accuracy of such an energy scan can be estimated from the slopes of the curves in Fig. 2.3.1. They are a measure for the required mechanical precision of the angular position at a given energy resolution. This angular precision can be deduced from a Taylor-expansion of equation (2.3.1)

$$\Delta\phi = \tan^{-1}(\phi) \cdot \frac{\Delta\lambda}{\lambda} \quad (2.3.3)$$

At large angles of incidence even tiny changes of the  $\Theta/2\Theta$ -angular position cause substantial changes of the pass energy. More precisely a terrace incident angle of  $65^\circ$  demands an angular precision of  $0.13^\circ$  at an energy resolution of 1%. A future use of a Pt(997) analyser with  $\Delta E/E = 0.1\%$  would therefore require an angular precision of the order of  $0.01^\circ$ . In this context it should be mentioned that the precision of the analyser angular settings is

indeed one of the crucial points in replacing a conventional TOF-detector by an analyser surface. One of the merits of the TOF technique is its high reproducibility allowing the comfortable use of a TOF-detector over long periods without worrying about the apparatus calibration [Doa89]. The equivalent to this TOF-reproducibility in a He-surface triple axis spectrometer is obviously the absolute angle positioning. We therefore developed an UHV compatible ultra high resolution angular positioning system which allows a reproducibility better than  $0.005^\circ$  of absolute angular positions. The system will be discussed in Section 3.

The above discussed angular **precision** shall be well distinguished from the angular **resolution** imposed by a desired energy resolution. Whereas the angular precision describes the accuracy of a  $\Theta/2\Theta$ -energy scan of the analyser the angular resolution determines to which amount atoms with different energies are spatially separated by the dispersive diffraction process and the diaphragms. Unfortunately there exists no standardised and even no well working definition in literature of the angular resolution in a surface molecular beam experiment. The following discussion of the energy resolution of the Pt(997) grating will therefore additionally clarify this aspect.

## 2.4 Theoretical energy resolution of Pt(997) echelette gratings

### 2.4.1 Resolution of a Pt(997) monochromator

Let us first consider the case of a monochromator application of the Pt(997) surface. The general experimental set-up of a molecular beam monochromator is straightforward. A polychromatic beam with a finite divergence coming from the nozzle scatters off the monochromator surface. Atoms with different wavelengths are scattered into different directions due to the dispersive diffraction process. The diffracted beam is selected in space (and direction) by an aperture behind the monochromator. This leads to an energy selection. A comparison of the wavelength distribution within the diffracted beam that passes the diaphragm and the wavelength distribution of the primary beam reveals the amount of monochromatization. This amount is obviously a function of the divergence  $\delta s$  of the incoming beam, the aperture size  $d$  and the aperture location. The aim of this section is to provide reliable tools for the theoretical description of the monochromatization as a function of the experiment geometry.

For this purpose let us first discuss the case of a He-beam coming from a point source with zero divergence shown in Fig. 2.4.1. It contains three wavelengths ( $\lambda$ ,  $\lambda+\Delta\lambda$  and  $\lambda-\Delta\lambda$ ) and hits the Pt(997) surface with the angle of incidence  $\vartheta_i$ . Diffraction will lead to the outgoing angles  $\vartheta_f$  and  $\vartheta_f \pm \Delta\vartheta_f$  for the three different wavelengths. Expanding the one-dimensional Bragg-equation and taking into account the constraints of the *ideal condition* expressed by equation (2.3.1) leads to a simple relation between  $\Delta\lambda/\lambda$  and  $\Delta\vartheta_f$ .



$$\frac{\Delta\lambda}{\lambda} = \frac{1}{2} \cdot \left( \frac{D}{h} + \tan(\phi) \right) \cdot \Delta\vartheta_f \quad (2.4.1)$$

with  $\phi$  being the incident angle with respect to the terraces at a given wavelength  $\lambda$  and diffraction order  $n$ . Thus  $\Delta\lambda / \lambda$  depends only slightly upon  $\lambda$  and the employed diffraction order, since  $\tan(\phi)$  is in practical cases much smaller than  $D/h$  ( $D/h \sim 20$ ). As expected it depends however directly on the angular resolution of the outgoing diffracted beam. Intuitively one would identify the ratio between the diaphragm size  $d$  and the distance  $D_D$  between the diaphragm and the surface with the angular resolution of the "experimental" set-up. Indeed each pair owing the same ratio  $d/D_D$  provides the same energy resolution. The term  $\Delta\vartheta_f = d/D_D$  therefore provides an universal measure of the energy resolution. In other words, any choice of diaphragm size and position which leads to the same spatial wavelength separation results in the same value of the angular resolution.

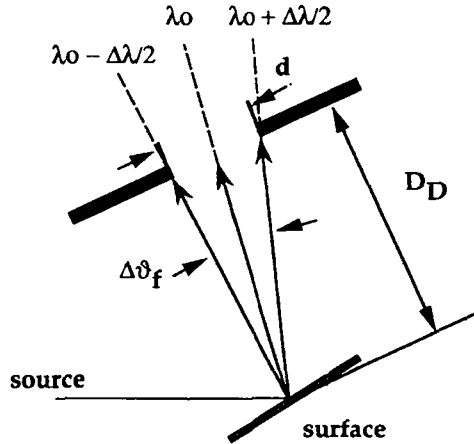


**Fig. 2.4.1:** Monochromatization gedankenexperiment with an incoming beam with zero divergence.

This statement doesn't hold any more for the realistic case of an incoming beam with a finite divergence shown in Fig. 2.4.2 for an incoming beam containing three different wavelengths ( $\lambda_0$ , "red" and "blue"). Basic geometric considerations reveal that different diaphragm settings which provide the same spatial wavelength separation result in different values for the angular resolution when applying the common formula for the angular resolution in molecular beam surface diffraction experiments given by Comsa [Com79b].

$$\Delta\vartheta_f = \sqrt{\left(\frac{\cos(\vartheta_i)}{\cos(\vartheta_f)}\delta_s\right)^2 + \left(\frac{\cos(\vartheta_i)}{\cos(\vartheta_f)}\frac{D_s}{D_d}\delta_s\right)^2 + \left(\frac{\delta d}{D_d}\right)^2} \quad (2.4.2)$$

In this equation the contributions of the beam divergence, the spot size on the sample and the detector opening are added as if they were independent Gaussians.  $\vartheta_i$  and  $\vartheta_f$  are the angles of the incoming and outgoing beams with respect to the surface normal, and  $D_s$  and  $D_d$  denote the distances between the sample, the source and the detector (see Fig. 2.4.2). The fact that different geometrical settings which provide the same monochromatization reveal different values for  $\Delta\vartheta_f$  is of course embarrassing and demonstrates the consequences of the approximations in deriving equation (2.4.2). Moreover it should be mentioned that similar problems do not appear in the description of the resolving power of an X-ray or neutron beam monochromator.

The reason for this discrepancy is indeed the difference between the diffraction process at a 2-dimensional surface grating and within the bulk of an x-ray or neutron monochromator. The latter case is illustrated in Fig. 2.4.3. Higher order diffraction in the bulk can be considered as specular scattering from parallel lattice planes. It occurs if the well known Bragg-formula

$$n\lambda = 2 \cdot l \cdot \sin(\phi) \quad (2.4.3)$$

is fulfilled ( $l$  denotes the distance between the lattice planes). From this equation or from the Ewald-construction it can be deduced that in three dimensions the diffraction problem is (mathematically) overdefined. An arbitrary monochromatic beam will therefore most probably not show diffraction. Only if its direction and its wavelength match equation (2.4.3) diffraction occurs. The wavelength separation within a neutron or x-ray

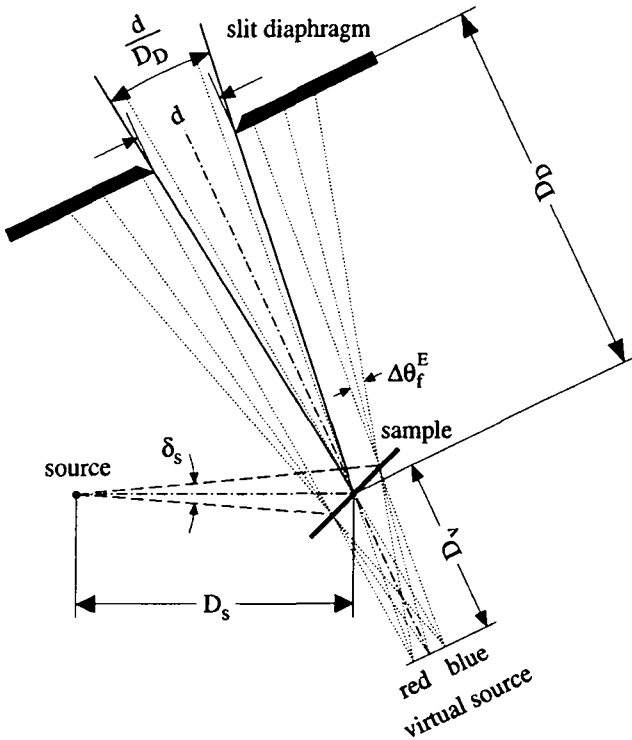


**Fig 2.4.2 :** Diffraction from a two-dimensional surface grating. Concept of virtual sources as a consequence of the diffraction process. The incoming beam contains three different wavelengths.

monochromator therefore happens - so to speak- already in the selective scattering process. For each direction within a diverging beam the corresponding energy which fulfils equation (2.4.3) is selected into the diffraction channel. The rest is concentrated in the zeroth diffraction order and cannot undergo higher order diffraction. Since diffraction exclusively occurs into the specular direction of the lattice planes the outgoing beam can be considered as a series of monochromatic beams which are inclined with respect to each other (see Fig. 2.4.3). Its maximum and minimum wavelength is directly determined by the divergence of the incoming beam. Reversely, an aperture in the outgoing beam gives rise to an effective incoming beam divergence. The amount of monochromatization therefore can easily be estimated from simple geometrical considerations.

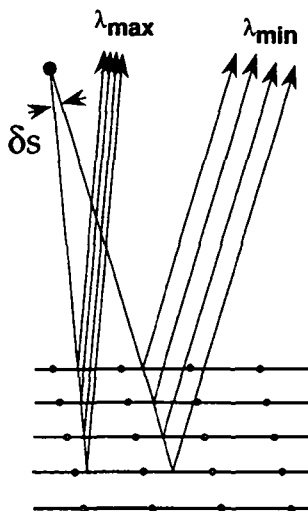


**Fig. 2.4.3 :** Sketch of the three-dimensional diffraction in the crystal bulk.

The scenario in diffraction from 2-dimensional gratings is completely different since diffraction occurs for any wavelength and incoming beam direction. He-atoms with the same incoming direction but different wavelengths  $\lambda$  and  $\lambda+\Delta\lambda$  therefore both undergo diffraction and leave the crystal under different directions (see Fig. 2.4.2). Spatial separation of atoms with different energies occurs at some distance behind the grating and is obviously a function of the interplay between the beam divergence, the aperture size and the distances involved.

Equation (2.4.2) can be modified by the introduction of virtual point sources [Com91] in order to transform  $\Delta\vartheta_f$  into a valuable measure for the energy resolution at a given geometry. As it is indicated in Fig. 2.4.2, the diffracted beam can be considered to be the superposition of three cones coming from different virtual point sources behind the surface. The divergence of the virtual source  $\delta_s^*$  is

$$\delta_s^* = \frac{\cos(\vartheta_i)}{\cos(\vartheta_f)} \delta_s \quad (2.4.4)$$

and its distance from the surface

$$D_v = \left( \frac{\cos(\vartheta_f)}{\cos(\vartheta_i)} \right) \cdot D_s \quad (2.4.5)$$

as it can be derived from a Taylor expansion of the one-dimensional Bragg-formula. Since a single slit diaphragm only provides a spatial selection and no selection of beams with certain directions, the virtual divergence has to be transformed into the effective divergence seen by the diaphragm

$$\delta_{diaphr} = \frac{D_v + D_D}{D_D} \delta_s^* \quad (2.4.6)$$

Finally one arrives at a modified expression for the angular resolution

$$\Delta\vartheta_f = \sqrt{\left( \frac{\cos(\vartheta_i)}{\cos(\vartheta_f)} \delta_s + \frac{\cos(\vartheta_i)}{\cos(\vartheta_f)} \frac{D_s}{D_d} \delta_s \right)^2 + \left( \frac{\delta d}{D_d} \right)^2} \quad (2.4.7)$$

Instead of adding the contributions of the beam divergence and the spot size as if they were independent Gaussians, "interferences" between these two terms occur, as can be seen from a comparison of equations (2.4.2) and (2.4.7). Equation (2.4.7) now provides an adequate measure for the energy resolution at a given monochromator geometry. Any geometry which provides the same spatial separation of atoms with different energies leads to equivalent values of  $\Delta\vartheta_f$ . Equation (2.4.7) together with equation (2.4.1) are therefore reliable tools for the design of a monochromatization experiment. For instance an aimed monochromatization of  $\Delta E/E = 2\%$  ( $\Delta\lambda/\lambda = 1\%$ ) requires an angular resolution of about  $0.1^\circ$  according to equation (2.4.1). This is easily available with standard apparatus sizes (for example :  $D_S = D_D$ ,  $D_D = 700$  mm), a beam divergence of the order of  $0.05^\circ$  and a diaphragm size of about of 0.5 mm. A resolution increase of one order of magnitude, however, needs at the same apparatus size a beam divergence and aperture size that are of the order of  $0.005^\circ$  and 0.05 mm !

Equation (2.4.7) can of course also be used for a description of the angular resolution of detector diffraction scans, since it describes the geometric diffraction peak broadening when working with a monochromatic beam. The additional contribution of a finite energy spread [Com79] is obtained from

$$\vartheta_f^E = |\sin(\vartheta_f) - \sin(\vartheta_f)| \sqrt{\frac{\Delta E}{E^2}} / \cos(\vartheta_f) \quad (2.4.8)$$

leading to the final expression for the angular resolution of a diffraction scan

$$\Delta\vartheta_f^{diff} = \sqrt{(\Delta\vartheta_f)^2 + (\Delta\vartheta_f^E)^2} \quad (2.4.9)$$

Knowing the spectrometer geometry equation (2.4.9) can be used to determine the velocity spread of the nozzle beam by analysing the FWHMs of diffraction peaks (see Sect. 3.4.1 : beam characteristics).

So far, the case of a simple single surface diffraction event with one diaphragm has been considered. Things become much more complicated in a double- or triple- surface scattering experiment, as it can be imagined by the example for single surface scattering given in Fig 2.4.2. A closer inspection of the scattering problem immediately reveals that one would run into severe problems when looking for an analytical expression for the corresponding angular resolution. We therefore developed an alternative description of multi-surface scattering that will be described in the next section.

#### **2.4.2 A matrix-optics like description of multi-surface scattering**

In classical light optics the theoretical description of complex experimental set-ups can be separated into its basic optical elements (mainly lenses, mirrors) by means of the matrix-optics method [Hec90]. At any place of its way through the optics under consideration a light beam is described by a few properties with respect to a reference beam along the optical axis of the optical elements. The influence of each optical element onto this light beam can be expressed in an analytical way as a matrix-operator that acts on the beam properties. This is the so called analytical ray tracing. We will now show that this idea can be transferred to molecular beam scattering.

For this purpose let us consider the example of a double-scattering experiment given in Fig. 2.4.4 a). The reference beam  $R_0$  is the beam that passes all apertures and surfaces in the centre (straight line, the dashed

beams are not considered here, but will be used later on for the description of inelastic experiments). Its wavelength  $\lambda_0$  is given by the angle settings at the surfaces and the corresponding one dimensional Bragg-equations. It is therefore not necessarily constant, but can change from one surface to the next. Any other beam  $b$  can now be described with respect to the reference beam, as it is shown in Fig. 2.4.4 b). Its properties with respect to the reference beam are the vertical displacement  $y$  and the inclination angle  $\vartheta$ . Furthermore, it is determined by its distance  $d$  from the virtual source, its divergence  $\delta$ , its beam density  $\rho$  and its wavelength  $\lambda$

$$b = (y, \vartheta, d, \delta, \rho, \lambda) \quad (2.4.10)$$

The beam intensity is  $I = \delta \rho$

The relevant atom-optical "elements" are the simple propagators  $P_i$ , the diaphragms  $D_i$  and the surface diffraction gratings  $S_i$ . The final beam  $b_f$  that passes the last diaphragm in the example of Fig. 2.4.4 a) can therefore be described by the following formal expression

$$b_f = D_3 \otimes P_5 \otimes S_2 \otimes P_4 \otimes D_2 \otimes P_3 \otimes S_1 \otimes P_2 \otimes D_1 \otimes P_1 \otimes b_i \quad (2.4.11)$$

with the initial monochromatic beam  $b_i = (0, 0, 0, \delta_s, \rho_i, \lambda)$  coming from the source. Realistic simulations of diffraction patterns are obtained by resolving equation (2.4.11) for several  $b_i$  with different wavelengths and superpositioning the results.



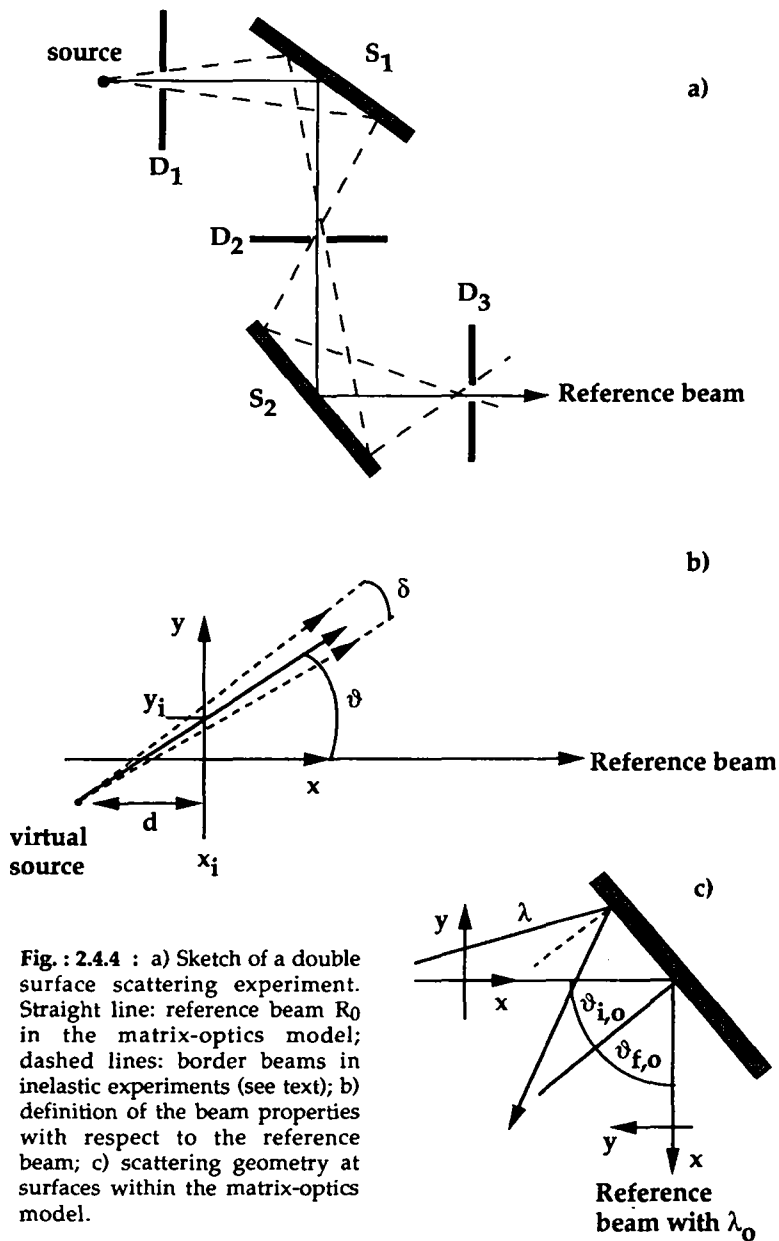


**Fig. : 2.4.4 :** a) Sketch of a double surface scattering experiment. Straight line: reference beam  $R_0$  in the matrix-optics model; dashed lines: border beams in inelastic experiments (see text); b) definition of the beam properties with respect to the reference beam; c) scattering geometry at surfaces within the matrix-optics model.

The analytical expressions for the different optical elements are:

The propagator P:

The parameter is the propagator length L.

$$\begin{aligned} y' &= y + \vartheta \cdot L ; & \delta' &= \delta ; \\ \vartheta' &= \vartheta ; & \rho' &= \rho ; \\ d' &= d + L ; & \lambda' &= \lambda \end{aligned} \quad (2.4.12)$$

It only changes the distance between the source and the beam.

The slit diaphragm:

The parameter is the vertical slit size b with respect to the reference beam.

$$\begin{aligned} y' &= \frac{y_{\max} + y_{\min}}{2} & \delta' &= \text{Max}[0, \frac{y_{\max} - y_{\min}}{d}] \\ \vartheta' &= \vartheta + \frac{y' - y}{b} & \rho' &= \rho \\ d' &= d & \lambda' &= \lambda \end{aligned} \quad (2.4.13)$$

with  $y_{\max} = \text{Min}[b/2, y + \delta/2 \cdot b]$  and  $y_{\min} = \text{Max}[-b/2, y - \delta/2 \cdot b]$

A diaphragm essentially changes the vertical beam displacement and the beam divergence. The new intensity is  $I' = \delta' \rho'$ .

### The surface diffraction:

The parameters are the incident angle  $\vartheta_i$ , the total scattering angle  $\chi = \vartheta_i + \vartheta_f$  and the diffraction order  $n$ . Basic geometric considerations using Fig. 2.4.4 c) reveal

$$y' = y \cdot \frac{\cos(\vartheta_f)}{\cos(\vartheta_i)} \cdot (1 - \vartheta \cdot \tan(\vartheta_i)) \cdot (1 + \vartheta' \cdot \tan(\vartheta_f)); \quad \rho' = \rho \cdot \left( \frac{d\vartheta_f}{d\vartheta_i} \right)^{-1}$$

$$\vartheta' = \frac{d\vartheta_f}{d\vartheta_i} \pm \frac{d\vartheta_f}{d\lambda} (\lambda - \lambda_o) \quad \begin{array}{l} "+" : \vec{e}_y \bullet \vec{n} > 0 \\ "-" : \vec{e}_y \bullet \vec{n} < 0 \end{array} ; \quad \delta' = \delta \cdot \frac{d\vartheta_f}{d\vartheta_i}$$

$$d' = d \cdot \frac{\cos(\vartheta_f)}{\cos(\vartheta_i)} \cdot \left( \frac{d\vartheta_f}{d\vartheta_i} \right)^{-1} ; \quad \lambda' = \lambda \quad (2.4.14)$$

$\lambda_o, \left. \frac{d\vartheta_f}{d\vartheta_i} \right|_{\vartheta_i, \chi, \lambda_o}$  and  $\left. \frac{d\vartheta_f}{d\lambda} \right|_{\vartheta_i, \chi, \lambda_o}$  are provided by the one dimensional Bragg-formula that has to be fulfilled by the reference beam.

Except for the wavelength, surface diffraction changes all properties of the beam. The equations (2.4.14) are derived from expansions about the reference beam values. Therefore they are only valuable for small deviations of the arbitrary beam  $b$  with respect to  $R_0$ . This condition is always fulfilled in a standard He-surface spectrometer.

Once the different operators have been established arbitrary successions of atom optical elements can easily be simulated. In Sec. 3 we will use this matrix-optics method for the determination of the primary beam velocity spread from diffraction peak FWHMs. In Sec. 5 it will be used for a simulation of monochromatization experiments.

So far this method is restricted to elastic diffraction. We are currently working on an extension that would allow for the description of inelastic processes during the scattering event. A crude albeit well working preliminary ansatz for the determination of the analyser energy resolution in inelastic experiments will be introduced in the next section.

### 2.4.3 The analyser energy resolution

The present discussion of the analyser resolution within a double-surface scattering experiment is also based on Fig. 2.4.4 a). An almost monochromatic primary beam is scattered off the sample. Making no assumptions about the kind of inelastic processes at the surface leads to a total ignorance about the energy distribution within the scattered beam. Therefore the analyser "sees" a diverging polychromatic beam coming from the illuminated area of the sample. Although it is impossible to describe the analyser resolution function in a closed expression, one can at least determine the extreme wavel-lengths that pass the analyser and enter the detector at a given analyser angular position. The beams that correspond to these extreme wavelengths are indicated in Fig. 2.4.4 a) by the dashed lines. They belong to the highest and smallest scattering angle at the analyser surface. Since one always works with negative diffraction orders at the Pt(997) surface the highest scattering angle corresponds to the smallest wavelength  $\lambda_{\min}$  and vice versa. As in the case of the matrix-optics model  $\lambda_0$  denotes a kind of reference beam that comes from the sample centre and passes through the diaphragm- and analyser centres. The analyser resolution therefore can be expressed by

$$\frac{\Delta\lambda}{\lambda} = \frac{\lambda_{\max} - \lambda_{\min}}{\lambda_0} \quad \text{or} \quad \frac{\Delta E}{E} = 2.0 \cdot \frac{\lambda_{\max} - \lambda_{\min}}{\lambda_0}. \quad (2.4.15)$$

This expression is a lower limit for the analyser resolution. Depending on the nature of inelastic scattering events at the surface, i.e. the dispersion relation  $\Delta E = \Delta E(\Delta K)$ , the effective resolution can be much better. For the case of dispersionless Einstein-oscillators at the surface, however, equation (2.4.15) should be quite realistic since inelastic scattering can occur in any direction, regardless of the parallel momentum transfer. In Sec. 3.4.2 we will use equation (2.4.15) for a discussion of the resolution of our double axis spectrometer.

### **3 Construction of the novel He-surface double axis spectrometer**

#### **3.1 Introduction and objectives**

In this section the design and construction of the novel He-surface double axis spectrometer will be described. The goal was to realize an experimental set-up that makes full use of the advantages of this new kind of spectrometer. Apart from the potential of a significant improvement of the energy resolution these advantages are mainly the possibilities of direct constant- $\Delta E$ - and constant- $\Delta K$ -scans at the sample. This demands independent adjustments of the angle of incidence and the total scattering angle with a precision that is superior to the performance of current TOF-machines. Once this is achieved any kind of scan in the  $\Delta E$ - $\Delta K$  - plane can be performed which is strongly increasing the over all kinematical range of a He-surface scattering experiment. In this context one of the special aims was a mechanical set-up that allows a continuous variation of the total scattering angle from  $60^\circ$  to  $180^\circ$ . Both extreme angular regimes have so far not been examined in inelastic He-scattering experiments and high resolution He-diffraction.

Similar scanning possibilities have to be available for the  $\Theta/2\Theta$ -energy-scans of the analyser surface. The complete analyser set-up consisting of the analyser surface and the He-beam detector unit can even be considered as a second entire high resolution He-diffractometer, since its dynamic range has to be of the order of state-of-the-art TOF flight tubes when used for high resolution diffraction measurements. Such a dynamic permits the distinction between atoms that have been selected by the analyser and continue to travel to the ionisation detector in a directed way and atoms

that were first blocked by the diaphragm behind the analyser surface before reaching the analyser by diffusion. Fig. 3.1 shows a typical time of flight spectrum (obtained from a LiF surface [Doa81]) indicating several energy losses. Concerning a He-surface double axis experiment this TOF-spectrum directly represents the incoming wavelength distribution into the analyser chamber. The small inelastic peak marked with an arrow represents at best 0.1% of the incoming flux. Its detection within a He-surface double axis

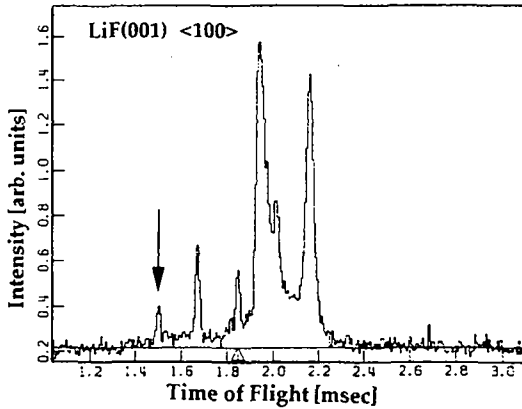


Fig. 3.1 : Typical TOF-spectrum from LiF indicating several inelastic scattering events (from [Doa81]).

spectrometer imposes severe requirements for the corresponding analyser/detector dynamics. This problem can be expressed in terms of a diffraction experiment using a monochromatic beam. Distinction between the atoms that belong to the marked inelastic event and all other atoms in a  $\Theta/2\Theta$ -scan at the Pt(997) analyser is similar to the detection of higher order diffraction from closed packed metal surfaces which is of the order of  $10^{-4}$  to  $10^{-3}$  of the specular intensity. Therefore the analyser-detector unit has to comprise suitable differential pumping comparable to current high resolution He-surface diffractometers .

A straightforward realisation of the above mentioned experimental requirements would imply an analyser-detector set-up rotating about the sample and including an additional rotation of the detector about the analyser surface. This is exactly what is done in x-ray or neutron spectrometers. In the case of He-scattering, obviously, serious problems arise, since all apparatus units have to be connected under UHV conditions. We therefore adopted a tricky scattering geometry where the change of the total scattering angle at the analyser surface is realised by a linear movement. This can be seen from the schematic sketch of the apparatus given in Fig. 3.2. An almost monochromatic He-beam is furnished by a standard high pressure nozzle source and passes two skimmers and a divergence limiting aperture. It is directed towards the sample where it is scattered off. The angle of incidence at the sample can be adjusted either by turning the sample manipulator with respect to the vacuum chamber or by rotating the whole vacuum chamber. The total scattering angle can be varied between  $59^\circ$  and  $181^\circ$  by rotating automatically the whole analyser/detector system about the sample without dismantling. The angle of incidence at the analyser surface is changed by turning the analyser in situ via a home-built high resolution sample manipulator. Changes of the total scattering angle at the analyser, however, are furnished by a linear movement parallel to the incoming beam. Currently the analyser scattering angle can only be varied between  $79^\circ$  and  $101^\circ$  due to travel limitations of the commercial available x/y/z positioning module that had been to our disposition. This angle interval will soon be increased by a specially designed translational motion device.

The analysed beam arrives from different directions at the fixed entrance slit of a quadrupole mass detector. Consequently, the diaphragm between the



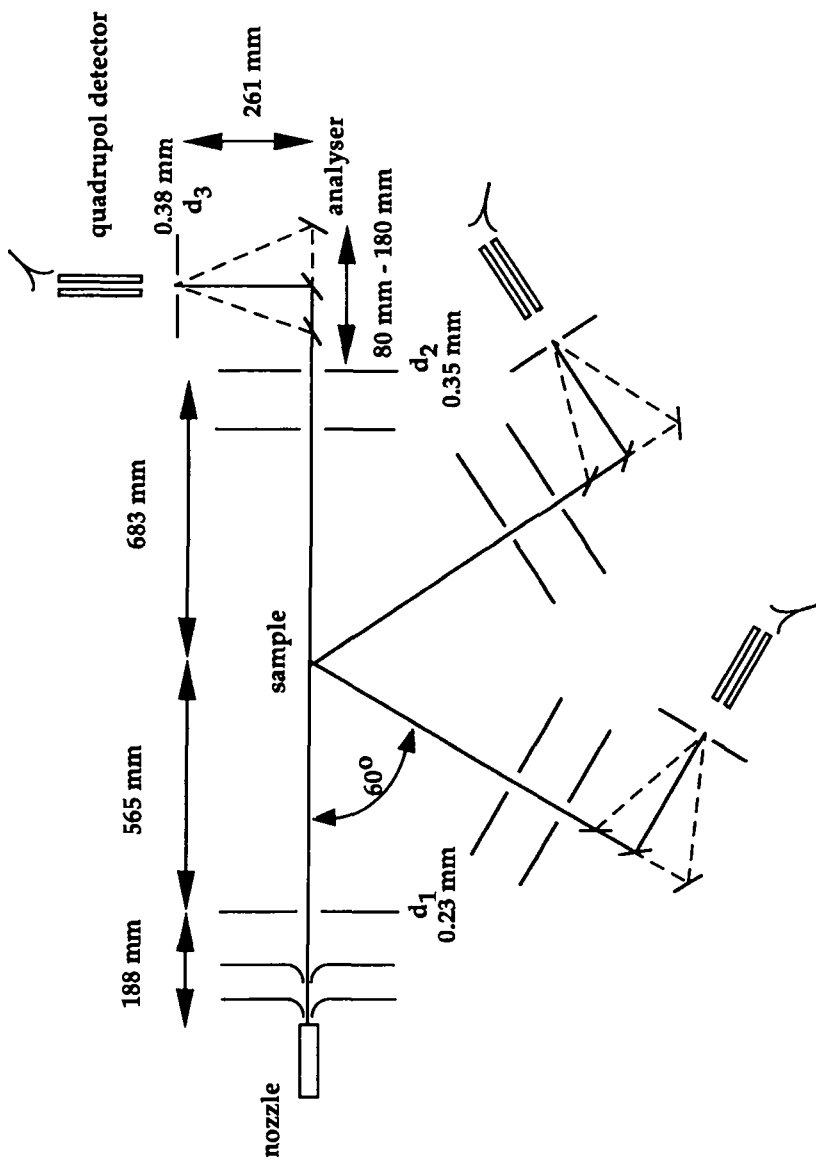
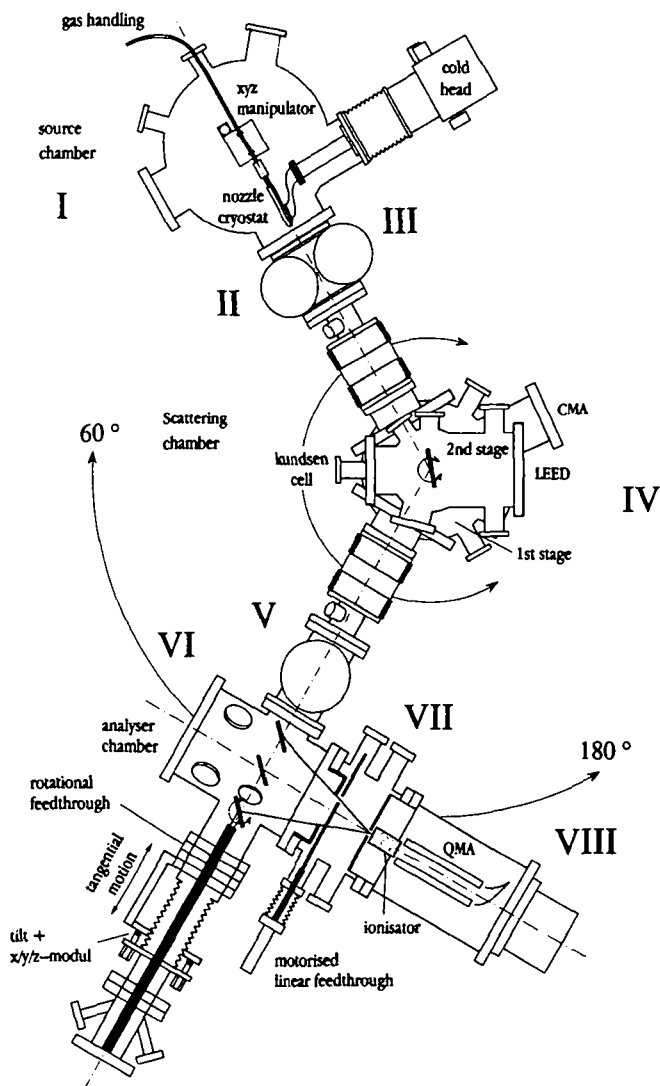


Fig. 3.2 : Schematic sketch of the He-surface double axis spectrometer.



**Fig. 3.3:** Top view of the He-surface spectrometer. The He-beam travels through the source chamber (I), two differential pumping stages (II+III), the scattering chamber (IV) containing the sample, a pumping stage (V), the analyser chamber (VI), a last pumping stage (VII) and the detector chamber (VIII).

analyser chamber and the subsequent differential pumping stage is mounted on a motorised linear feedthrough and follows the analyser linear motion.

Fig. 3.3 shows a more vivid design of the apparatus illustrating the technological challenge of the realisation of the precise rotation of the entire analyser/detector system around the sample. The corresponding mechanics and its performance will be separately presented in Section 3.3 after having discussed the main properties of the different apparatus units in Section 3.2. Section 3.3 also contains a detailed description of a specially developed UHV compatible high resolution angular position measuring system which controls the analyser polar axis of rotation. A table containing the most important apparatus parameters is added in the Appendix A.

## **3.2 The vacuum system**

### **3.2.1 The beam source**

The beam source including two differential pumping stages (150 l/sec turbomolecular pumps) is a modified copy [Mar95] of a low-energy helium nozzle beam source constructed by Kern, David and Comsa [Ker85] at Jülich. Its main chamber is pumped by a 6000 l/sec oil diffusion pump boosted by a 500 m<sup>3</sup>h<sup>-1</sup> roots blower allowing for stagnation pressures up to 280 bar with a 10 µm (nominal) nozzle diameter at room temperature. The expanding beam is skimmed by two skimmers with a diameter of 0.28 mm and 0.2 mm, respectively.

The nozzle temperature can be varied between 500 K and 40 K by means of a filament heating and cooling with a Helium cold head. The temperature is stabilised to better than  $\pm 0.2$  K by a commercial PID- regulator.

### **3.2.2 The scattering chamber**

The scattering chamber contains the sample and is thus supplied with standard surface science equipment consisting of a home built ion gun, a CMA (cylindrical mirror analyser) Auger spectrometer (Omicron) and LEED (low energy electron diffraction) mounted at two different stages of the vacuum chamber. The sample is mounted on a precise sample manipulator [Dav86] that has been constructed in Jülich by R. David and V. Marsico [Mar95] It allows for independent adjustments and scans of the polar angle, the azimuthal angle and the tilt. The hat shaped sample ( $\varnothing$  10 mm) can be heated to 1400 K by electron bombardment from the rear. Sample cooling down to 25 K is provided by a liquid-He cryostat attached to the sample holder by a copper braid. The temperature is measured by a spot welded Ni/CrNi thermocouple and can be stabilised better than  $\pm 0.2$  K.

Fig. 3.6 in Section 3.3 shows a section view of the lower part of the scattering chamber which contains the scattering plane. In the scattering position three flanges are directed towards the sample permitting in situ evaporation or sputtering experiments.

### 3.2.3 The analyser chamber

The analyser chamber is separated from the scattering chamber by a differential pumping stage. Although this additionally improves the apparatus dynamics, the main reason for this is a mutual protection of the sample and the analyser surface. As will be shown in Sec. 4.3 chemical passivation of the Pt(997) in order to prevent contamination of the analyser surface can be achieved by exposing the surface to a mixed oxygen hydrogen atmosphere. On the other hand, experiments including reactive gases might be performed at the sample. The pumping stage therefore allows for individual treatments of the surface while the valve between the scattering chamber and the analyser chamber is open.

The analyser chamber is again equipped with a home built ion gun. If necessary, a LEED - System can properly be mounted in front of the analyser surface. Surface analysis is directly done by means of He atom diffraction. For this purpose the total scattering angle at the sample is adjusted to  $180^\circ$  and the sample is taken off the beam allowing for ordinary He-scattering experiments from the analyser surface. The analyser crystal is mounted onto a special manipulator explained in Sec. 3.3.2 . Its temperature can be varied between 1400 K and 80 K by electron bombardment and liquid nitrogen cooling, respectively<sup>1</sup>.

---

<sup>1</sup>The cooling option has been removed in the meanwhile.

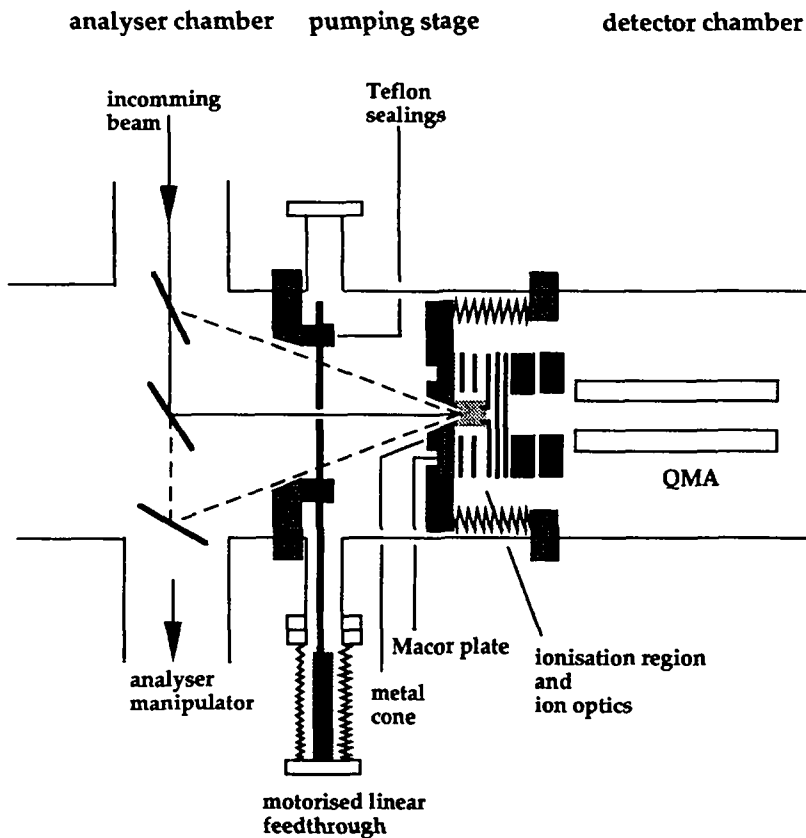


Fig. 3.4 : Sketch of the analyser/detector vacuum unit containing an additional pumping stage (see text).

### 3.2.4 The detector unit

As it has been outlined in the introduction of this chapter the detector chamber containing a quadrupol mass filter (Extra Nuclear) has to be separated from the analyser by efficient differential pumping stages. The number of stages (TOF machines have up to 9 pumping stages [Toe87]) can be reduced by applying small apertures between the different vacuum chambers. In most TOF-machines this would, however, cause disadvantageous intensity losses, because the corresponding increased angular resolution would not further improve the energy resolution [Smi88]. In the case of a double axis spectrometer using a Pt(997) analyser a slightly increased angular resolution with respect to TOF-machines is necessary. Therefore the choice of small apertures between the different vacuum units is even convenient and does not cause needless intensity losses. Consequently one gets along with one single stage between the analyser and the detector as it will be shown next.

The detector entrance slit has a size of  $0.38 \times 3.5 \text{ mm}^2$ . It has to be located in such a way that the passing beam hits the detector ionisation region for any possible incoming direction. We therefore transformed the ionisator of a recently described [Kuh94] high performance molecular beam detector by mounting its entrance slit on a metallic cone which penetrates into the ionisation region. This is shown in Fig. 3.4. The metallic cone itself is mounted on a Macor disc that is attached to the vacuum walls via a flexible metal bellow. The entrance slit is electrically isolated and can be used as powerful ion optical element, i.e. the so called ion repeller.

Fig. 3.4 also shows the movable slit diaphragm between the analyser chamber and the pumping stage. A rectangular metal sheet containing a 2 mm wide slit is guided between two rectangular Teflon sealings that are

pressed against each other by a set of springs. The metal sheet is attached to a motorised linear feed through. The size of the slit has to be somewhat higher than the size of the entrance slit of the detector to get a maximal intensity with the energy resolution determined by the size of the detector entrance slit. Nevertheless, the current size of this movable slit can still be reduced by a factor of 2 which has not been done so far in order to prevent aligning difficulties. An already planned ex-situ installation of a precise measuring system for the diaphragm position will surmount this problem allowing for a doubling of the analyser/detector dynamics which actually amounts to  $4.0 \times 10^{-4}$ . This value can be deduced from high resolution diffraction scans from a Pt(111) surface that has been mounted as a simple mirror like "analyser" surface during the early stages of the apparatus construction. Fig. 3.5 shows such a scan in the  $\langle 11\bar{2} \rangle$  azimuthal direction that has been obtained at a fixed scattering geometry by varying the polar angle. Apart from the intense specular peak a well resolved first order diffraction peak appears. Note that the spectrum has been taken at a sample temperature of 750 K with an incoming beam divergence of only  $\sim 0.01^\circ$  as it can be deduced from the diaphragm sizes given in Fig 3.2. The absolute intensity of the Pt(111) specular peak therefore is of the same order of magnitude as other specular intensities from closed packed metal surfaces reported in literature. The relative intensity of the diffraction peak with respect to the specular intensity also agrees with the results of other high resolution diffraction measurements from Pt(111) [Bor89, Ker86]. Summing up it might be said that the presented analyser/detector experimental set-up containing only one single differential pumping stage has almost the same dynamic range as current TOF detectors.



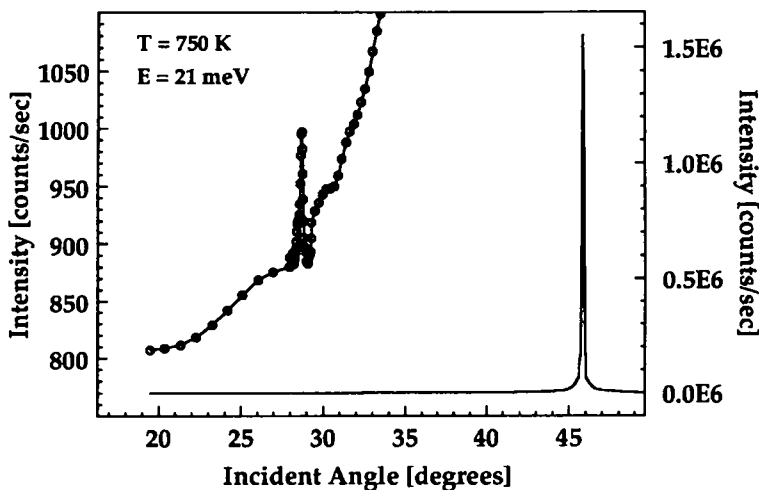


Fig. 3.5 : He diffraction scan of Pt(111) into the  $\langle 11-2 \rangle$  direction at a fixed scattering geometry of  $91.7^\circ$ ;  $T = 750$  K. The beam energy is 21 meV.

### 3.3 Scanning possibilities at the sample and the analyser

#### 3.3.1 Scattering chamber rotation and detector rotation

The mechanical design of the different scanning possibilities at the sample has been inspired by the design of modern neutron triple-axis-spectrometers [Mon83] or advanced surface x-ray diffractometers at synchrotron light sources [Als87, Bre84]. In this devices sample manipulation is provided by manipulating the entire (UHV) vacuum chamber instead of moving the sample with respect to the vacuum chamber. One of the main advantages of this method is its high mechanical precision since robust and well

developed industrial positioning devices can be used. These devices are able to carry tons and are also applied for the rotation of the whole detector set-up around the sample. Usually they are driven by stepping motors and their positions and movements are controlled by means of ultra high precision resolvers permitting extraordinary reproducibilities. A new class of rotational tables has recently been introduced in robotics (Megatorque Inc. [Meg91]) by combining the propulsion directly with the mechanical support and the resolver. The load is directly attached to the motor axis. An intelligent electronics permanently controls the actual angular position and tries to adjust the nominal value by means of a PID regulator allowing for reproducibility's far below  $0.01^\circ$ . This novel kind of rotary tables has successfully been applied in x-ray diffraction, too.

Knowing about the mechanical performance of modern x-ray or neutron spectrometers it becomes desirable to adopt this method within a He-surface spectrometer. The section view of our apparatus given in Fig. 3.6 illustrates how this can be achieved. The complete vacuum assembly of the scattering chamber is mounted on top of a classical mechanical rotary table (Francke [Fra91]) which is mounted exactly coaxially above a modern robotronic rotary table (Megatorque motor). The latter provides the rotation of the complete analyser/detector vacuum assembly via an extremely rigid swivel arm that makes part of the vacuum system support. This support glides on a specially surface finished granite plate with the help of air-cushion devices. The granite plate having a weight of more than 3.5 tons is mounted on three adjustable supports. This allows for a precise horizontal adjustments and for corrections that become necessary due to deformations of the building floor. As already stated, the total scattering angle can be varied between  $59^\circ$  and  $181^\circ$ . The scattering chamber can be rotated by  $\pm 30.5^\circ$  with respect to the source chamber and analyser chamber.

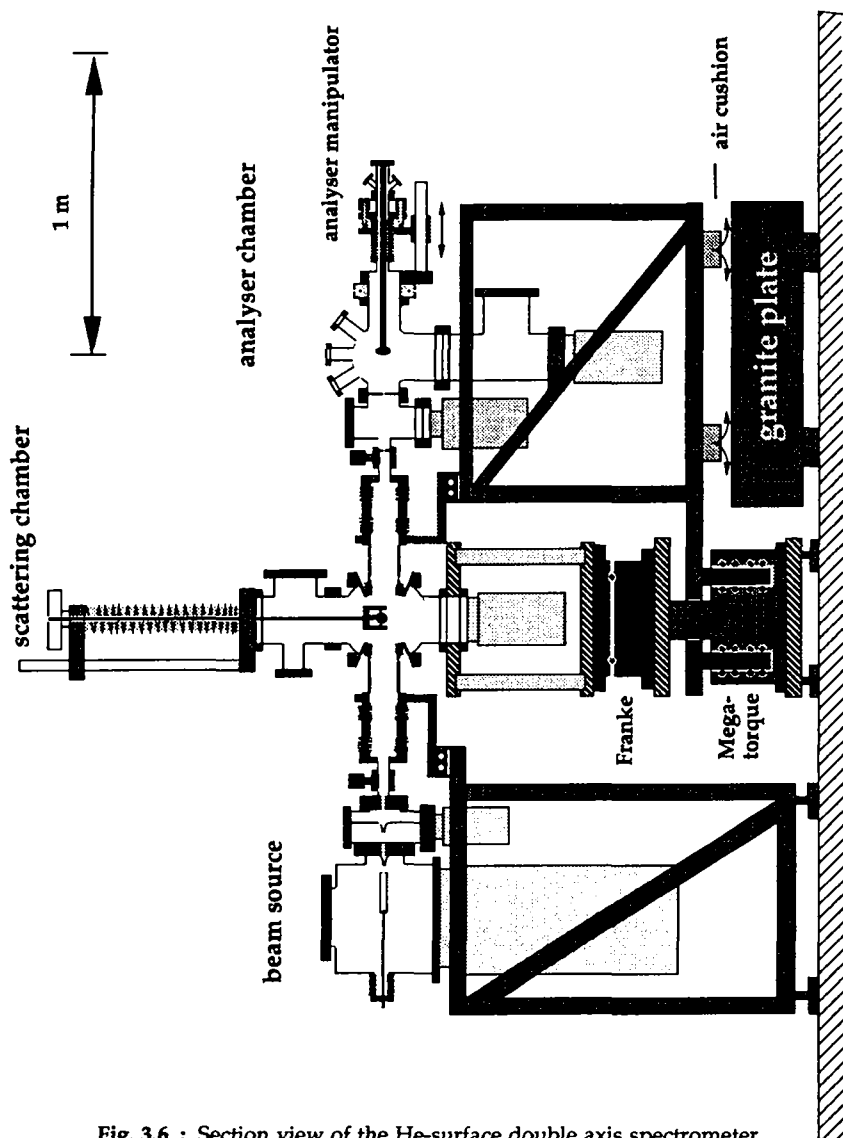


**Fig. 3.6 :** Section view of the He-surface double axis spectrometer showing the technical solution for the independent scanning possibilities of the scattering chamber and the analyser/detector system.

One of the crucial points is of course the vacuum connection between the scattering chamber, the beam source and the analyser chamber, respectively. In order to avoid the use of metal bellows that are directly welded to the scattering chamber a special bellows arrangement has been developed. This is shown by the horizontal cross section through the scattering chamber containing the scattering plane (Fig. 3.7) . The scattering chamber is based on a sphere to which two CF 200 flanges are tangentially welded with an angle of  $120^\circ$  with respect to each other. The counter flanges carry a cone with an opening angle of  $70^\circ$  that penetrates into the scattering chamber. Metal bellows are welded to this cones. They are elongated by rigid tubes which are again connected to a bellows followed by a second tube and a last bellows. By this, the deformation of the bellows during rotation of the scattering chamber or the analyser/detector set-up can be divided into a pure circular deformation with varying radius of curvature and a pure translation. This can be seen from the almost extreme position of the bellows arrangement connecting the scattering chamber with the He beam source at the left hand side of the design in Fig. 3.7 . This position is achieved by rotating the scattering chamber about  $30^\circ$  from the equilibrium. Whereas the bellows at the cone undergoes a pure circular deformation the two remaining bellows perform a translation with the help of the intervening tube. This kind of motion would not happen automatically and has thus to be guided by a stepmotor motorised linear motion device that is attached to the long tube between the first and the second bellows. In consequence, any rotation of the scattering chamber implies the simultaneous accommodation of the linear motions of both vacuum connections, whereas varying the scattering angle only requires to accommodate the linear motion of the connection between the scattering chamber and the analyser chamber.

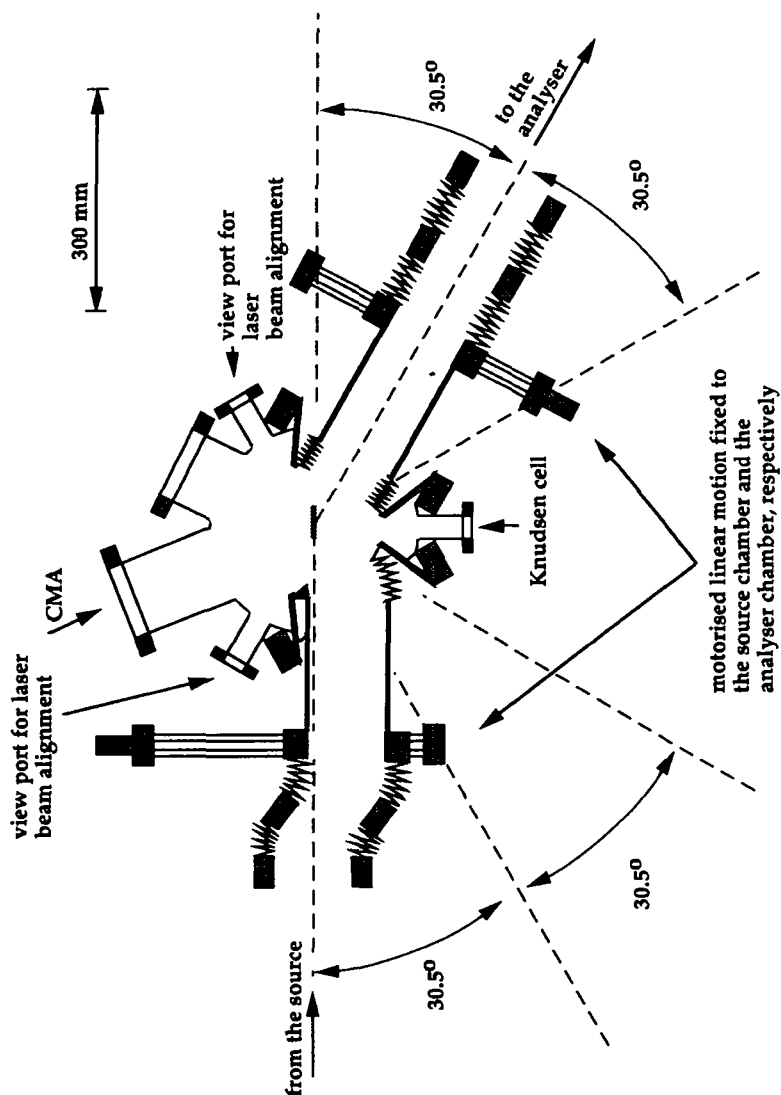


Fig. 3.7 : Horizontal cross section through the scattering chamber containing the scattering plane. The vacuum connection to the beam source and analyser/detector system is made by flexible bellows.

In the position example of Fig. 3.7 the analyser/detector system is in its equilibrium position with respect to the scattering chamber. Since the scattering chamber is rotated by  $30^\circ$ , the total scattering angle amounts to  $150^\circ$ . The extreme scattering geometry of  $180^\circ$  is achieved by rotating the detector about  $30^\circ$ . Whereas in the extreme positions of  $180^\circ$  and  $60^\circ$  no wide range scans with the scattering chamber are possible, any other total scattering geometry allows for sufficient wide scattering chamber scans. The widest scan ( $\pm 30.5^\circ$ ) can obviously be performed at a total scattering angle of  $120^\circ$ . The possibilities of scattering chamber scans can be enlarged by suitable accommodations of the polar angle position of the sample manipulator with respect to the scattering chamber.

We will now demonstrate the performance of detector scans at fixed angles of incidence. For this purpose Fig. 3.8 shows two scans of the primary beam at  $180^\circ$ . They were taken with a Pt(111) "analyser" surface that simply reflects the beam towards the detector. In both spectra the step width was  $0.02^\circ$ . After having performed the first scan, arbitrary large angle movements have been performed with the detector. Then, the first scan has been repeated into the opposite scanning direction. Furthermore, the nominal angle positions have been chosen to shift about  $0.01^\circ$  with respect to the first scan leading to an almost perfect alternation of the data points of the first scan (open circles) and the second scan (filled squares). This means that our mechanical set-up completely converts the nominal angular reproducibility ( $\sim 0.003^\circ$ ) of the *Megatorque motor* into an equal scattering angle reproducibility. The slight deviations from a perfect alternation of the different data points is a direct consequence of the data acquisition procedure during a scan. For each step the computer program transfers the new nominal value to the motor electronics which adjusts the new value by means of its PID-regulator.

During this regulation the computer program permanently reads the position and calculates a kind of mean deviation per unit of time. Data acquisition is only performed if this deviation is smaller than a chosen tolerance value. The scans of Fig 3.8 have been taken with a tolerance of  $0.01^\circ$ . At this tolerance the time needed to adjust a new angular position is about 2 to 5 seconds and so it is short enough for fast high resolution scans. Smaller tolerance values of the order of  $0.005^\circ$  lead to scanning precisions that prevent the above mentioned irregularities, but the angular position adjustment becomes more time consuming. On the other hand higher tolerance values, allow for much faster scans whose velocity is rather limited by the motor torque. Depending on the kind of experiments performed during the present thesis tolerances between  $0.1^\circ$  and  $0.005^\circ$  have normally be used.

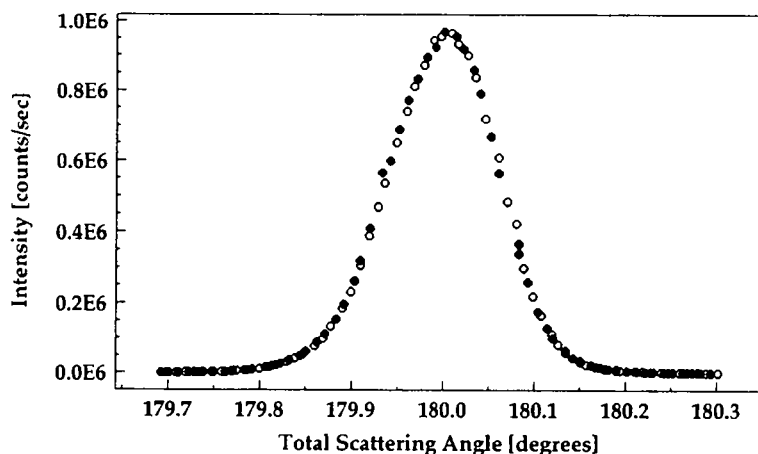


Fig. 3.8 : High resolution detector scans of the primary beam at  $180^\circ$ . The two scans were taken into the opposite scanning direction

Finally, it should be recalled that the angular positions are measured in an absolute way. Once the primary beam is detected, any total scattering angle between  $59^\circ$  and  $181^\circ$  can directly be approached with a precision better than  $\pm 0.005^\circ$ .

Now the performance of scans with varying angles of incidence at a fixed scattering angle performed by rotating the whole scattering chamber will be discussed. For this Fig. 3.9 shows three diffraction scans from the Pt(997) surface. As in the upper case of the detector scans arbitrary angle movements have been performed with the scattering chamber between the scans. Nevertheless, the peak position remains almost constant during the forward and backward repetition of the initial reference spectrum. Note the small peak FWHM of about  $0.05^\circ$ . The reason for the differences between the spectra is twofold. First, the purely mechanical rotary table supporting the scattering chamber is not yet equipped with a resolver system. This will be done in the near future. The number of stepping motor steps is thus the only control of the angular motion, and mechanical play can not be corrected for. Nevertheless, the reproducibility is extremely high ( $\approx 0.01^\circ$ ) and exceeds -to our opinion- the (real) precision of any UHV-sample-manipulator. Secondly little temperature fluctuations of the cooled nozzle cause intensity changes since the measured peak is a higher order diffraction peak.

The possibility of polar angle scans by rotating the scattering chamber turned out to be very advantageous. Polar angle scanning with the UHV-manipulator is only used for precise changes of the sample position with respect to the scattering chamber. For example, sample cooling with liquid Nitrogen or Helium is no more critical since the stiffened copper braid that attaches the sample to the cryostat has not to be moved anymore. Therefore



the azimuthal and the tilt angular position can no more be affected by polar angle scans.

In conclusion it might be said that the presented mechanical set-up allowing independent rotations of the scattering chamber and the analyser/detector system has a sufficient high reproducibility for a future full use of the specific advantages of He-surface double axis spectrometry. This properties are completed by extremely precise analyser motions that will be presented in the next section.

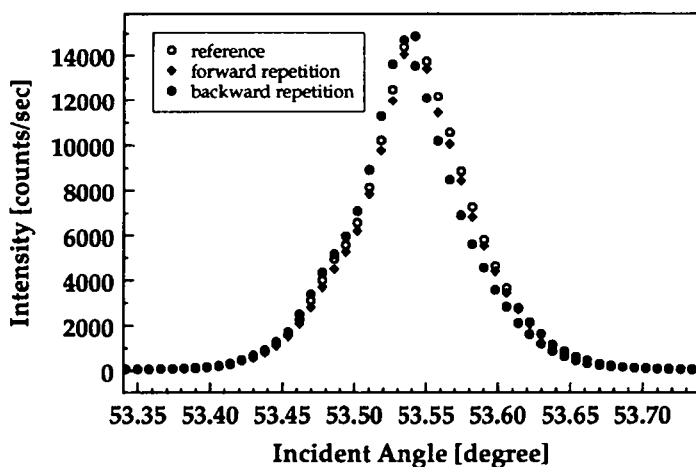


Fig. 3.9 : High resolution scattering chamber scans of a Pt(997) diffraction peak including a forward repetition and a backward repetition.

### 3.3.2 Ultra high resolution sample positioning in UHV

It has been pointed out in Sec. 2.1 that the use of crystal surfaces as molecular beam monochromators or analysers demands above all *relative* angle position resolutions between  $0.2^\circ$  and  $0.02^\circ$  depending on the desired

energy resolution between 2% and 0.2 %. For a single-experiment this can probably be achieved by standard pure mechanical sample manipulators. But if it is aimed to replace a conventional TOF-detector by an analyser set-up with a crystal surface without loss of performance considerable mechanical problems arise since high reproducibility is one of the special merits of the TOF technique allowing for the use of a TOF-detector routinely over long periods without worrying about the apparatus calibration [Doa92].

In a double axis spectrometer the equivalent to the TOF-reproducibility is the absolute angle positioning. It is a daily laboratory life experience that all mechanical driven manipulators have a certain play. Therefore, scans are always performed in the same direction. Nevertheless, subsequent scans can easily be shifted by an amount greater than 0.02 or 0.2 degrees. This is usually taken into account by recalibrating or readjusting on a well known intensity peak. It is evident that the latter method would not be practicable in an extended run with a He surface double axis spectrometer. Moreover, in the case of the vicinal Pt(997)-surface this method would even not apply for the two following reasons:

- Whereas for low index surfaces small deviations from the desired angular position only change the pass-energy but not the diffraction intensities, also the diffraction intensities from the Pt(997)-surface strongly decrease when accidentally the rainbow scattering position of the *ideal condition* is left.

- Any deviation from the *ideal condition* will lead to a broadening of the diffraction peaks and thus to a decreasing energy resolution due to the finite terraces length distribution. In Sec. 4.2 it will be shown

experimentally that already a deviation of  $0.1^\circ$  with respect to the *ideal condition* gives rise to an extra-broadening of about  $0.02^\circ$ .

Thus, a successful use of nanoscopic echelette gratings strictly requires perfect  $\Theta/2\Theta$ -scans and, in consequence, independent absolute positioning of both the incident and scattering angle. This can only be achieved by controlling the angular positions with modern incremental position measuring techniques (resolvers) as they are applied in X-ray diffractometers or triple-axis neutron scattering apparatus at atmospheric pressure. Anyhow the main use of this measuring systems are of course standard technological applications such as machine tools or robotics. They were constructed for this purpose and consequently none of them is suited for an UHV application due to the use of strongly degassing materials. We therefore transformed such a commercially available system to make it adequate to UHV-applications.

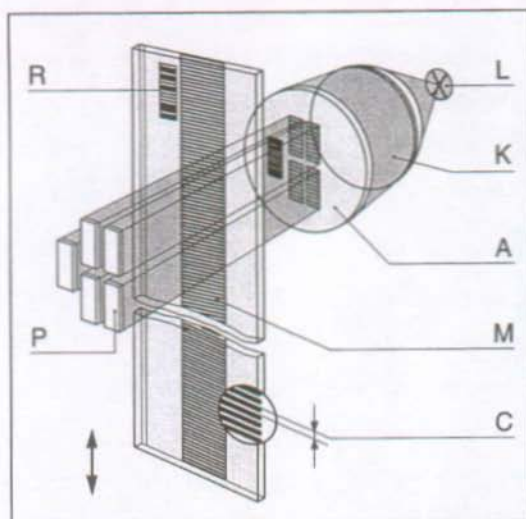
It goes without saying that this new type of UHV sample position control might not only have a certain impact on Helium-Atom-Scattering but also on other surface science techniques requiring high angular resolution such as angle resolved electron spectroscopies or ion scattering. One might even think on industrial applications. In semiconductor technology, for example, most processing steps needing high position resolution such as the photoresist light exposure are so far done at atmospheric pressure. With the advent of novel techniques such as x-ray lithography at XUV-synchrotron radiation facilities, however, precise production steps under UHV conditions become important.

### **The electro-optical position measuring technique**

Among the various options that can be found on the market we gave preference to the electro-optical measuring system over methods using light diffraction or induction phenomena, because it provides higher resolution combined with great reliability [Ern93].

The basic scheme of this method is shown in Fig. 3.10 . A parallel polychromatic light beam is furnished by a special bulb (L) and a condenser lens (K) and is directed towards a glass plate (A). The glass plate supports five arrays of parallel absorption line gratings made by chromium metal evaporation. Four of them are grouped together. We will first discuss their mode of action. They provide the relative angular position measurement. The gratings in each array are periodic with a ratio of 1:1 between the widths of transmitting and non-transmitting regions. They have the same periodicity, but there is a phase shift of  $90^\circ$  from one array to the next. A second glass plate which is mounted on the moving object is installed in front of the first glass plate with a distance of about  $100\text{ }\mu\text{m}$ . It supports the same periodic line grating. When sliding the second glass plate with respect to the first one the light transmission through both glass plates varies sinusoidally. This is detected independently for the 4 different arrays by 4 photo diodes. The signal of each diode consists of a sinusoidal portion which is superimposed by a constant background. Subtracting the signals from two arrays with a phase shift of  $180^\circ$  eliminates the constant signal and provides a symmetrical sinusoidal-like signal. This can be done for two of those pairs of arrays with  $90^\circ$  phase difference. Both signals are converted to rectangular signals and read by a counter leading to four count-events per grating period. Thus, the corresponding resolution is  $1/4$  times the grating

a)



b)

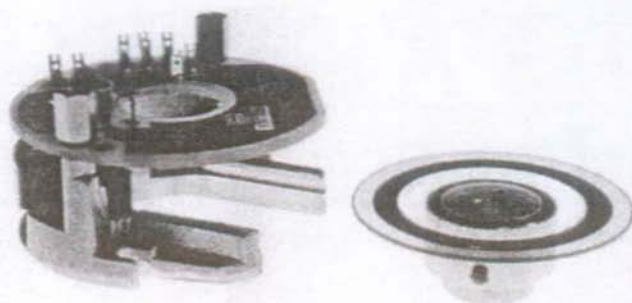
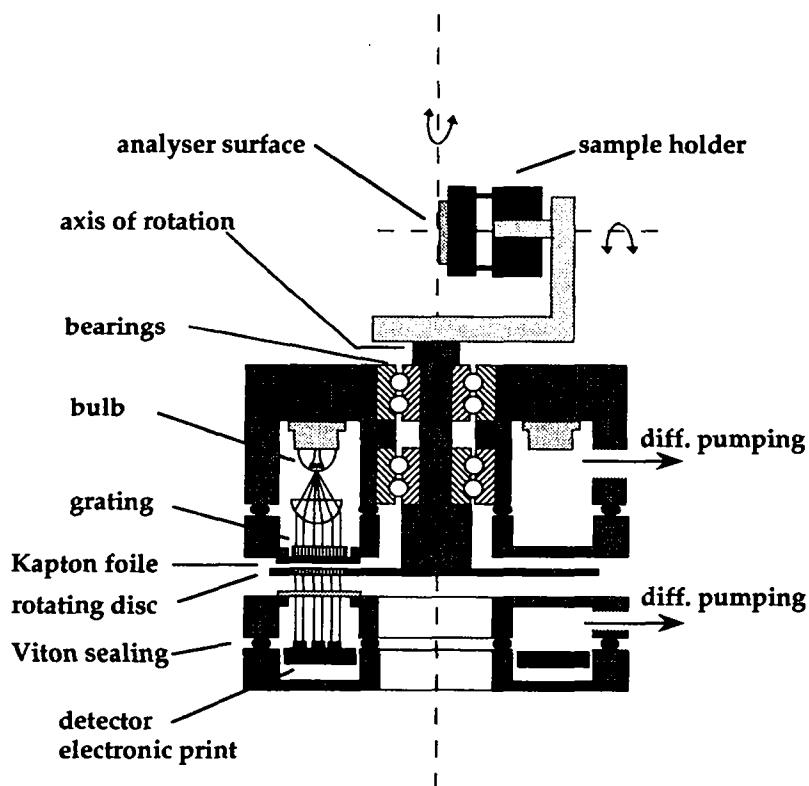


Fig. 3.10 : a) Schematic illustration of the electro-optical position measuring technique (from[Ern93]), b) photo of the commercially available angle measuring system [Hei93].

periodicity. But it is also possible to take into account the phase information of the measured signals. Then the resolution can be increased by a factor up to 100 by an interpolation process described in reference [Ern93]. The electronics is additionally able to determine the direction of the motion. Modern micro-structuring techniques nowadays allow for grating periodicity's down to 4  $\mu\text{m}$  and, therefore, for resolutions in the sub-micron regime. In our case 2500 lines are arranged at the outer border of a turning glass disc giving rise to a theoretical angular resolution much smaller than 0.001°. Fig. 3.10 b) shows (a photo of) the ready-to-use angle measuring system bought from Heidenhain GmbH [Hei93]. It consists of the light source including the condenser lens and the first glass plate, the detector with electronic print and the rotating disc. All parts are perfectly aligned by the supplier. Since the light source and the detector electronic print can not be used in UHV, they have to be separated, independently encapsulated and differentially pumped, whereas the disc has to be mounted in UHV onto the axis of rotation. Besides the re-aligning, the crucial point thereby is to maintain the tiny distance of 100  $\mu\text{m}$  between the two glass plates because any increase of this distance will smear out the light signal due to the final angular divergence of the incoming light beam.

We solved this problem by intercalating an almost transparent 25  $\mu\text{m}$  thick KAPTON foil between the two glass plates. This can be seen in the section view of our mechanical set-up given in Fig. 3.11 . The KAPTON foil is attached to the metallic housing of the light source by an UHV compatible polyester glue. (It has been a general result of our investigations that such adhesive connections have leak rates smaller than  $1.0 \times 10^{-9}$  mbar l/sec). The two housings can be opened to become accessible to the light source and the detector. They are sealed by outgased VITON O-rings. The glass disc is

rigidly mounted on the polar axis of rotation which is guided in two bearings before being attached to the crystal holder.



**Fig. 3.11:** Section view of the transformed incremental angle position measuring device (see text).

The whole device is mounted onto a commercial UHV manipulator. The polar angle rotation is driven by a spring loaded metal cable assembly via a step-motorised translational feedthrough. Its computer control is done by means of an algorithm taking each time in account the difference between the nominal and the actual value. Data acquisition takes only place when this difference is smaller than a chosen tolerance.

The bake-out of the analyser chamber containing the angular positioning device *has to be performed at temperatures below 100°C in order to avoid damages of the measuring unit.* Nevertheless, after 3 days at 95°C and half a week of additional pumping time the base pressure has routinely been in the low  $10^{-10}$  mbar range.

We will now demonstrate the high performance of the above described method for the determination of **relative** angular positions. For this purpose a high resolution scan of a Pt(997)-diffraction peak with a step width of  $0.02^\circ$  (Fig. 3.12 a), open circles) has been repeated by a similar scan (Fig. 3.12 a), filled circles) whose data points have been shifted by  $0.01^\circ$  with respect to the first one. The tolerance in both scans was  $0.004^\circ$ . In between these two scans arbitrary angle movements greater than  $50^\circ$  have been performed. It can be nicely seen, that the two scans are exactly shifted by  $0.01^\circ$  and filled and open circles are strictly alternating.

A discussion of this result will be given later, because we will first demonstrate the performance of the **absolute** angle measurements. For this purpose we go back to the description of the incremental measuring system or, more precisely, to the mode of action of the fifth array on the first glass plate, so far not discussed. Actually, it enables the user to refine the absolute angular position once the measuring system had been interrupted. Its



grating is not periodic, but it consists of a special sequence of lines with varying widths. Also does the reference grating (R) on the second glass plate. Moving these two gratings against each other gives rise to a well defined single peak of the detector signal. Its maximum is electronically identified to an internal reference value plus an user offset. The corresponding resolution is about 1/20 times the grating resolution, thus  $0.0072^\circ$  in our case.

Fig. 3.12 b) shows the second scan of Fig.3.12 a) (filled circles) together with a new scan, performed after having interrupted the measuring system and overpassed the absolute reference signal (open squares). The data points of the new scan have again been chosen to be shifted by  $0.01^\circ$  with respect to the preceding scan. This results once more in a perfect alternation of the filled circles and open squares in Fig. 3.12 b). Thus, the reproducibility of absolute angular positions is better than  $0.01^\circ$ .

### Discussion:

It has been shown that the **absolute** angular positions can be reproduced within an error of  $0.01^\circ$ . This is close to the theoretical limit of the electro-optical method and by far means sufficient for most UHV applications such as angle resolved scattering experiments. This also holds for double axis helium scattering using nanoscopic blazed gratings operating with an energy resolution of about 0.5%. If higher reproducibilities are needed one has to pass over to an internal calibration with a permanent control of relative angular movements. In this mode, the measuring electronics might never be interrupted. In regard of the theoretical resolution limit of  $0.00036^\circ$  of this mode the spring-loaded cable assembly drive is certainly the main

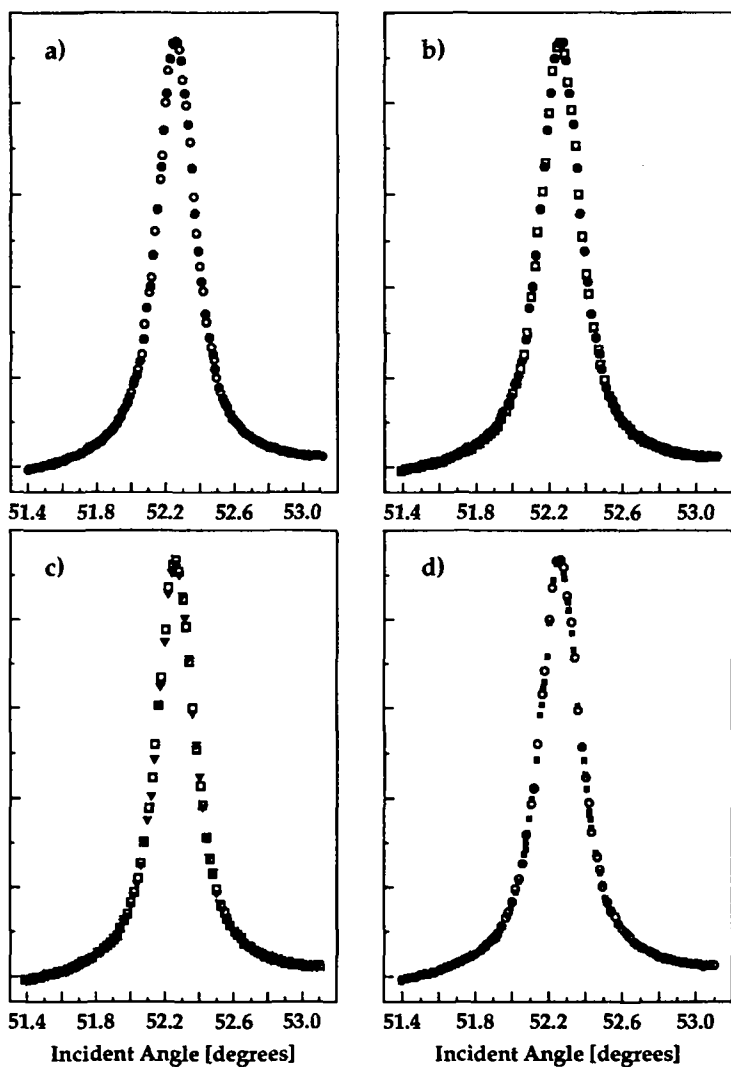


Fig. 3.12 : High resolution diffraction scans from the Pt(997) analyser surface obtained with a room temperature beam. a) demonstration of the high reproducibility of relative angular positions, b) demonstration of the high reproducibility of absolute angular positions, c) and d) precision of backward and random repetitions of angular scans.

resolution limiting factor. This can be seen from Fig. 3.12 c) where the second scan of Fig. 3.12 b) (open squares) has been repeated in the opposite scanning direction (filled triangles). In this scanning direction small angular changes during the acquisition of the data points can occur due to relaxation within the cable assembly leading to the minimal data spread seen in Fig. 3.12 c). We could avoid this effect by working with tolerances lower than  $0.002^\circ$ . But the time needed to adjust the angular position for one data point exceeded two minutes. Improvements of both the mechanical drive and its computer control will certainly overcome this problem making possible fast scans in any direction with resolutions far below  $0.01^\circ$ .

Nevertheless, the current manipulator set-up already allows for a precise ( $\pm 0.005^\circ$ ) setting of angular positions. This can be seen from the measurement in Fig. 3.12 d) where the measurements of Fig. 3.12 a)-c) have been repeated by a random scan with  $0.003^\circ$  tolerance (small filled squares). Instead of making a directed scan preceding nominal values between  $51.4^\circ$  and  $53.0^\circ$  have been generated with the computer random-generator and transferred to the control program. Despite the permanent movement direction changes no significant deviations from the preceding spectra can be observed (Note, that the random scan is compared to the first scan of Fig. 3.12 a)).

Throughout the forthcoming parts of this thesis we will make several times successful use of this new positioning system by adjusting diffraction peak maxima without further control. Furthermore, smallest peak shifts or changes of the FWHM of diffraction peaks could be determined directly in an absolute way. Finally, it provides the key to a successful and comfortable use of a Pt(997)-analyser as TOF-substitute.

### 3.3.3 Outlook

Although a widespread use of the above presented positioning possibilities can be imagined this outlook exclusively reports about work that is already in progress in order to bring the analyser scanning possibilities to perfection. Having resolved the problem of the precise measurement of the angle of incidence the linear motion of the analyser becomes the crucial point of high resolution  $\Theta/2\Theta$ -analyser scans.

In the present set-up the analyser surface is aligned parallel to the polar axis of rotation by means of laser beam aligning. Together with the high resolution angular position measuring unit it is mounted on a tube that is attached to a standard UHV manipulator containing a x/y/z travel unit as well as a tilt module. This manipulator is connected to the analyser vacuum chamber via a differentially pumped rotational feedthrough that allows for a vertical adjustment of the polar axis of rotation. This is illustrated in the apparatus side view already presented in Fig. 3.6. The linear motion parallel to the He-beam is motorised and can be controlled *ex situ* by a precise linear measuring system that also uses the electro optical measuring technique. The corresponding high reproducibility can be deduced from Fig. 3.13 showing two subsequent shifted scans of the total scattering angle at the analyser. Although this peak is rather broad due to the crystal mosaic spread, it might be stated that the scattering angle can be reproduced better than  $0.01^\circ$ . Together with the high reproducibility of the polar angle rotations this allows for almost perfect  $\Theta/2\Theta$ -scans. This has been verified by performing  $\Theta/2\Theta$  scans using the specular peak of a Pt(111) surface. Thereby it turned out that the peak positions only vary about  $\pm 0.02^\circ$  with respect to their nominal values. But the intensities did not show the

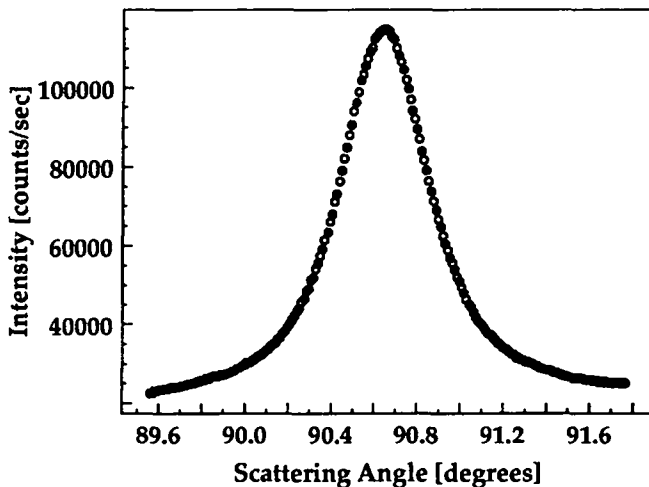


Fig. 3.13 : High resolution scans of the total scattering angle at the analyser surface performed by a translational motion parallel to the He-beam.

expected behaviour. The reason for this is twofold. In a first place mechanical instabilities of the conventional UHV manipulator during the linear motion give rise to slight tilt angle changes <sup>1</sup>. Secondly, the linear motion is not perfectly parallel to the incoming He-beam since the manipulator is rigidly connected with the vacuum chamber. Therefore different areas on the analyser surface owing different properties are involuntarily probed during a  $\Theta/2\Theta$ -scan. Fig. 3.14 shows how these problems will be surmounted in the near future by a new home built

---

<sup>1</sup> These intensity variations are only important in inelastic experiments. Throughout this thesis we could work during one week without readjusting the tilt angle.

manipulator. Its design is again inspired by the mechanical set-up of state-of-the-art x-ray surface diffractometers [Rob86]. The basic idea is the use of robust positioning devices from outside the vacuum. The long tube with the simple manipulator is reinforced. It is directly attached to a standard circle segment of a x-ray (or neutron) diffraction goniometer that is mounted on a industrial high precision x/y/z-linear motion device. The analyser surface is exactly positioned in the centre of the circle described by the circle segment. Linear motion parallel to the He-beam is provided by simultaneous accommodation of the x,y and z positions. Even the tilt angle can automatically be optimised at each scattering angle by rotating the circle segment. Finally a second UHV compatible angle position measuring device will be installed for the control of the azimuthal angle.

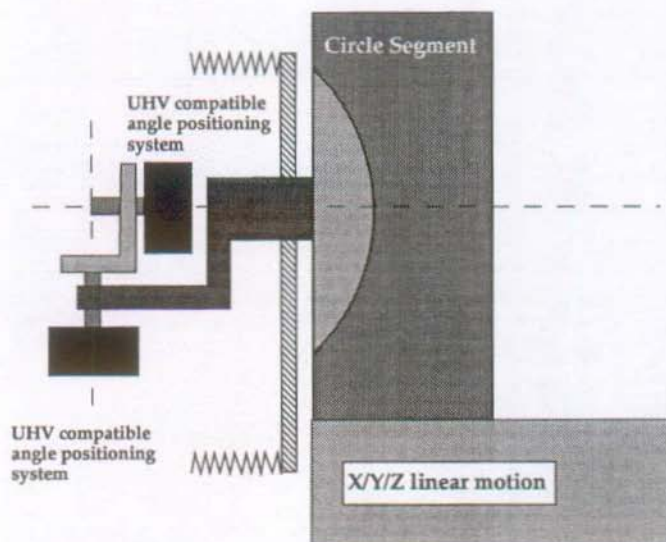


Fig. 3.14 : Schematic sketch of the future analyser manipulator. Precise movements parallel to the He-beam are provided from outside the vacuum by standard industrial linear motion devices and a circle segment.

### 3.4 Apparatus characteristics

#### 3.4.1 He-beam characteristics

Tab. 3.1 shows experimentally determined beam characteristics for some typical nozzle parameters used in this work.

$T [K]$	$P [bar]$	$\lambda [\text{\AA}]$	<i>Gaussian</i> $\Delta\lambda/\lambda$	<i>Matrix</i> $\Delta\lambda/\lambda$	<i>Energy</i> [meV]
320	250	0.525	1.6 %	1.5 %	74.8
95.0	140	0.959	1.4 %	1.3%	22.4
89.4	85	1.01	0.6%	0.7%	20.2
89.4	22	1.05	1.4%	1.4%	18.7
92.0	12	1.01	2.5%	2.5%	20.2
50.0	15	1.53	0.8%	0.7%	8.8

**Tab. 3.1 :** Beam characteristics for some typical source parameters used in the present work. The wavelength spreads have been obtained by fitting Gaussians to diffraction peaks (see equation 2.4.9) as well as by using the matrix-optics method described in Sec. 2.4 .

The wavelengths were determined by evaluating various diffraction scans taken from the Pt(997) surface or from an oxygen p(2\*2) superstructure on the Pt(111) "analyser" surface.

The velocity spreads ( $\Delta\lambda/\lambda$ ) have been determined by evaluating the diffraction peak widths. Thereby scanning the primary beam provides a

reliable help since it directly determines the pure geometric contribution to the peak broadening. The open squares in Fig. 3.15 show such a scan together with its Gaussian fit (straight line). The FWHM is  $0.139^\circ$ . This has to be compared with the theoretical result for the geometrical angular broadening discussed in Sec. 2.4. Since the measurement has been done with specular scattering from a Pt(111)-"analyser" surface, equation (2.4.7) does not really hold. It only describes the case of a single slit diaphragm that is insensitive to the direction of the incoming beam whereas, the experimental set-up corresponds to a direction sensitive detector. Fortunately equation (2.4.7) can be modified for the case of two aligned diaphragms [Kuh91] which does not principally differ from our set-up containing two diaphragms and a simple mirror. The modified equation (2.4.7) yields an angular broadening  $\Delta\vartheta_f$  that is somewhat smaller ( $\sim 90\%$ ) than the measured FWHM. Since the exact meaning of  $\Delta\vartheta_f$  is not strictly defined we always multiplied it with a constant factor in such a way that the theoretical angular broadening matches the measured geometrical angular FWHM of the primary beam. The determination of  $\Delta\lambda/\lambda$  is now straightforward. For each wavelength the FWHM of diffraction peaks taken at the *in-phase condition* of the Pt(997) sample is determined by Gaussian fits. This is shown by the open circles and the straight line in Fig. 3.15 for the case of a nozzle that is operated at  $P_{\text{nozzle}} = 12$  bar and  $T_{\text{nozzle}} = 92$  K ( $\lambda = 1.01\text{\AA}$ ). The velocity spread  $\Delta\lambda/\lambda$  can be extracted from equation (2.4.9) by taking into account the geometric angle broadening that corresponds to the new scattering position. In the example of Fig. 3.15 this new theoretical geometric broadening is more than 20% (FWHM =  $0.108^\circ$ ) smaller than at  $180^\circ$  (FWHM =  $0.139^\circ$ ). Nevertheless the comparison of the scan of the primary beam and the diffracted beam in Fig. 3.15 gives a good idea of the



dispersion smearing contribution to the peak broadening. The velocity spread in the given example is 2.5%.

The values for  $\Delta\lambda/\lambda$  shown in Tab. 3.1 nicely agree with the values obtained from similar beam sources [Bru77,Ker85] by TOF-measurements. Nevertheless we additionally checked them by means of the matrix-optics method described above. Reversely this provides a good test of this new method. The result of the simulation is shown by the dashed lines in Fig. 3.15 . Apart from the geometrical apparatus dimension and a Gaussian wavelength distribution no further assumption has been made. Let us first discuss the simulation of the primary beam peak at  $180^\circ$ . Whereas its central part is almost perfectly described great differences occur at the peak bottom. This is due to the difference between perfectly aligned diaphragms in the simulation and slightly misaligned slits in the experiment. Additionally the circular ( $\varnothing$  0.3 mm) diaphragm **d1** (see Fig. 3.2) has been replaced in the calculations by a rectangular slit (0.23 mm) providing the same effective beam divergence. In the simulation beam truncation gives rise to the sharp intensity drop at the peak wings. This drops are cancelled out by the dispersion smearing during diffraction as can be seen from the fit of the diffraction peak . The peak shape becomes nearly Gaussian. More important, the velocity spread obtained by the matrix-optics method is again 2.5%, as in the former case.

Tab. 3.1 shows as well the  $\Delta\lambda/\lambda$  - values obtained by fitting Gaussians as the results obtained by the matrix-optics method. Although little differences can occur, both methods approximately reveal the same results.

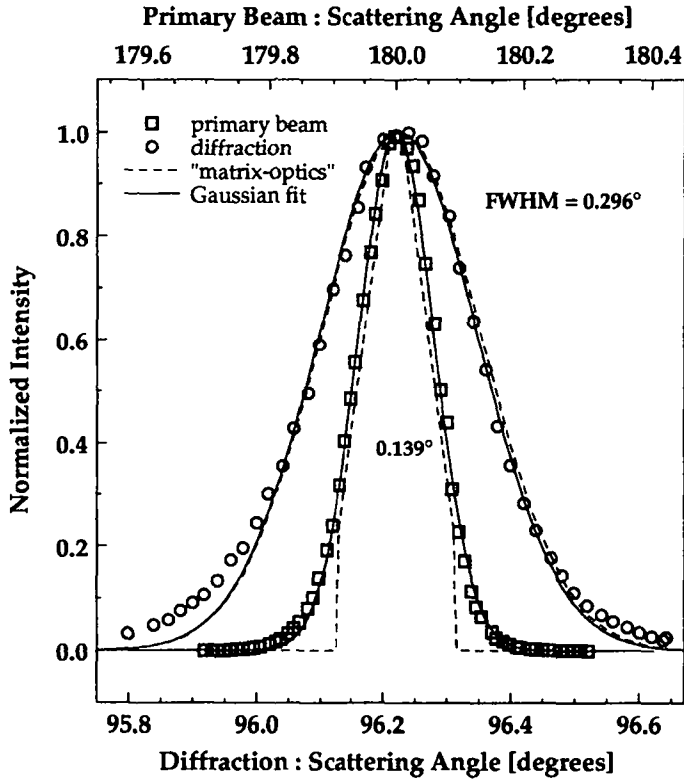


**Fig. 3.15** : Fit examples for the determination of the primary beam velocity spreads. Open squares: scan of the direct beam at 180°; open circles :  $n=-3$  diffraction order measured with a beam with  $\lambda = 1.01 \text{ \AA}$ ; straight lines : Gaussian fits; dashed lines: fits by the matrix-optics method.

### 3.4.2 Spectrometer resolution in inelastic experiments

In this section the energy resolution of inelastic experiments will be discussed according to the method described in Sec. 2.4.2. The analyser resolution within this method has been defined as

$$\frac{\Delta\lambda}{\lambda} = \frac{\lambda_{\max} - \lambda_{\min}}{\lambda_0}$$

where  $\lambda_{\max}$  and  $\lambda_{\min}$  denote the extreme wavelengths that are able to pass the analyser at given analyser scattering geometry corresponding to  $\lambda_0$ . At a given apparatus size the resolution crucially depends on the beam divergence determined by the size of the diaphragm **d1** (see Fig. 3.2) and the sizes of the diaphragms **d2** and **d3** in front of and behind the analyser surface. This is demonstrated by the theoretical resolution shown in Fig. 3.16 a) as a function of the beam divergence. The analyser scattering geometry corresponds to the  $n = -3$  diffraction order for  $\lambda_0 = 1.0 \text{ \AA}$ . The resolution has been calculated for a fixed sample scattering angle of  $90^\circ$  and three different incident angles ( $\vartheta_i = 45^\circ$  (straight line),  $\vartheta_i = 55^\circ$  (filled circles) and  $\vartheta_i = 35^\circ$  (open squares)). The size of the diaphragm **d2** ( $d_3 = d_2$ ) has been chosen to be 0.175 mm, 0.35 mm and 0.7 mm as it is also indicated in Fig. 3.16. As expected, the resolution decreases with an increasing incoming beam divergence. The smaller the sample incident angle the better is the analyser resolution. At zero divergence the differences between the resolutions at different incident angles is zero, and the resolution is entirely determined by the size of the diaphragms **d2** and **d3**. In view of an aimed resolution of  $\Delta\lambda/\lambda = 1\%$  we installed a fixed diaphragm **d1** that provides a beam divergence of  $0.077^\circ$ . The fixed sizes of **d2** and **d3** are 0.35 mm and 0.38 mm, respectively. This gives rise to a theoretical resolution between 1.2 % and 1.8 % as it can be revealed from Fig. 3.16 a). Note that these values are only a lower limit for the apparatus resolution and that the resolution can

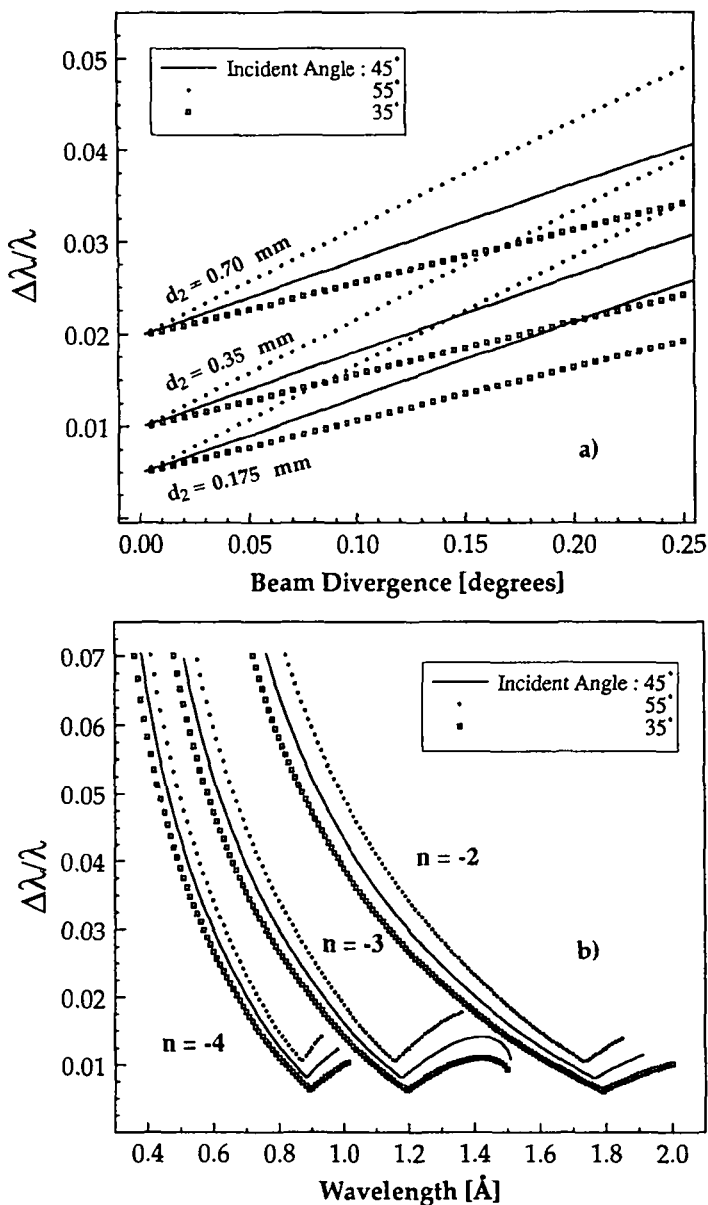


Fig. 3.16 : Theoretical determination of the apparatus resolution for inelastic experiments (see text), a) resolution as a function of the incoming beam divergence, b) resolution as a function of the analyser pass-energy.

be much better depending on the kind of inelastic scattering processes. The diaphragms are installed in such a way that they provide the only vacuum connection between adjacent vacuum chambers making possible an optimal differential pumping.

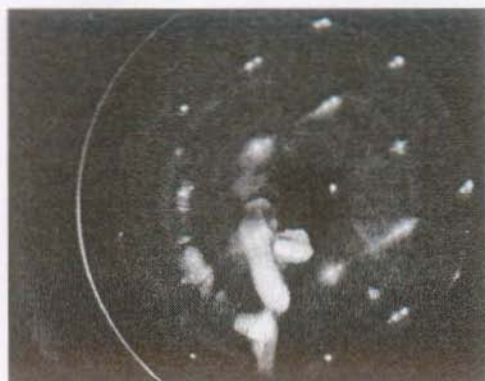
So far we have only shown the analyser resolution at a fixed wavelength of 1.0 Å. What happens during an inelastic experiment when the analyser pass energy is changed at a given sample scattering geometry and fixed aperture sizes? Fig. 3.16 b) shows the corresponding simulations for the same angles of incidence as in the case of the calculations of Fig. 3.16 a). The resolution strongly depends on the He-wavelength. Small wavelengths demand a use of high diffraction orders to get a resolution of the order of  $\Delta\lambda/\lambda = 1\%$ .

Summing-up it can be said that the fixed aperture sizes installed in our apparatus provide an over-all analyser resolution between 0.7 % and 3% if one works with standard scattering geometries and appropriate analyser diffraction orders. Additional slit diaphragms with sizes between 25  $\mu\text{m}$  and 200  $\mu\text{m}$  are mounted on linear feedthroughs and can be slid into the beam giving rise to increased resolutions.

### 3.5 Surface and system preparation

During this thesis two Pt(997) crystals (Pt(997)A and Pt(997)B) have been prepared. They were oriented, cut by spark erosion and polished to the desired orientation within  $\pm 0.1^\circ$ . They were cleaned by repeated cycles of argon ion bombardment (ion energy: 750 eV) at about 750 K and subsequent annealing at about 850 K for more than 15 minutes. This procedure resulted in a sharp LEED pattern with hexagonal symmetry and a typical energy dep-

a)



b)

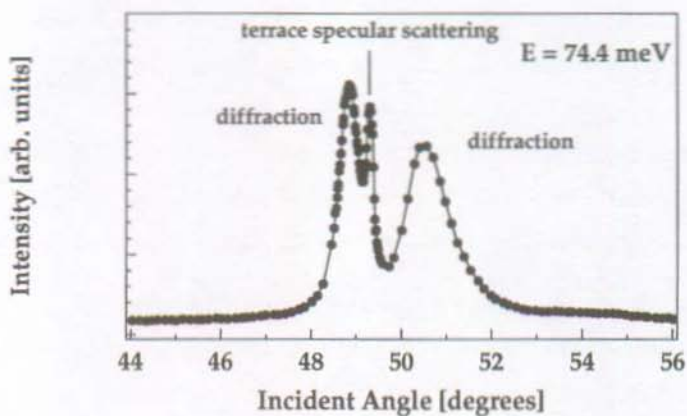


Fig. 3.17 : a) LEED pattern obtained during the initial stage of the surface preparation of Pt(997), an ordered step arrangement is indicated by the typical spot splitting. b) He-diffraction spectrum obtained from Pt(997) during the initial stage of the surface preparation demonstrating the existence of large facets.

endent spot splitting, as expected for a regularly stepped surface [Zan88]. Fig. 3.17 a) shows such a LEED pattern that has been obtained with a electron beam energy of 210 eV. However the presence of LEED spot splitting is no definite proof of a well ordered surface. This can be concluded from the He-diffraction scan in Fig. 3.17 b) that has been taken during the initial stage of the surface preparation where the surface already shows the LEED spot splitting. Apart from broad diffraction features an intense peak corresponding to non-diffractive terrace specular scattering occurs. It is due to the formation of large (111) terraces caused by bulk and surface contaminations. Generally, the Pt(997) surface turned out to be highly instable towards faceting in the presence of impurities. Therefore extended cycles of sputtering and annealing are required for the preparation of a well ordered surface.

The He-diffraction data shown in Sec. 2.2.3 and in Sec. 4 have been taken from Pt(997)A mounted at the sample position, whereas Pt(997)B has been used as analyser surface in the monochromatization experiment presented in Sec. 5. Unfortunately it turned out that the crystal Pt(997)B has a mosaic spread of the order of  $0.13^\circ$ . It is thus unsuitable for a further successful use as He-beam analyser and will be exchanged in the near future.

During the early stages of the apparatus construction a Pt(111) surface has been used as "analyser" surface to reflect the He-beam into the detector. It has been prepared in the standard way by repeated cycles of sputtering (750 K) annealing (1250 K) and exposing in an oxygen atmosphere at  $T = 800$  K resulting in a well ordered surface, as it can be revealed from the diffraction scan already shown in Sec.3.2.4.

An ordered oxygen  $p(2 \times 2)$  super-structure on Pt(111) has been used as dispersive analyser grating in the monochromatization experiments presented in Sec. 5.1. Certain care has been taken to prepare well ordered oxygen overlayers in order to detect the tiny diffraction peak narrowing upon monochromatization. Different recipes for the preparation of  $p(2 \times 2)$  O/Pt(111) can be found in literature [Leh82,Ker86]. Following a recipe given by Neuhaus [Neu90] the  $p(2 \times 2)$  oxygen overlayers were prepared at 420 K and kept in a constant oxygen atmosphere of about  $5.0 \times 10^{-7}$  mbar. Fig. 3.18 a) shows a diffraction scan including the specular peak and the  $(\frac{1}{2}, \frac{1}{2})$  diffraction peak into the  $\langle 11-2 \rangle$  substrate direction (extended polar angle scans revealed up to 8 visible diffraction orders). The  $(\frac{1}{2}, \frac{1}{2})$  diffraction peak is superimposed on a flat background and its FWHM is only  $0.02^\circ$  larger than the FWHM of the specular peak (FWHM =  $0.09^\circ$ ) indicating large overlayer islands of the order of 500 Å. The formation of this extended islands happens on a large time scale as it can be deduced from the oxygen up-take curves in Fig. 3.18 b) that have been measured using the specular peak, the (1,1) diffraction peak and the half order diffraction peak. Oxygen adsorption at 420 K and a oxygen partial pressure of  $3.7 \times 10^{-7}$  mbar leads to a dramatic drop of the specular intensity due to the adsorption of isolated oxygen atoms on identical adsorption sites. This can be concluded from the up-take curve measured on the (1,1) diffraction peak. Its intensity immediately increases with the beginning oxygen exposure and reaches relatively soon a saturation value. The intensity of the half order diffraction peak, however, increases only very slowly during about 1 hour indicating a slow formation of large oxygen islands. This behaviour is reflected in the full-widths at half maximum of the diffraction peaks. Whereas the FWHM of the (1,1) diffraction peak remains small upon oxygen exposure the half order diffraction peak is initially broad and becomes smaller with increasing



island sizes. At the end of the overlayer formation no difference between the FWHMs of the (1,1) and the  $(\frac{1}{2}, \frac{1}{2})$  diffraction peak can be observed. Therefore we could use the intense half order diffraction peak for the monochromatization experiment.

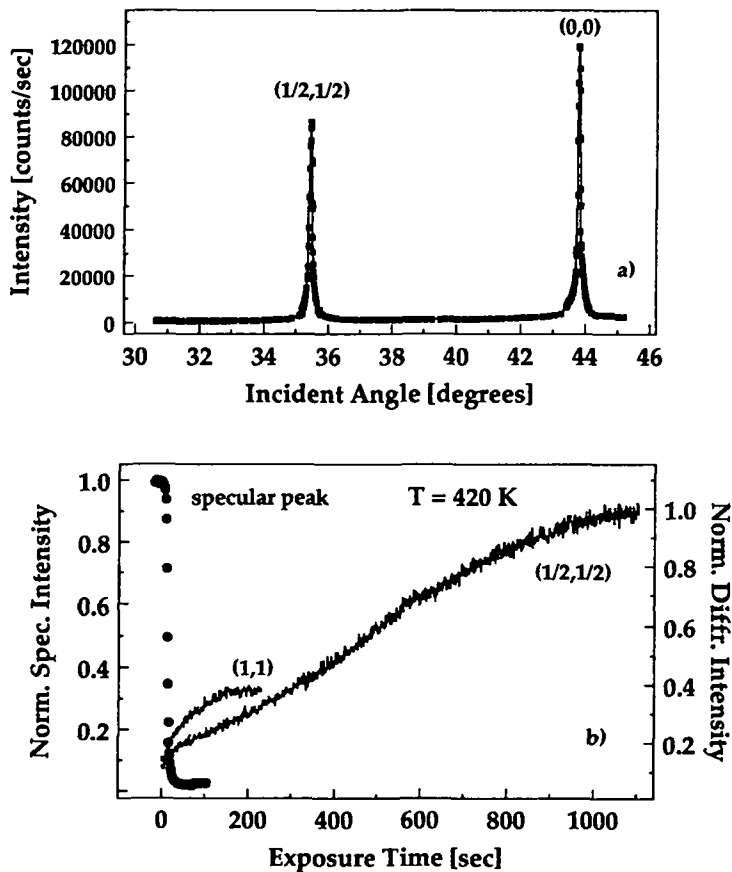


Fig. 3.18 : a) He-diffraction scan from  $p(2 \times 2)$  O/Pt(111) into the  $\langle 11-2 \rangle$  substrate direction ( $E = 20.2$  meV, scattering angle:  $87.65^\circ$ ), b) oxygen up-take curves measured with the specular peak, the (1,1)- and  $(1/2, 1/2)$ -diffraction peak,  $T = 420$  K,  $P_{O_2} = 3.7 \times 10^{-7}$  mbar

## 4 Pt(997) (and Pt(111)) as atom-optical device

The He-diffraction measurements of Sec. 2.2.3 revealed that the Pt(997) surface acts as almost perfect nanoscopic blazed grating. In this section the atom-optical properties of the Pt(997) surface will be discussed in more detail by additionally taking into account the consequences of surface and crystal imperfections. The present measurements have again been performed with the Pt(997) surface (Pt(997)A) at the sample position in the scattering chamber and a simple Pt(111)-mirror to reflect the beam into the detector.

### 4.1 The Pt(997) analyser dynamics

The Pt(997) surface can be considered as a powerful filter for wavelengths that match equation (2.3.1) if the in-phase scattering position of adjacent terraces is fulfilled. It would be possible to demonstrate this by varying the beam energy at a fixed terrace specular scattering condition, i. e. by so called drift-measurements. In apparatus with fixed scattering geometries this kind of measurements are often made for the determination of step heights [Wit95] since they scan the perpendicular momentum transfer  $\Delta k_z$  parallel to the terrace normal. Another possibility to scan the perpendicular momentum transfer is a  $\Theta/2\Theta$ -scan. The latter has the great advantage that one can work with constant nozzle parameters whereas the nozzle temperature scan at a fixed nozzle pressure during a drift-measurement inevitably changes the beam characteristics. Since our apparatus allows for independent adjustments of the angle of incident and the total scattering angle, we performed those measurements on the Pt(997) surface. A typical result is shown in Fig. 4.1 as a function of the total scattering angle  $\chi$  ( $\vartheta_i = \chi/2 + 6.45$ ) for  $\lambda = 1.01\text{\AA}$ . Two intense diffraction peaks ( $n = -3$  and

$n = -2$ ) appear at exactly the angular positions that correspond to the in-phase scattering condition. In between no additional features can be observed indicating the almost perfect filtering due to destructive interference. In principle this measurement can be considered as a first  $\Theta/2\Theta$ -energy scan performed with a Pt(997)-analyser since it directly reveals the velocity distribution of the primary beam. According to equation (2.3.1) the FWHM of the peaks has to be of the order of  $1^\circ$  for a primary beam with  $\Delta\lambda/\lambda = 1\%$ . This is nicely confirmed by the data of Fig. 2.1.

In the inset of Fig. 4.1 we show a normalized logarithmic plot of the left part of the  $\Theta/2\Theta$ -scan together with a simple detector diffraction scan that passes the same  $n = -3$  *ideal condition*. Whereas the  $\Theta/2\Theta$ -scan maintains specular scattering with respect to the terraces, the detector scan leaves this condition. Unfortunately, the latter case leads to a stronger intensity decrease when leaving the diffraction peak. This means that anti-phase scattering into the terrace specular direction does not lead to perfect destructive interference.

The reason for this is twofold. In a first place, large terraces that are greater than the apparatus transfer width give rise to ordinary (terrace) specular scattering. As it has been shown in the STM-image from Fig. 2.2.2 c) surface contamination can cause the formation of large terraces. Secondly, the finite terrace width distribution gives rise to a diffraction peak broadening and thus to intensity into the terrace specular direction. This event is additionally favoured by the shape of the terrace form factor. Theoretical diffraction pattern simulations using Pt(997) surface topographies revealed from STM confirm this explanation [Aff94, Mar95].

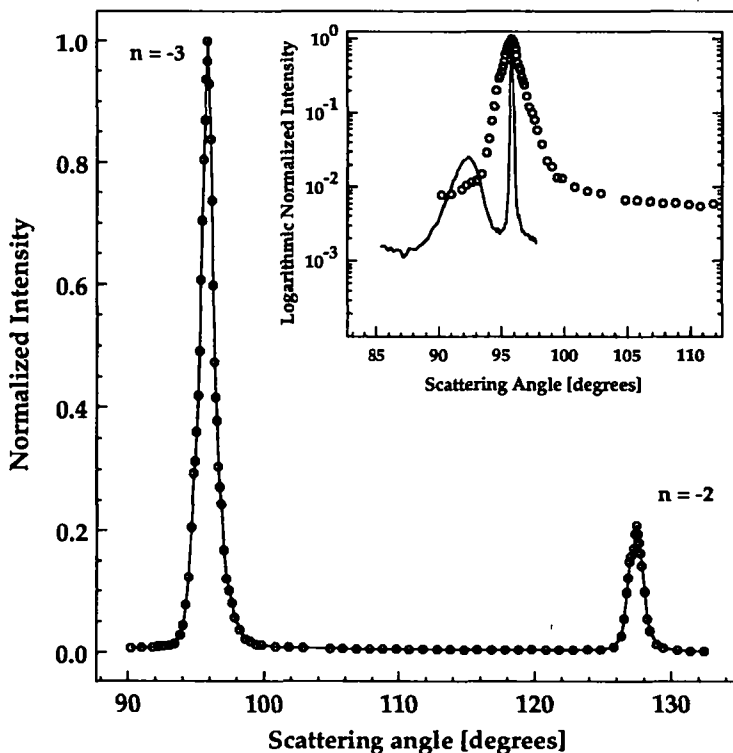


Fig. 4.1:  $\Theta/2\Theta$  - diffraction scan from Pt(997) obtained with a He wavelength of  $1.01 \text{ \AA}$  shown as a function of the scattering angle  $\chi$ .  $\vartheta_i = \chi/2 + 6.45^\circ$ ; inset: logarithmic plot of the  $\Theta/2\Theta$  - scan compared to a simple detector scan that also scans the  $n = -3$  diffraction peak at the in-phase scattering condition.

Obviously, this residual terrace specular scattering limits the dynamical range of a Pt(997) analyser. The intensity between the two diffraction peaks in Fig. 4.1 is about  $5.0 \cdot 10^{-3}$  the intensity of the  $n=-3$  diffraction peak maximum. In terms of an inelastic experiment this means to a first

approximation that an energy loss event containing 5 ‰ of the total flux will have the same intensity as the background.

## 4.2 The analyser resolution

Closely related to the above discussed analyser dynamics is the investigation of the influence of the diffraction peak broadening on the energy resolution. Fig. 4.2 shows seven diffraction scans that have been performed with slightly different He wavelengths by varying the nozzle temperature by steps of 0.5 K leading to relative wavelength shifts of about 0.75 ‰ (the exact wavelengths are indicated in the figure caption). The spectra have been taken under the *ideal condition* for the 50 K beam ( $E = 8.8$  meV). At the given apparatus angular resolution wavelength shifts of 0.75‰ result in distinct peak separations according to the one-dimensional Bragg - equation. The spectra in Fig. 4.2 a) hence nicely visualise the resolving power of the Pt(997) echelette grating. In Sec. 5 even more intuitive measurements showing the wavelength separation upon diffraction will be presented in the framework of a monochromatization experiment.

A considerable peak broadening already occurs at very small wavelength shifts. Apparently it partially cancels out the peak separation by the dispersive diffraction process. Fig. 4.2 b) shows the diffraction peak FWHMs (open squares) obtained by Gaussian fits as a function of the diffraction peak shift with respect to the terrace specular direction. Assuming that the peak broadening due to the finite terrace width distribution adds to the minimum FWHM of the 8.8 meV beam as if they were Gaussians leads to the values of the Excess-FWHMs also shown in Fig. 4.2 b) (open circles). The extra-broadening is always a factor two smaller than the diffraction peak

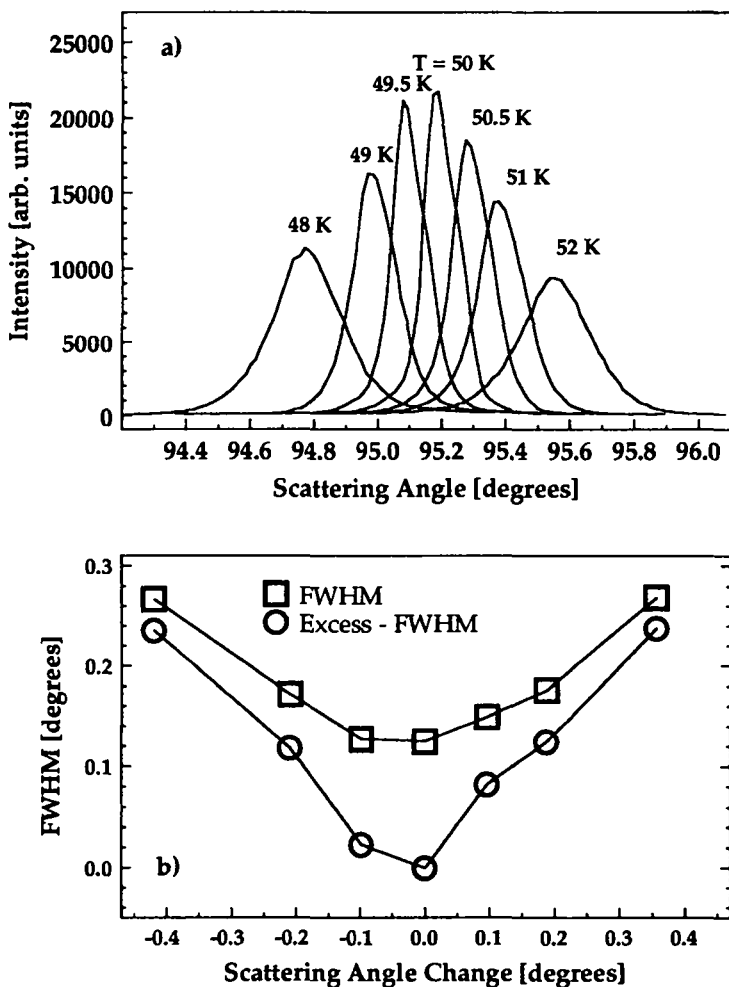


**Fig. 4.2 :** a) detector diffraction scans with varying wavelengths obtained by varying the nozzle temperature: 50K :  $\lambda = 1.53(1)$  Å; 49.5 K :  $1.54(4)$  Å; 49 K :  $1.55(7)$  Å; 48 K :  $1.586(0)$  Å; 50.5 K :  $1.51(8)$  Å; 51 K :  $1.50(6)$  Å; 52 K :  $1.58(3)$  Å. The 50 K beam fulfils the ideal condition.

shift. This means that the theoretical energy resolution is not too much affected by the surface irregularities. But this statement only holds if one carefully works under the *ideal condition* of terrace specular scattering. Any deviation of this condition will lead to a dramatic resolution worsening as it will be demonstrated in the following discussion.

### 4.3 Consequences of the finite terrace width distribution

The above discussed investigation of the energy resolution of Pt(997) blazed gratings has been performed by carefully adjusting the *ideal condition* of terrace specular scattering. Any routine use of a Pt(997) analyser or monochromator will sometime cause a deviation from the *ideal condition*. This will lead to a loss of the apparatus calibration and a worsening of the energy resolution due to the finite terrace width distribution. In this section the latter effect will be quantified experimentally. Note that in the case of a well ordered analyser surface, such as a LiF-surface, the loss of the apparatus calibration would not simultaneously impair the resolution.

Fig. 4.3 a) shows a series of detector scans with different incident angles in the close vicinity of the *ideal condition* for a 8.8meV-beam. The larger the difference between the real incident angle and the incident angle of the *ideal condition* the broader are the diffraction peaks. This is accompanied by a strong intensity decrease. The open squares of Fig. 4.3 b) show the corresponding FWHMs as a function of the diffraction peak position. They were obtained by fitting Gaussians to the curves of Fig.4.3 a). The minimum at about  $95^\circ$  corresponds to the *ideal condition*. Assuming that the extra-broadening due to the finite terrace width distribution adds to the minimum FWHM as if they were Gaussian leads to the values of the extra-broadening shown by the open circles in Fig. 4.3 b). Already a deviation of about  $0.9^\circ$  of the real incident angle with respect to the *ideal condition*

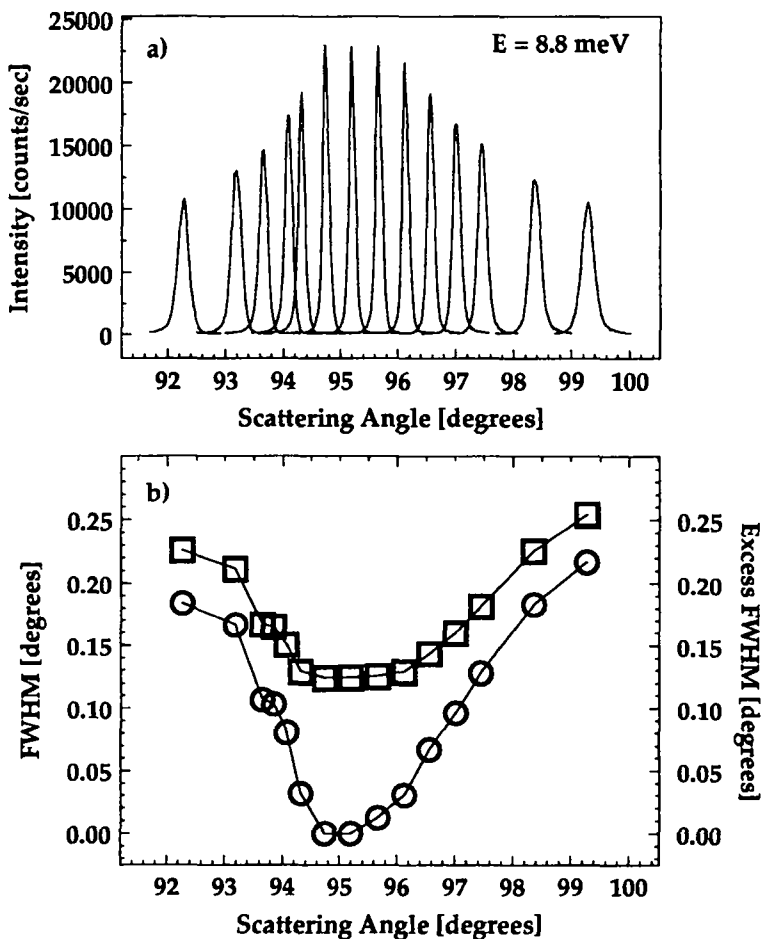


**Fig4.3:** a) High resolution detector scans in the vicinity of the ideal condition of a 8.8 meV He-beam, b) corresponding FWHMs and Excess-FWHMs of the spectra from a) obtained by Gaussian-fits.



causes a extra-broadening of  $0.1^\circ$ . In other words, a deviation of  $0.9^\circ$  already completely cancels out the resolution of a Pt(997) monochromator or analyser which runs at  $\Delta\lambda/\lambda = 1\%$  as it can be seen from equation (2.3.3) .

Fig. 4.4 shows the extra-broadening obtained with a 19.1 meV-beam in the very close vicinity of the *ideal condition* of the  $n = -3$  diffraction order. It is directly plotted as a function of the deviation of the incident angle with

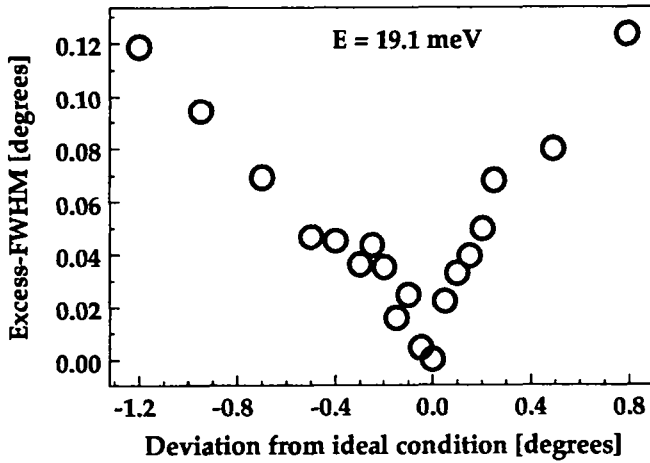


Fig. 4.4: Excess-FWHM due to the finite terrace distribution obtained in the very close vicinity of the  $n = -3$  ideal condition with a 19.1 meV beam plotted as a function of the deviation with respect to the *ideal condition*.

respect to the *ideal condition*. Already a deviation of  $0.1^\circ$  gives rise to an extra-broadening of about  $0.02^\circ$ . This imposes severe requirements for the absolute angular positioning of the Pt(997) surface monochromator or analyser when used at resolutions about 1% and smaller. This is one of the

reasons why we developed the ultra-high precision angular position measuring system explained in Sec. 3.3.2.

The results of Fig. 4.3 and Fig. 4.4 indicate that the extra-broadening is always a factor 5 to 10 smaller than the deviation of the incident angle. This means that at the *ideal condition* the extra-broadening due to the divergence of the incoming beam is always much smaller than the beam divergence. Therefore equation (2.3.3) describing the theoretical energy resolution of Pt(997) blazed gratings still holds for the real Pt(997) surface and the choice of the angular resolution as a function of the desired energy resolution is not affected by the finite terrace width distribution.

#### 4.4 Consequences of crystal imperfections

Any finite mosaic spread of the monochromator or the analyser crystal logically limits the attainable energy resolution, because the wavelength separation furnished by the diffraction process will be partially cancelled out. In this context one has to distinguish between the existence of a few large grains (crystal twinning) and an intrinsic homogeneous smearing of the crystal alignment within a single crystal due to low angle grain boundaries consisting of walls of dislocations [Haa74].

During this work we were faced to both kinds of mosaic spreads, as will be explained next. In a first place, the existence of large grains in the crystal Pt(997)A will be demonstrated. So far no peak splitting could be observed in the presented diffraction scans from this crystal, because we always carefully looked for a non-twisted region on the surface by scanning the sample with respect to the incoming beam. Otherwise the diffraction peaks would generally have a certain asymmetry that is due to crystal twinning. Fig. 4.5

shows a diffraction scan (filled circles) taken after having systematically looked for a surface region where two grains were equally represented. This leads to a distinct peak splitting. Note that this splitting only amounts to  $0.05^\circ$  in a detector scan of the total scattering angle. It would thus be invisible in all current modern high resolution He-scattering machines due to their worse angular resolution. Since the diffraction scan has been taken under the *ideal condition* one has to exclude the existence of large (111) facets which would give rise to a specular peak in the very close vicinity of the diffraction peak. This peak must not shift when the wavelength is changed. We checked this by recording the same spectrum with a somewhat smaller beam energy (dashed curve in Fig.4.5). Clearly the entire peak shifts. Additionally, its splitting becomes invisible due to the peak broadening under the *non-ideal condition*. Thus the splitting is not due to surface imperfections, but is a consequence of crystal imperfections.

By means of the two small curves (small filled squares and small filled circles) of Fig.4.5 it will now be shown that the first curve (filled circles) has been taken from two adjacent grains instead of one single region containing a lot of small grains with two preferential alignments. For this purpose they were obtained by pushing a  $25\text{ }\mu\text{m}$  aperture into the incoming beam giving rise to a  $0.1\text{ mm}$  small illuminated spot on the sample. The location of the spot was altered from one spectrum to the next by sliding the aperture about  $0.15\text{ mm}$  perpendicularly to the beam direction. It can nicely be seen that this gives rise to an alternating selection of one of the peaks that belong to the splitted line-shape of the first diffraction scan taken without diaphragm. Finally we drew back the aperture and looked again for a large enough grain by scanning the sample with respect to the He-beam. The result is also shown in Fig.4.5 by the straight line. The resolution decreasing peak broadening due to the mosaic spread is incidentally visualized.

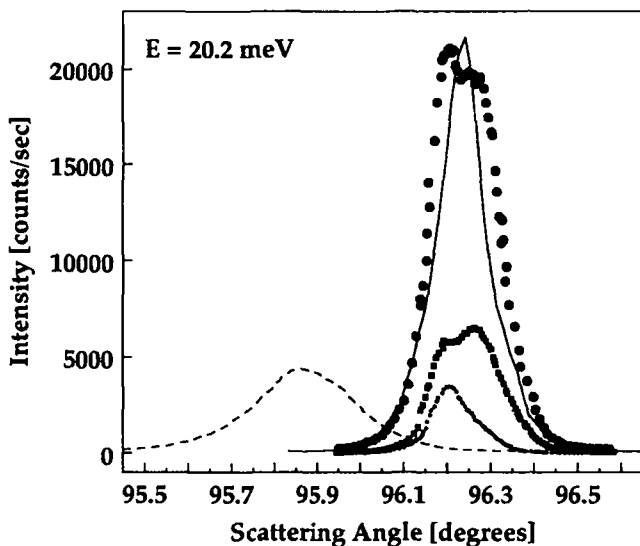


Fig. 4.5 : Diffraction peak splitting due to crystal twinning (see text).

In conclusion it may be said that the problem of crystal twinning or large grains can principally be surmounted by looking for a large enough grain (as we did) or by reducing the size of the incoming beam.

This is not true for resolution limitations which come from a homogeneous mosaic spread caused by low angle grain boundaries. For metals this kind of crystal error is of course always present - even in otherwise perfect single crystals [Guy76]. Therefore the aim of an analyser crystal (not surface!) preparation must be to keep this limitation markedly smaller than the required angle resolution imposed by the aimed energy resolution. A long anneal of single crystals a little below the melting temperature possibly with periodic temperature variation can reduce the grown-in dislocation density in metals by two orders of magnitude [Haa74].

Sandy et al. report on a similar Pt-crystal preparation [San92] which provides a mosaic spread FWHM smaller than  $0.006^\circ$ . This would be small enough for a future use of the Pt(997)-analyser with an energy resolution of  $\Delta E/E = 0.2\%$ .

On the other hand, the several large grains of the crystal **Pt(997)A** already now allow for a resolution  $\Delta E/E$  much better than 1%, since its diffraction peak FWHMs are entirely dominated by the apparatus angular resolution and the dispersion smearing.

Unfortunately, the second Pt(997) crystal (**Pt(997)B**) prepared during this work has a homogeneous mosaic spread of about  $0.1^\circ$ . This has been revealed from systematic scans on the crystal surface. We could not find any region where the diffraction peaks became as narrow as the diffraction peaks from **Pt(997)A**. This had disadvantageous consequences for our double-scattering-monochromatization experiment using two Pt(997) surfaces, as will be discussed in Sect. 5.

## 4.5 Chemical passivation of Pt(997) and Pt(111)

### 4.5.1 Hydrogen Passivation of Pt(997)

A reliable long-time and comfortable use of the Pt(997) grating in a He-surface double axis spectrometer requires its passivation against adsorption of molecules from the residual gas atmosphere consisting mainly of  $H_2$ , CO,  $CO_2$ , and hydrocarbons to a smaller extent. Upon adsorption of 0.05 ML of CO, for instance, the specular reflectivity of the (111) terraces is reduced by 50% [Poe89] due to the large diffusive scattering cross section of the CO molecule [Poe82]. Adsorption of  $H_2O$  or  $CO_2$  has a comparable effect, but they stick to Pt(111) only at temperatures below 150 K [Fis80, Liu91].

On the other hand, a Pt(111) surface covered by a full and ordered (1x1) monolayer of hydrogen has a He-reflectivity of about 80% of clean Pt(111) [Poe86]. Furthermore HAS [Ber87] and RAIRS (Reflection Absorption Infrared Spectroscopy) [Hog88] studies of the  $H_2/CO$ -Pt(111) coadsorption systems revealed a repulsive interaction between the different species within the mixed adlayer. This leads to the formation of high density CO-islands even at low coverages. It could additionally be shown that at very high  $H_2$ -pressures in the 0.001 to 0.1 mbar range the hydrogen induces desorption of preadsorbed CO. Reversely it has been shown that one full (1x1)  $H_2$ -monolayer prevents subsequent adsorption of CO even after extended exposure [Len87].

In their initial *proposal for a novel triple axis He-surface spectrometer* [Kuh92] Kuhnke et al. suggested that these properties can be used for a chemical passivation of Pt(997). Later on this suggestion could be confirmed

by RAIRS (and STM) measurements by Hahn et al. [Hah93]. They showed that at 165K hydrogen preadsorption lowers the CO saturation coverage and the CO sticking coefficient. After predosing the Pt(997) surface with 60.000 L H<sub>2</sub> only a weak absorption band corresponding to a saturation coverage of 0.03 ML step-edge adsorbed CO could be observed in the RAIRS spectra. In addition no morphological changes of the substrate took place upon the hydrogen adsorption as it was revealed from STM. Hahn et al. therefore concluded that the H/Pt(997) surface with  $\Theta_H = 1$  is completely passivated when it is kept at 165 K to minimize hydrogen desorption and to prevent H<sub>2</sub>O sticking through direct adsorption or reaction with the residual oxygen. To conserve the complete hydrogen monolayer the crystal must continuously be exposed to an atmosphere of  $10^{-9}$  to  $10^{-8}$  mbar hydrogen.

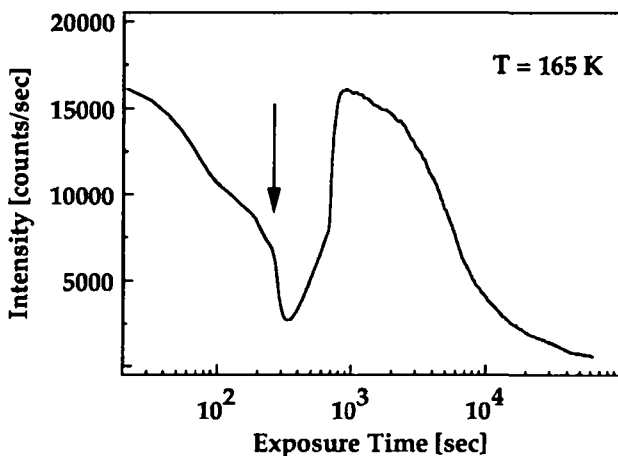


Fig 4.6 : Hydrogen up-take curve from Pt(997) at  $T = 165$  K. Instead of remaining constant the diffraction intensity homogeneously decreases on a long time scale.

Unfortunately we could not confirm this recipe by thermal He scattering as it is shown by the hydrogen up-take curve of Fig. 4.6 which has been taken at  $T=165$  K under an ideal diffraction condition of the Pt(997) surface. During the first 200 seconds hydrogen adsorption takes place from the residual gas during the cooling of the sample from 300 K to 165 K (the  $H_2$  partial pressure of the residual gas was about  $2.0 \cdot 10^{-9}$  mbar). This results in an intensity decrease which becomes greater when the  $H_2$ -pressure is adjusted to a value of  $2.0 \cdot 10^{-6}$  mbar (arrow). The intensity passes through a minimum and increases during the formation of the ordered overlayer. But instead of approaching a final value the intensity passes through a maximum and continues to fall (note the logarithmic scale of the exposure time). This happens within a wide temperature and pressure interval, as it is has been established from a detailed study.

Fig. 4.7 shows as well a diffraction scan (upper curve) taken from the hydrogen covered surface as a scan from the bare surface. The upper curve has been measured several minutes after the maximum of the up-take curve has been reached. Although the peak intensities continuously decreased the over all line shape stayed constant for several hours. The only difference to the spectrum of the pure surface is the inversed population of the diffraction events under *non-ideal* conditions. This can be explained by the differences of the attractive part of the He-surface potentials [Har82]. Thus, at least no dramatic surface structure changes occur upon hydrogen adsorption.

There might be four reasons for this failure of the passivation, as will be briefly discussed. First the 0.03 ML CO saturation coverage observed by RAIRS could be located on the terraces. This seems to be unlikely and does not fit with the CO vibration frequencies obtained from RAIRS. Secondly,



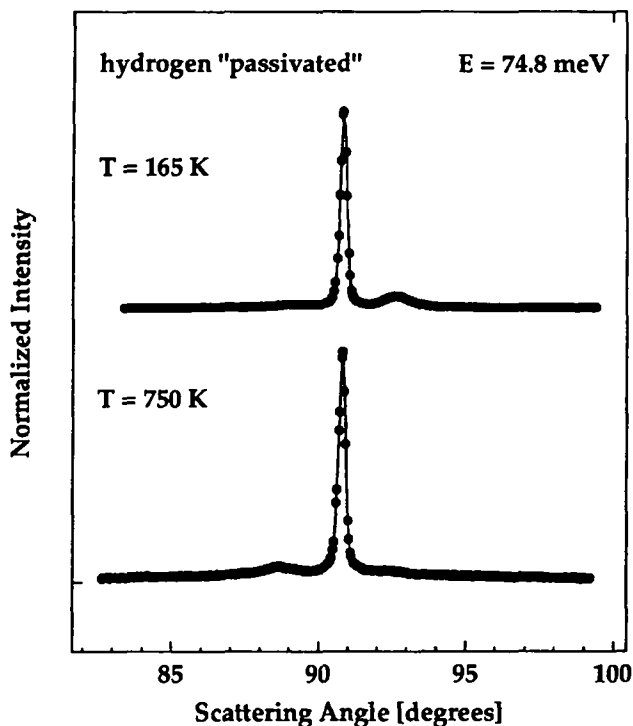


Fig. 4.7 : Comparison between detector diffraction scans taken from a hydrogen passivated surface at  $T = 165 \text{ K}$  and from clean Pt(997) at  $T = 750 \text{ K}$ .

one could deal with a delicate equilibrium situation between the 3D gas and the adsorbed hydrogen. Since the diffraction intensity discontinuously changes upon changes of the hydrogen pressure, we have experimental evidence for this scenario. Nevertheless, we could not find any condition where the intensity remained stable. In their He-diffraction study from H/Pt(111) [Lee83] Lee et al. revealed a disordered and rough hydrogen

overlayer at high exposure times and temperatures below 150 K which is due to hydrogen adsorption on an additional adsorption site ( $\beta 1$ -state). It gives rise to a dramatic drop of the specular intensity. One might speculate, whether this can happen on the (111) terraces of Pt(997) at higher temperatures due to the greater sticking coefficient (also on Pt(111) dissociative hydrogen adsorption is step mediated [Ber75]) or due to slight differences between the terrace-morphologies. Lastly, one has to discuss the influence of the CO-molecules adsorbed at steps, as it has been revealed by RAIRS. The question arises to which amount the diffusive CO cross-section is shielded by the steps and kinks. It can not be excluded a priori that the effective diffusive cross section of a CO-decorated step is greater than the cross-section of the pure step, giving rise to a reduction of the mirror like part of the (111)-terrace. In the case of Ni(100) however the effective size of a step seen by a helium atom decreases with CO-decoration [Ber89].

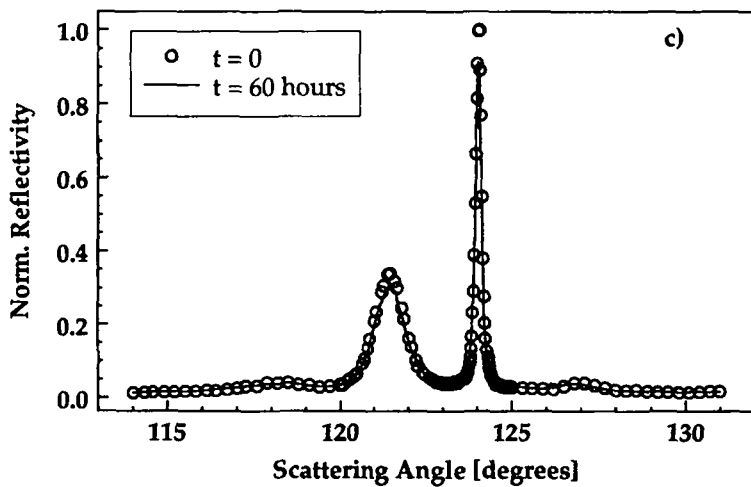
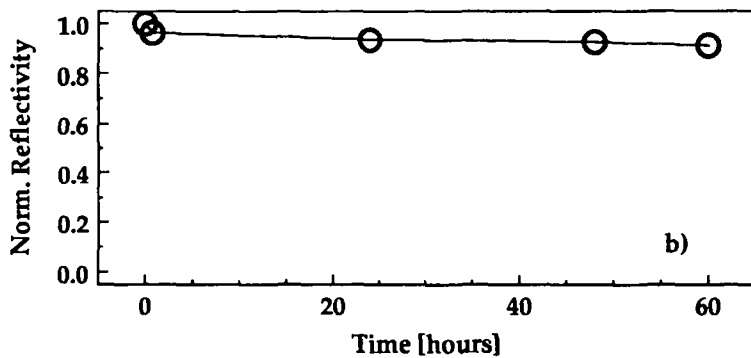
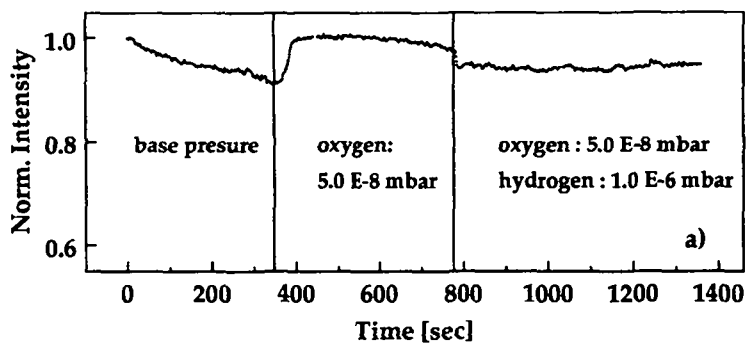
In conclusion, it might be said that chemical passivation seen by RAIRS does not automatically mean morphological passivation as it is probed by Helium-atom-scattering. Additionally, He scattering seems to "see" a surface corrugation introduced by the hydrogen adatoms that can not be resolved by means of STM .

#### 4.5.2 Catalytic Passivation of Pt(997)

In regard of the failure of the hydrogen passivation we developed an in-situ cleaning procedure at high temperatures which works almost perfectly. The surface is kept at 750 K at an oxygen partial pressure of  $5.0 \cdot 10^{-9}$  mbar. Thus, carbon impurities coming from the bulk or from dissociatively adsorbed hydrocarbons are oxidised to CO and desorb. Oxygen adsorption or chemisorption is prevented by simultaneously exposure of the surface to an hydrogen atmosphere of  $5.0 \cdot 10^{-7}$  mbar. By this the oxygen on the surface immediately reacts with the hydrogen and forms desorbing water. This two mechanisms are visualized in Fig. 4.8 a) for somewhat higher pressure values in order to obtain a shorter time scale of these processes. After its preparation the surface initially was kept at 750 K in a normal residual gas atmosphere of about  $5.0 \cdot 10^{-10}$  mbar. This gives rise to an expected homogenous attenuation of the He-diffraction intensity measured under an *ideal condition*. At  $t \approx 350$  sec the oxygen partial pressure was adjusted to  $5.0 \cdot 10^{-8}$  mbar. This is followed by a strong intensity increase due to the removal of carbon impurities. However, after a while oxygen adsorption sets in leading to a homogenous attenuation of the diffraction intensity. This can be stopped by the additional hydrogen exposure ( $1.0 \cdot 10^{-6}$  mbar) at  $t \approx 775$  sec ( the jump in the intensity comes from gas phase scattering of the He-beam with the hydrogen molecules).

---

**Fig. 4.8** (next page): Permanent cleaning of Pt(997) in a mixed hydrogen-oxygen atmosphere; a) visualization of the permanent cleaning; b) normalized absolute reflectivity as function of the cleaning time; c) comparison between detector diffraction scans obtained immediately after the surface preparation and 60 hours later.



In order to measure the characteristics of this in situ cleaning of the surface on a long time scale of several days we made use of the possibility of the apparatus to directly scan the primary beam. This is shown in Fig. 4.8 b). Here the normalised absolute intensity is plotted against the time. Absolute intensity means the ratio between the diffraction intensity and the intensity of the primary beam which have been determined for each data point by subsequent scans of the diffraction peak and the primary beam, respectively. Therefore the results are independent of apparatus instabilities or different adjustments of the detector. During the first half hour the absolute intensity decreases about 3%, but remains almost constant during the following 60 hours. In Fig. 4.8 c) the whole absolute diffraction spectrum immediately obtained after the preparation of the surface (open circles) is compared to the spectrum recorded after 60 hours (straight line). Apart the 9 % peak intensity loss no significant changes can be seen. Therefore neither an important contamination nor a morphological change of the surface occurs during the *catalytic passivation*. As it can be extrapolated from this data the Pt(997) surface can be used for several weeks without significant intensity loss. This is indeed the standard laboratory practice applied with the new He-surface double axis spectrometer.

### 4.5.3 Hydrogen passivation of Pt(111)

During the initial stage of the construction of the new double axis spectrometer a simple Pt(111) mirror has been used as "analyser" surface in order to reflect the beam into the detector. This can already be regarded as a simple albeit important atom optical application of crystal surfaces. Planar or parabolic bended molecular beam mirrors made of crystal surfaces will certainly be a standard optical device in future atom optical applications such as beam focusing [Doa92] or He-microscopy [Lah93]. They will only be useful if it is possible to passivate well ordered low index metal surfaces with negligible corrugation. In this context we studied the passivation behaviour of a H (1x1) terminated Pt(111). Although the diffraction

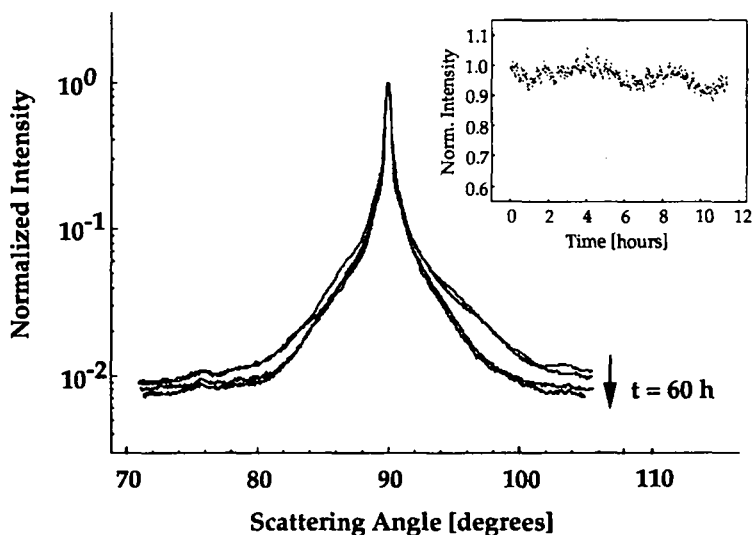


Fig. 4.10 : Subsequent scans during a time intervall of 60 hours from H/Pt(111) at  $T = 165$  K showing the hydrogen passivation (the scans are not taken in a high symmetry direction and therefore do not show diffraction features) ; inset: specular intensity during the first 11 hours of the passivation.

intensities from this system are about 100 times higher than from pure Pt(111) [Lee83] it can still be considered as flat surface with respect to Helium atom scattering. Whereas the method of hydrogen termination did not work for Pt(997) it results in an almost perfect passivation of Pt(111). This can be seen in Fig.4.10 where subsequent scans from (1x1) H/Pt(111) taken at a  $H_2$ -background pressure of  $1.0 \times 10^{-6}$  mbar at 165 K during a time interval of 60 hours are shown. They were recorded at a constant incident angle by varying the scattering angle (note that the differential pumping stage between the analyser and the detector was not yet mounted resulting in a bad dynamics). The specular peak becomes even narrower with time, possibly indicating a slow removal of CO on a long time scale. Since these measurements have been performed on the analyser surface, they could not be done in an absolute way as in the case of the Pt(997) surface. Nevertheless, we believe that the comparison of the subsequent scans in Fig. 4.10 provides a good estimation of the passivation. The intensity far from the specular peak at large parallel momentum transfers is due to incoherent scattering from surface defects. Since this intensity decreases with respect to the specular intensity it can be deduced that the defect density even decreases with time. Fig. 4.10 shows the specular intensity during the first 11 hours after the preparation of the H/Pt(111) surface. Although the intensity oscillates due to teething troubles with the detector during the construction period of the apparatus, no significant intensity loss can be observed.

In conclusion we have shown that the above reported cold passivation of hydrogen terminated Pt(111) permits the use of H/Pt(111) as a molecular beam mirror during more than one week without further preparation of the surface and without important reflectivity loss.

#### 4.5.4 Catalytic passivation of Pt(111)

In regard of the successful catalytic passivation of Pt(997) the question arose whether this concept is transferable to the Pt(111) surface. This would signify a simple and inexpensive (no liquid nitrogen use) alternative to the hydrogen passivation. The loss of reflectivity at 750 K with respect to 165 K due to the Debye-Waller attenuation of elastic diffraction [Bor88] would be partially compensated by the absence of the (1x1) hydrogen layer, which lowers the reflectivity of Pt(111) by 20%.

The same experiment as in the preceding chapter has been performed to demonstrate the catalytic passivation of Pt(111). The result is shown in Fig.4.11. In this experiment the additional pumping stage between the analyser and the detector had already been mounted and the UHV compatible angle position system had been installed.

Apart from the fixed temperature of 750 K the initial passivation parameters were  $p_{H_2} = 1.0 \times 10^{-6}$  mbar and  $p_{O_2} = 5.0 \times 10^{-9}$  mbar. As it is shown in Fig.4.11 the ratio between the intensity at the ends of the polar angle scans ( $\vartheta_i = 70^\circ$  and  $\vartheta_i = 17^\circ$ ) and the specular intensity increases from  $6.0 \times 10^{-4}$  to  $1.8 \times 10^{-3}$  during the first 50.5 hours. Although this is an important increase, the latter still indicates a very clean surface. This is supported by a barely remarkable specular intensity loss. Under this conditions we have used the Pt(111) surface one whole week (or more) without further cleaning. A corresponding reflectivity loss can be observed, but it remains inferior to 25%.

In contrast to the Pt(997) surface a smaller hydrogen pressure causes a damage of the passivation. This can be seen from the penultimate curve (V) which has been obtained 17,5 hours after the preceding one. During this



period the hydrogen pressure accidentally dropped to  $1.0 \times 10^{-7}$  mbar giving rise to an acceleration of the surface contamination. Finally, turning off the oxygen and the hydrogen causes a fast degradation of the surface within a few hours (VI).

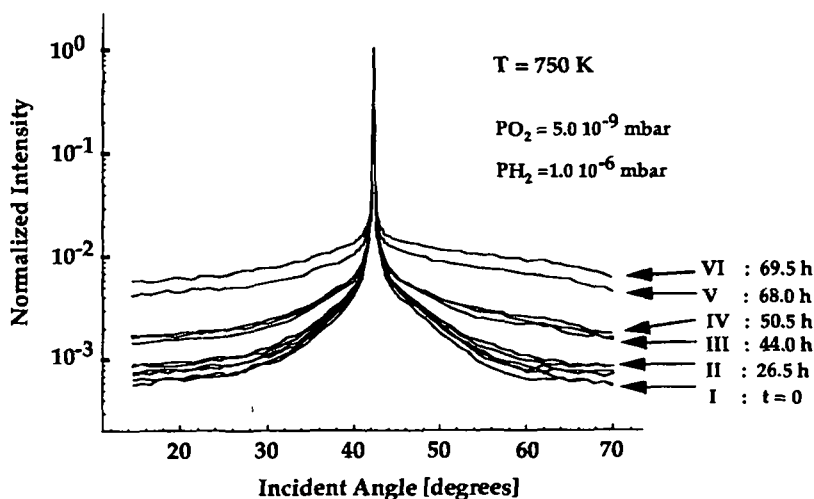


**Fig. 4.11:** Subsequent scans of a permanently cleaned Pt(111) surface at  $T = 750 \text{ K}$ . The hydrogen pressure accidentally dropped to  $1.0 \cdot 10^{-7} \text{ mbar}$  after 50.5 hours.

#### 4.6 Absolute efficiency of the Pt(997) echelette grating

In the preceding chapters it has been shown that the Pt(997) surface generally fulfils the basic requirements of a dispersive atom optical device. We will now discuss its efficiency, i.e. the amount of collected atoms within one higher diffraction order with respect to the incoming flux [Eff95]. It has already been discussed in Sec.2.1 that this efficiency should be several orders of magnitudes higher than for any low index surface of ionic or metallic crystals.

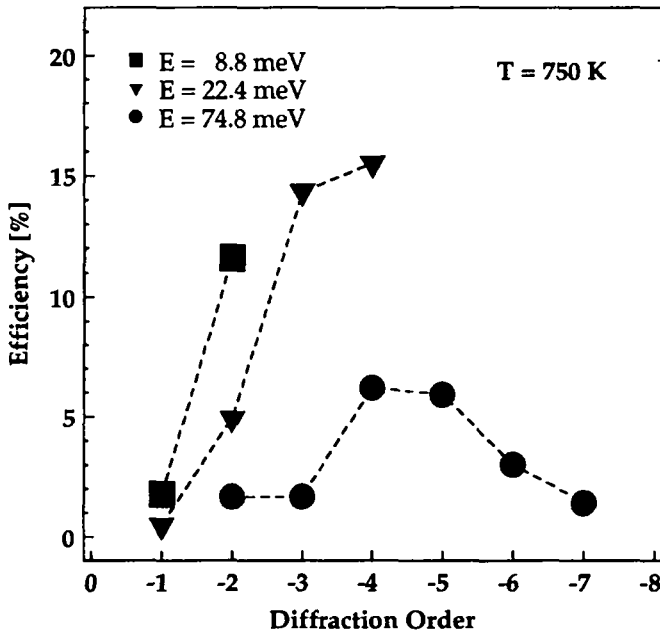


Fig. 4.12 : Absolute efficiencies of Pt(997) for diffraction under the ideal condition.

The experimental determination of the absolute efficiency has been possible due to the special construction of our apparatus, which allows for a direct scan of the primary beam. It therefore provides, to our knowledge, the first measurements of efficiencies of higher order He-diffraction using a highly monochromatic He-beam ( $\Delta\lambda/\lambda < 2\%$ ). The results are shown in Fig. 4.12 as a function of the diffraction order for three different beam energies and a fixed temperature of 750 K corresponding to the catalytic passivation of Pt(997). They were obtained by scanning subsequently the primary beam and the ideal diffraction orders. What is plotted in Fig. 4.12 is the ratio between the surface beneath the primary peak and the surface beneath the diffraction peaks and not the simple ratio between the peak maxima. The latter would give rise to too small values due to the dispersion smearing. In fact the ratio between the efficiencies determined by taking into account the surfaces beneath the peaks and by only taking into account the peak maxima varied between 2.5 for a 75 meV beam and 1.2 for a 8.8 meV beam which is in good agreement with the corresponding velocity spreads of 1.6 % and 0.8 %, respectively.

At beam energies of about 75 meV (filled circles) the efficiency has a maximum of about 6.5% at the fourth and fifth diffraction order. At beam energies of about 22 meV the efficiency, however, homogeneously increases giving rise to a maximum of about 16% at the fourth diffraction order. Note, that the fifth diffraction order can principally not be observed under the *ideal condition*. At beam energies of about 8.8 meV the efficiency varies between 3% and 12% for the first and second diffraction order. These values

are satisfying high<sup>1</sup> and they even justify the construction of a He-surface triple axis spectrometer with an additional Pt(997) monochromator beside the Pt(997) analyser, as it can be revealed from the discussion of the intensities in a triple axis spectrometer given in Sec. 2.1. The data of Fig. 4.12 also show the necessity of a correct choice of the working diffraction order, because already at constant beam energies the reflectivity can change by one order of magnitude when changing the diffraction order.

The data shown in Fig. 4.12 intuitively confirm the basic assumption that the Pt(997) under the *ideal condition* acts as almost perfect (dispersive) Pt(111) mirror. We will now make a closer inspection to get an idea to which extent the steps of the Pt(997) diminish the efficiency, and why the data obtained with a 75 meV beam show a maximum, whereas they do not at lower beam energies.

For this purpose, a rather crude model of the Pt(997) surface is introduced in Fig. 4.13. The surface consists of flat terraces which give only rise to forward specular scattering and step regions acting as perfect diffuse scatterers. In an early work Poelsema et al. measured a value of  $12\text{\AA}$  for the effective size of such a step region on Pt(111) [Poe89].

Within the model, diffraction into the specular direction of the (111) terraces will be limited by three reasons which can easily be quantified. First

---

<sup>1</sup> The data in Fig. 4.12 have been obtained from a well prepared Pt(997) surface that has been treated in the vacuum during several month. Nevertheless the quality of the surface continously increased during the proceeding months. We can now routinely obtain absolute reflectivities close to 20 % when working with a He- beam of about 20 meV. This improvement is most probably due to the permanent cleaning of the Pt(997) surface at 750K in a mixed hydrogen-oxygen atmosphere.

of all, the diffuse scattering step region Sst can be considered to be invisible for the He-beam which means a zero reflectivity of this part of the surface. Secondly, each step gives rise to a geometric shadowing effect making invisible for the He-beam a fraction of the adjacent terrace (Ssh). The larger the incident angle with respect to the (111) terrace the smaller is the specular scattered intensity.

The third contribution to the limitation of the diffraction intensity are inelastic scattering events. Their influence onto the intensity of diffraction peaks can be treated within the well known Debye-Waller formalism [Ash87] which -to a certain extent- also holds for He-atom scattering [Arm79, Lev81, Mey81].

$$I(T) = I_0 e^{-2W(T)} \quad (4.1)$$

$2W(T)$  is the temperature dependent Debye-Waller factor, which can be approximated for usual scattering geometries [Gar78] by

$$2W = \frac{3T(\hbar^2 \Delta k_z^2 + 8mD)}{Mk_b \Theta_D^2} \quad (4.2)$$

where  $\Delta k_z$  is the perpendicular scattering wave-vector transfer.  $D$  denotes the well depth of the He-surface potential and  $\Theta_D$  is an effective surface Debye-temperature.  $M$  and  $m$  are the masses of the Pt-atom and He-atom, respectively.

From equation (4.1) and (4.2) it can be concluded that the influence of inelastic scattering events is opposite to the shadowing effect mentioned before. An increasing incident angle (with respect to the (111) terrace) means a decreasing perpendicular momentum transfer and, thus, an increasing

intensity. It will be shown now that these two opposite trends can qualitatively and quantitatively explain the behaviour of the efficiency data of Fig. 4.12 .

For this we establish a simple formula for the diffracted intensity as a function of the incident angle  $\Phi$  with respect to the (111)-terraces.

$$I/I_0 \approx e^{-2W(\Delta k_z, D, \Theta_D)} * \frac{S - (S_{st} + S_{sh})}{S} * \frac{\cos(\Phi - 6.45^\circ)}{\cos(\Phi + 6.45^\circ)}, \quad (4.3)$$

It takes into account the shadowed region  $S_{sh} = \tan(\Phi) * h$  (h is the step height), the step region  $S_{st}$  and the momentum transfer  $\Delta k_z$ . S denotes the terrace width. The last term in equation (4.3) describes the effective illuminated area on the sample.

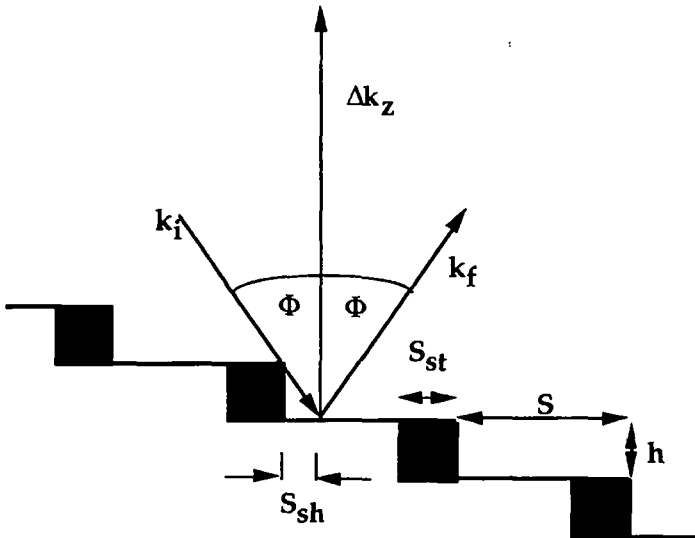
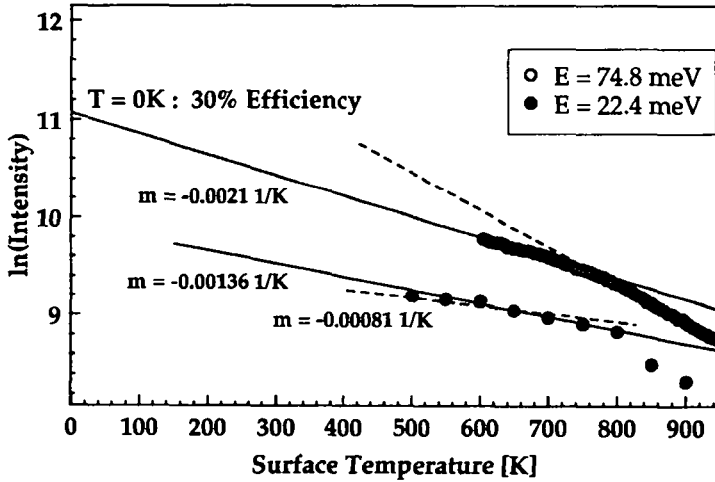


Fig. 4.13: Model of the Pt(997) surface.

In order to determine  $D$  and  $\Theta_D$  experimentally the  $n = -5$  diffraction order of a 75 meV beam has been measured at  $\Delta k_z = 13.8 \text{ \AA}^{-1}$  (*ideal condition*) as a function of the surface temperature. This is shown by the open circles in the logarithmic plot of Fig. 4.14. They show two linear regions separated by a kink at about 800K. This kink and the greater slope at temperatures above 800K is probably due to the onset of kink formation as a first step towards the facetting phase-transition of the Pt(997)-surface above 900K [Hah94]. Nevertheless at temperatures below 760 K a pure Debye-Waller scenario takes place and the data can be fitted by equation (4.1) and (4.2) (straight line). Next we measured the same temperature dependency with a 22.4 meV beam and a perpendicular momentum transfer of  $\Delta k_z = 8.3 \text{ \AA}^{-1}$  (*ideal condition*) at almost the same scattering geometry. This is shown by the filled circles in Fig. 4.14 (the y-axis scaling of Fig. 4.14 is not valuable for this data set). Again a dramatic change of the slope appears at about 800 K.

The two measured pairs consisting of  $\Delta k_z$  and the slope of the Debye-Waller fit (straight lines in Fig. 4.14) permit a preliminary determination of the well depth  $D$  and the surface Debye-temperature  $\Theta_D$  with the help of equation (4.2). The corresponding values are  $D = 42 \text{ meV}$  and  $\Theta_D = 426 \text{ K}$ . Although the value for  $D$  is surely too high, they can be compared to the values that have been observed for Pt(111) by a similar experiment done by Bortolani et al. [Bor88]. These authors reported a well depth of 12 meV and a surface Debye-temperature of 231K. Assuming that the Pt(997)-surface has the same Debye-temperature leads to the unphysical result of a positive well depth when independently fitting the two data sets of Fig. 4.14. Therefore the surface Debye temperature and in consequence the well depth of Pt(997) must be higher than for Pt(111). This agrees with the conception that the well depth increases as a function of the step density [Mec81]. The increased

Debye-temperature can be explained by a stiffening within the Pt(997)-surface due to the strong step-step interaction which has recently been deduced from a combined STM and He-diffraction study [Hah94].



**Fig 4.14:** Debye-Waller -measurements of the diffraction intensity into the terrace specular direction; open circles:  $\Delta k_z = 13.8 \text{ \AA}^{-1}$ , filled circles  $\Delta k_z = 8.3 \text{ \AA}^{-1}$ . The scaling of the y-axis is only valuable for the open circles.

Knowing  $D$  and  $\Theta_D$  equation (4.3) can be used to explain the efficiency data shown in Fig. 4.12. Fig. 4.15 a) shows the experimental data as a function of the terrace incident angle together with the simulation results. A constant proportionality factor has been chosen in such a way that the theoretical curve fits the efficiency of the fourth diffraction order at a beam energy of 75 meV. Therefore the theoretical curves (only) contain information about the relative changes of the efficiencies. Although the experimental values of  $D$



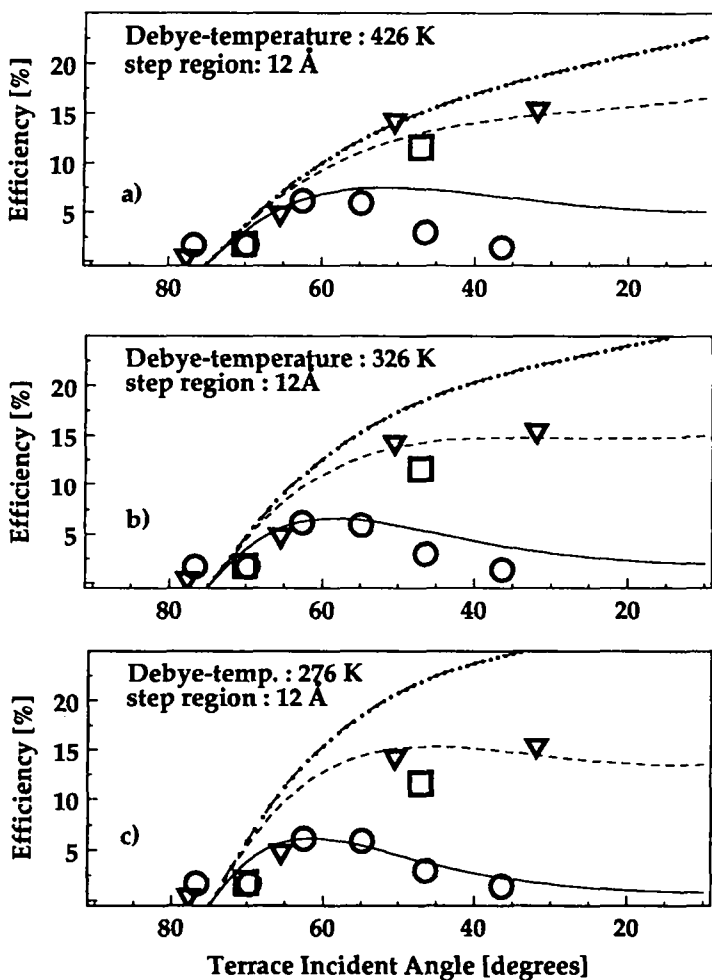


Fig. 4.15 : Experimental efficiency data compared to the results of the simulation using equation (4.3). The size of the step region was fixed to 12 Å; open circles / straight line:  $E = 74.8$  meV, open triangles / dashed line :  $E = 22.4$  meV, open squares / dashed-dotted line :  $E = 8.8$  meV . a)  $\Theta_D = 426$  K , b)  $\Theta_D = 326$  K , c)  $\Theta_D = 276$  K

and  $\Theta_D$  are too high the theoretically obtained curves of Fig. 4.15 a) confirm the main behaviour of the experimental data.

*At high beam energies the great perpendicular momentum transfer at small incident angles cancels out the intensity gain due to the decreasing shadowing effect. This gives rise to a maximum of the efficiency. On the other hand, at low beam energies the intensity losses are mainly dominated by the shadowing effect leading to a homogeneous increase of the efficiency with decreasing terrace incident angle.*

In regard of the simplicity of the model we did not carry out a real fit of the data. Nevertheless the model allows for a demonstration of the consequences of possible deviations of the well depth, the Debye-temperature, and the size of the step region. First the Debye temperature has been lowered by 100 K leading to the results shown in Fig. 4.15 b). The corresponding well depth  $D$  has been calculated with the help of the Debye-Waller-factor obtained from the first temperature dependent measurement shown in Fig. 4.14 (open circles,  $n = -5$ ,  $E = 74.8$  meV). The second data set of Fig. 4.14 (filled circles) has been neglected since it no more fits the new values of  $D$  and  $\Theta_{D,eff}$ . This will be justified below. The lowered Debye-temperature leads to a more pronounced maximum for the 75 meV beam energy in agreement with the experimental observation. Additionally, it weakens the efficiency increase at low beam energies, because inelastic scattering becomes more important. The curves describe surprisingly well the data except for the data obtained with the 8.8 meV-beam. A further lowering of the Debye-temperature by an amount of 50 K amplifies these changes as can be seen in Fig. 4.15 c). The 75 meV data are now well described and the 22 meV data still follow the theoretical curve, which now has also a maximum. Only the data obtained with the 8.8 meV beam do not

fit with the theoretical curve. This might be due to an increased step-cross-section for low energy atoms.

The well depth which results from a Debye-temperature of 276 K and the first data set of Fig. 4.14 (open circles,  $n = -5$ ,  $E = 74.8$  meV) is 14 meV. Thus, both the Debye-temperature and the well depth have reasonable values with respect to the values of Pt(111). They can be used to calculate the slope of the second data set in Fig. 4.14. As can be seen from the dashed line in Fig. 4.14, this new slope varies from the experimental data within the experimental error. This is justifying the above unilateral lowering of the Debye-temperature.

In Fig. 4.16 a)+b) the influence of the size of the step region is discussed at a fixed Debye-temperature of 276 K ( $D=14$  meV). A step size of 8 Å (Fig. 4.16 a)) shifts the efficiency maximum towards higher incident angles, whereas a 15 Å large step region results in a shift towards smaller incident angles (Fig. 4.16 b)). A 15 Å large step region is certainly unrealistic, because the efficiencies at low beam energies explode with respect to the values for the 75 meV beam.

The consequences of the catalytic passivation at  $T = 750$  K are discussed in Fig. 4.16 c) by plotting the theoretical predictions of the efficiency at  $T=165$  K. For this the theoretical curves of Fig.4.15 c), which fitted well the data at  $T = 750$ K have been recalculated with a surface temperature of  $T=165$  K. The low surface temperature leads to a vanishing of the maximum at high beam energies. This would allow for a wider range of angular settings of the analyser surface. Furthermore the efficiencies at  $T = 165$ K would be about a factor of 2 higher than at  $T = 750$  K. On the other, hand one full hydrogen monolayer on Pt(111) has a reflectivity, which is about 80 % of the reflectivity of the pure Pt(111) surface. Therefore it can be concluded, that

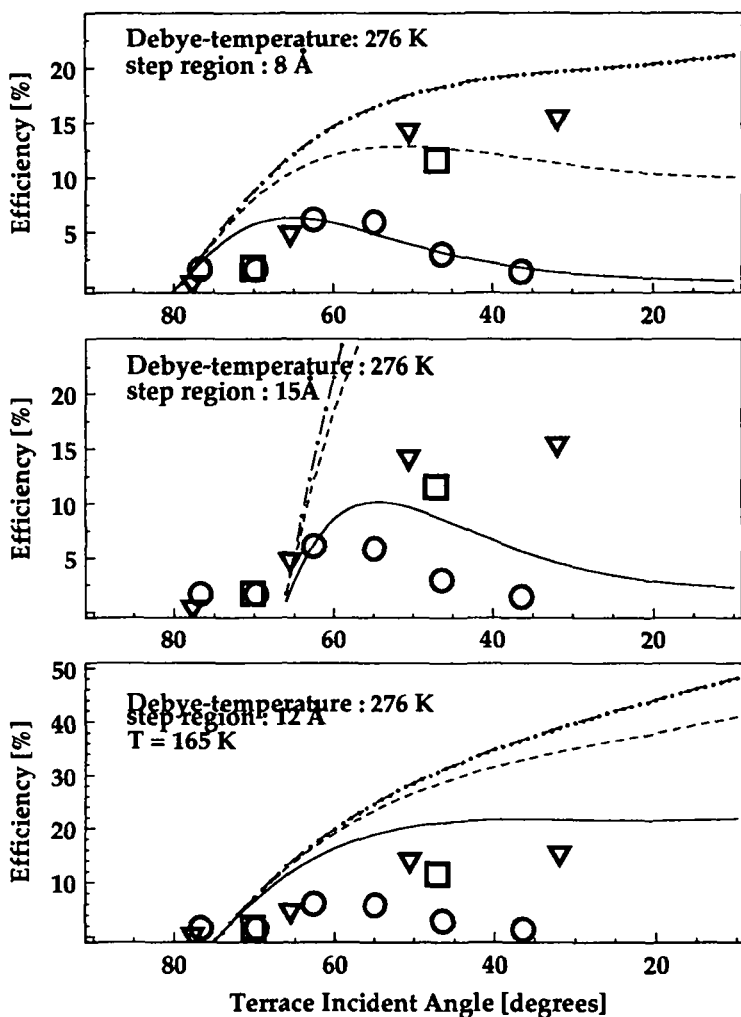


Fig. 4.16 : Experimental efficiency data compared to the results of the simulation using equation (4.3). The Debye-temperature is fixed to 276 K ( $D = 14$  meV); open circles / straight line:  $E = 74.8$  meV, open triangles / dashed line :  $E = 22.4$  meV, open squares / dashed-dotted line :  $E = 8.8$  meV .. a) step size : 8 Å , b) step size : 15 Å ; c)  $T = 165$  K , step size : 12 Å .

the adoption of the catalytic passivation causes an intensity loss of the order of 37 %.

Finally the absolute values of the efficiencies will be discussed. For this purpose the Debye-Waller fit of the data of Fig. 4.14 (open circles,  $n = -5$ ,  $E = 74.8$  meV) has been extrapolated to 0 Kelvin. By the way this provides a good test of the reliability of the absolute measurements, because the 0 K intensity must of course not be higher than the primary beam. The extrapolated efficiency at  $T = 0$  K is about 30% , which is in almost perfect agreement with the prediction of the above model. At zero temperature the Debye-Waller term vanishes and the efficiency is given by the ratio between the visible and non-visible region on the surface. This leads to an efficiency of about 25% for a step size of  $12 \text{ \AA}$  at the ideal condition of the fifth diffraction order of a 75 meV-beam.

In conclusion it can be stated, that the form factor of the Pt(997) surface can be separated into negligible step edge scattering and the dominating terrace scattering. This is not the case for most stepped surfaces with smaller step periodicities which have a corrugated He-surface potential [Lap92]. The Pt(997) surface therefore really corresponds to a blazed grating in light optics.

## **5 Monochromatization of supersonic He nozzle beams by diffraction**

So far the Pt(997) surface only acted as "passive" object of our investigations. Having established its properties with respect to helium atom diffraction we will now employ it as nanoscopic echelette grating for the active monochromatization of He-waves.

Apart from the pioneering work of Estermann, Frisch and Stern [Est31] in 1931 the experiments shown here are so far the only demonstration of active monochromatization of atomic de-Broglie waves by diffraction. Our double scattering experiment takes advantage of the high intensity of He nozzle beams and the high efficiency of nanoscopic echelette gratings; but the basic ideas are unchanged and the principal instructions for our experiments can already be found in the work of Estermann et al. [Est31].

### **Monochromatization by diffraction**

The basic idea of the experiment is shown in Fig. 5.1 a) which is directly taken from [Est31]. A polychromatic He-atom beam with a divergence defined by aperture 1 is first scattered off the monochromator surface. Atoms with different de-Broglie wavelengths are diffracted in different directions. Aperture 2, thus, skims an energy selected beam which is then analysed by diffraction from the second analyser surface.

Fig. 5.1 b) shows the experimental set-up used by Stern et al.. A so-called He-oven (Ofenraum) furnishes an effusive He-beam with a Maxwellian velocity distribution which is collimated by the aperture b and directed towards the LiF monochromator surface (K1). A small part of the scattered

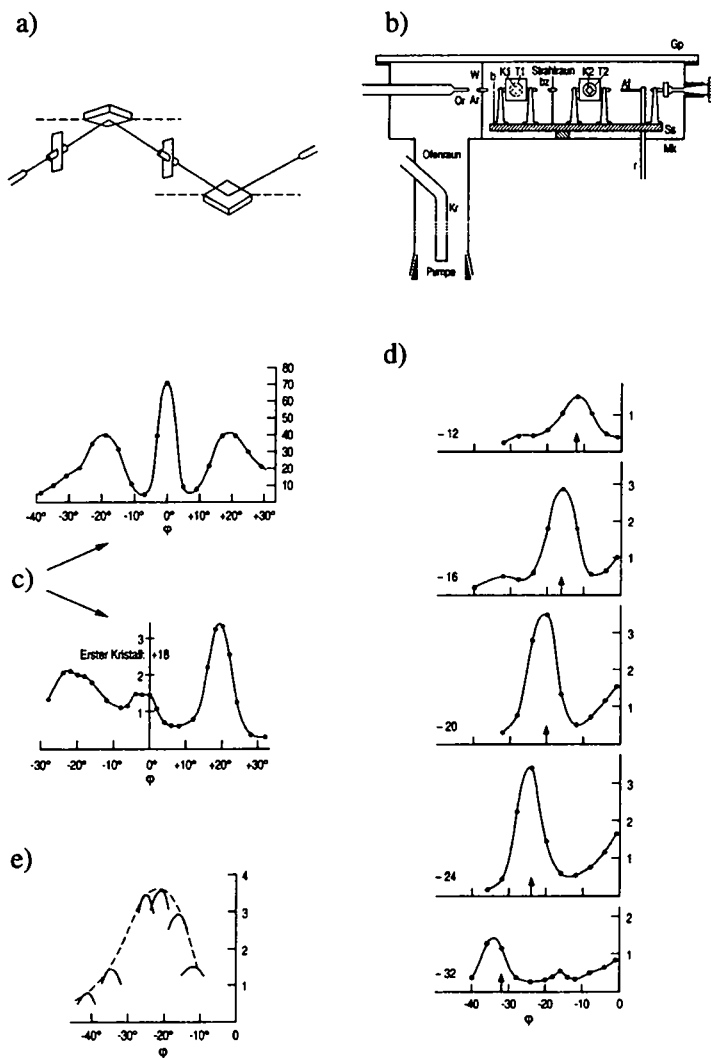


**Fig. 5.1 :** Aspects of the pioneering work of Stern and co-workers concerning the "Monochromatisierung der de Broglie-Wellen von Molekularstrahlen" : a) Schematic sketch of the experiment, b) design of their apparatus, c) demonstration of the monochromatization by the apparent diffraction peak narrowing, d) and e) scan of the incoming beam wavelength distribution by changing the monochromator angular position (see text).

beam is selected by the aperture  $bz$  before scattering from the LiF analyser surface (K2). Monochromatization is demonstrated by comparing diffraction spectra directly taken from the monochromator surface (upper curve in Fig. 5.1 c) ) with diffraction spectra taken from the analyser surface after having monochromatized the He-beam (lower curve in Fig. 5.1 c) ). Both curves were taken by rotating the crystal at an identical scattering geometry and can, thus, directly be compared. The peak at  $0^\circ$  is due to specular reflection, whereas the peaks at about  $\pm 20^\circ$  correspond to first order diffraction. The diffraction peaks of the lower curve are narrowed with respect to the upper curve which is nicely demonstrating the monochromatization.

From a philosophical point of view the measurements of Stern and collaborators contain a slight inconsistency, since an "absolute" proof of monochromatization would require the comparison of diffraction scans taken from the same surface. Proceeding in this way one has not to worry about morphological differences between the two surfaces which might also give rise to different diffraction patterns. Nevertheless, the peak widths and the changes of peak widths observed by Estermann et al. are without doubt determined by the large velocity spreads of the Maxwellian He-beams and its active monochromatization. This is, however, no more warranted in our case of highly monochromatic ( $\Delta\lambda/\lambda < 3\%$ ) supersonic nozzle beams where surface defects or mosaic spreads of the crystals can give rise to an extra-broadening that is greater than the dispersion smearing. We therefore compare in our experiment spectra taken from the analyser crystal with and without monochromatization. Additionally this allows the use of analyser surfaces that are different from the Pt(997) monochromator surface. We took advantage of this possibility by using a p(2\*2) O/Pt(111) analyser surface and a Pt(997) analyser surface.



Otherwise our experiments differed only in two more aspects from those of Stern and collaborators. Instead of being free to adjust any scattering geometry at the LiF monochromator, the *ideal condition* of the Pt(997) surface had to be fulfilled. This has been achieved in analogy to the measurements presented in Sec. 4.3 by stepwise changing the incident angle and searching for the minimum of the FWHM of the diffraction peak. Finally we took in-plane scans instead of out-of-plane scans as it has been done in [Est31].

Fig. 5.2 recalls the scattering geometry of our double surface scattering experiment. The size of the diaphragms  $d_2$  and  $d_3$  in front and behind the analyser surface have been fixed to 0.35 mm and 0.38 mm, respectively. The amount of the active monochromatization could be adjusted by varying the incoming beam divergence with the help of the variable diaphragm  $d_1$ .

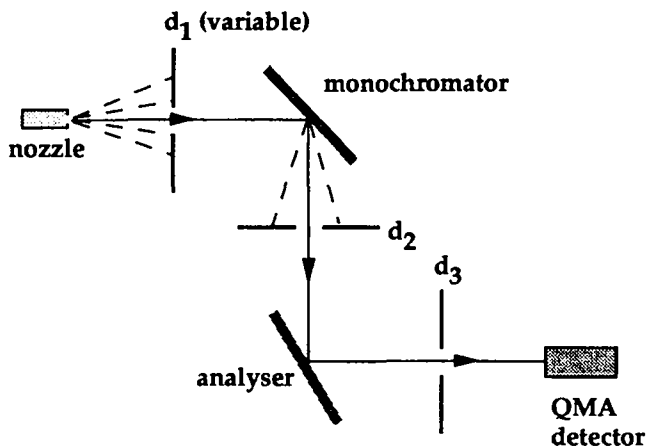


Fig. 5.2 : Scattering geometry of the double scattering monochromatization experiment.

## 5.1 Monochromatization demonstrated with a p(2\*2) O/Pt(111) analyser surface

Following the recipe given in Sec. 3.5 well ordered p(2\*2) oxygen overlayers have been grown on the Pt(111) surface which has been used as simple mirror-like "analyser "-surface during the early stages of the apparatus construction. The size of the diaphragm  $d_1$  in front of the monochromator was fixed giving rise to an incoming beam divergence of  $0.077^\circ$ . The corresponding theoretical monochromatization is of the order of  $\Delta\lambda/\lambda = 1\%$ , as it can be deduced from the normalized transmission function of the Pt(997) monochromator set-up shown in Fig. 5.3 a) (filled squares). The transmission has been calculated for a pass energy of 18.7 meV ( $\lambda = 1.05 \text{ \AA}$ ) at the  $n = -3$  diffraction order using the matrix-optics method. It can be characterized by the value  $\lambda_{\max} - \lambda_{\min}/\lambda_0$  which amounts to 1.6 % in the given example.  $\lambda_{\max}$  and  $\lambda_{\min}$  are the extreme wavelengths that are able to pass the aperture behind the monochromator. The straight line in Fig. 5.3 a) describes the wavelength distribution of a primary beam with  $\Delta\lambda/\lambda = 1.35\%$  (here  $\Delta\lambda$  is the FWHM). The wavelength distribution of the monochromatized beam that passes the slit diaphragm behind the monochromator is, thus, the product of the monochromator transmission multiplied by the incoming beam wavelength distribution. The result is shown by the dashed line indicating a distinct effective theoretical monochromatization. We therefore tried to monochromatize an incoming primary beam with  $\Delta\lambda/\lambda = 1.35\%$  that has been produced by running the 10  $\mu\text{m}$  nozzle source at 89.4 K and 22 bar. The filled rhombuses in Fig. 5.3 b) show the corresponding scattering angle diffraction scan from the Pt(997) monochromator at the *ideal condition* of the  $n = -3$  diffraction order. The

straight line in Fig. 5.3 b) is the fit to this data by means of the matrix-optics method.

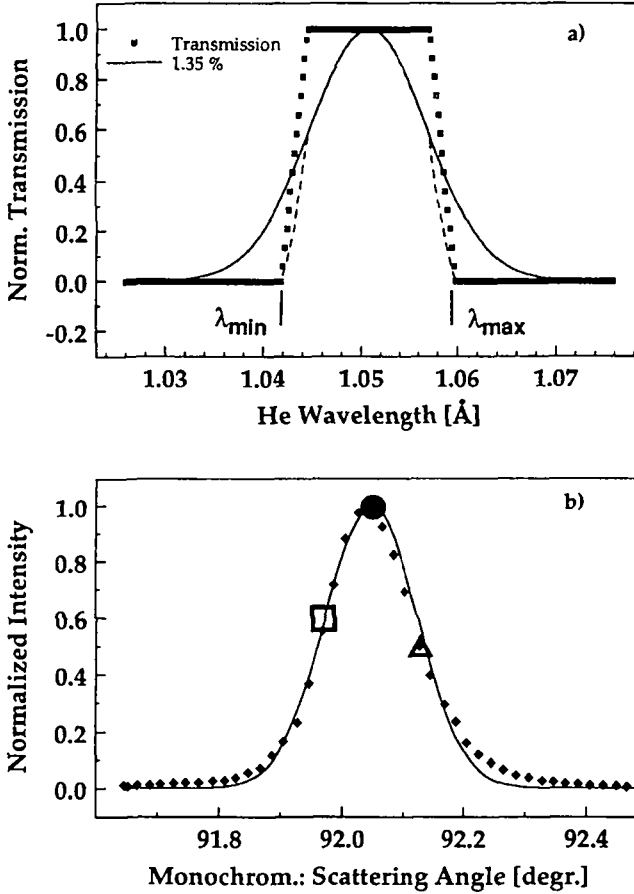


Fig. 5.3 : a) Monochromator transmission (filled squares) at the  $n = -3$  diffraction and a pass energy of 18.7 meV. The incoming beam wavelength distribution ( $\Delta\lambda/\lambda = 1.35\%$ ) is indicated by the straight line. b) Scattering angle scan from the monochromator showing the different monochromator angular positions used in the experiment (see text).

Fig. 5.4 shows the background corrected and normalized spectra obtained from the analyser diffraction taken with (filled circles) and without (open circles) monochromatization. As diffraction condition of the analyser we have used the (1/2,1/2) diffraction order of the p(2x2) oxygen overlayer on the Pt(111) surface. Background correction and normalization have been done by numerically fitting a Lorentzian superimposed on a constant background. The result of these fits are represented in Fig. 5.4 by the straight lines. The apparent monochromatization results in a pronounced reduction of the diffraction peak FWHM from  $0.160^\circ$  down to  $0.118^\circ$ , i.e. the FWHM is decreased by 26.3%. The observed monochromatization is in agreement with the theoretical prediction shown as dashed line in Fig. 5.3a).

We will now discuss a second instructive experiment performed in the original work of Estermann et. al.. They scanned the wavelength distribution of the incoming effusive He-beam by performing analyser scans at different monochromator angular positions. Fig. 5.1 d) shows such a series. The arrows indicate the corresponding monochromator angular positions. As expected, the maximum of the analyser diffraction scans are exactly located at the monochromator angular positions. Moreover, the maximum of each curve directly reflects the intensity of the incoming atoms with a wavelength according to the monochromator angular position. A plot of the maxima as a function of the monochromator position therefore confirms the Maxwellian velocity distribution of the incoming beam as it can be seen in Fig. 5.1 e).

In the following it will be demonstrated that similar effects can be made visible for supersonic nozzle beams with  $\Delta\lambda/\lambda < 2\%$ . For this purpose we did exactly the same experiment by performing analyser diffraction scans at three different monochromator angular positions. The monochromator

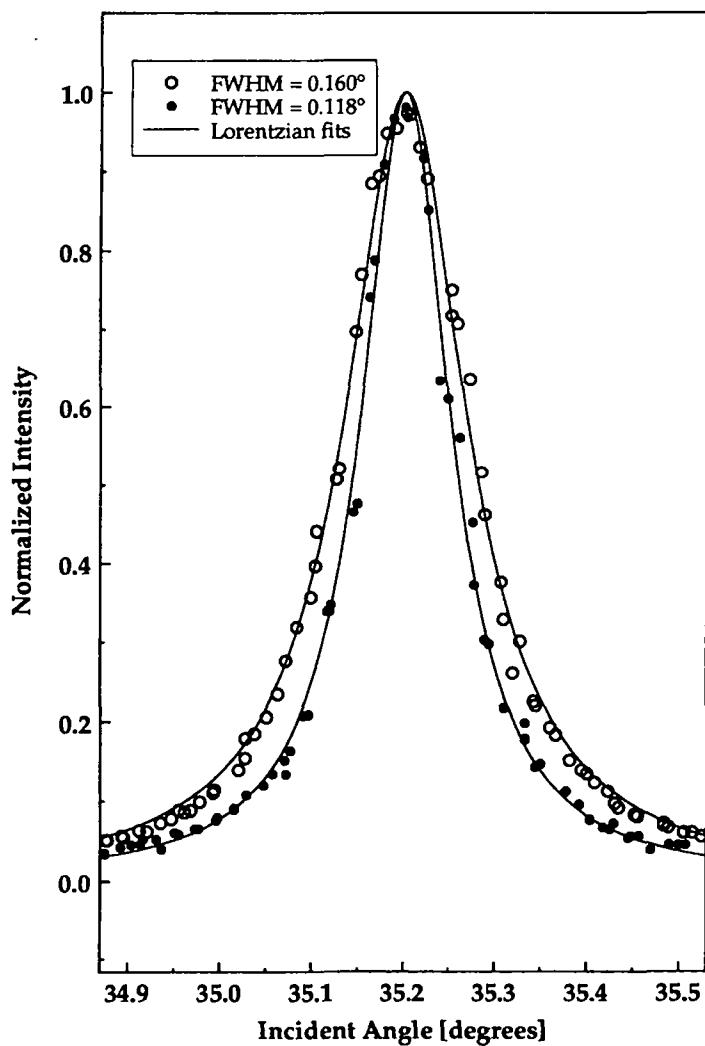


Fig. 5.4 : Comparison of analyser diffraction scans obtained by using a primary beam with  $\Delta\lambda/\lambda = 1.35\%$  with (filled circles) and without (open circles) monochromatization.

positions are indicated by the large filled circle, the large open square and the large open triangle in Fig. 5.3 b). They have been chosen to be in the peak maximum and near the half maximum positions that are shifted about  $\pm 0.08^\circ$  with respect to the peak maximum. The corresponding analyser scans are shown in Fig. 5.5 a) together with their Lorentzian fits. The central curve is identical to the "monochromatized" curve already shown in Fig. 5.4, whereas the two shifted curves correspond to the detuned monochromator angular position. Since we are using a positive diffraction order at the analyser surface, a lowered angle of incidence (open squares) corresponds to an increased wavelength and, thus, to a smaller scattering angle at the monochromator. The peak shift of the detuned scans with respect to the central curve is measured to be  $+0.04^\circ$  and  $-0.05^\circ$  corresponding to the wavelength shifts of  $-0.5\%$  and  $+0.7\%$ , respectively (see also the wavelength scaling of the x-axis of Fig. 5.5). The sum of these shifts almost perfectly agrees with the wavelength spread of  $\Delta\lambda/\lambda = 1.35\%$  of the incoming beam.

The FWHM of the analyser scans taken in the wings of the monochromator peak are about 10% broader than the FWHM of the scan taken in the *ideal condition* of the monochromator. This corresponds to an extra-broadening of about  $0.05^\circ$  due to the deviation from the *ideal condition* and is in agreement with the results shown in Sec. 4.3.

The above results can be confirmed by doing the complementary experiment. Instead of adjusting different monochromator positions and scanning the analyser one pre-selects distinct analyser positions and performs diffraction scans with the monochromator.

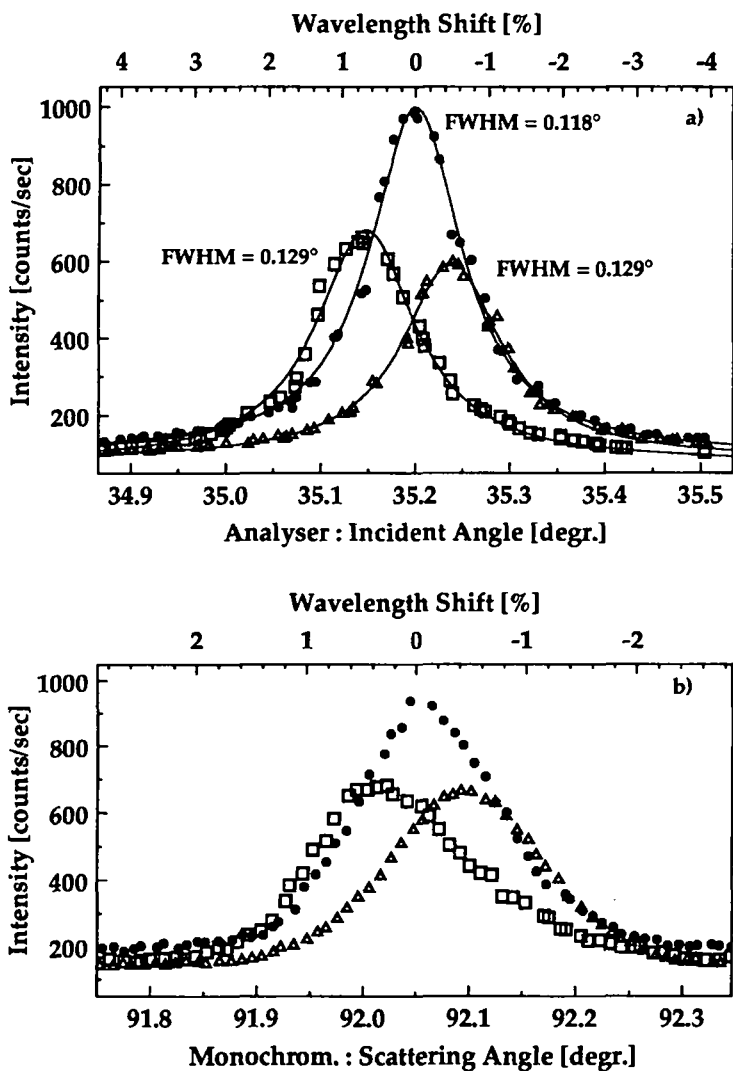


Fig. 5.5 : Demonstration of spatial wavelength separation by diffraction (primary beam:  $\Delta\lambda/\lambda = 1.35\%$ ) a) Analyser diffraction scans obtained at different monochromator positions, b) Scattering angle scans performed with different analyser angular settings. Identical symbols belong to corresponding measurements (see text).

We pre-selected the three peak maxima of the analyser scans of Fig. 5.5 a) and then performed the scattering angle scans with the monochromator as shown in Fig. 5.5 b). As expected the result is symmetric to the spectra shown in Fig. 5.5 a). Note the correspondence between the two data sets of Fig. 5.5 a) and b) : smaller incident angles at the analyser (positive diffraction order, open squares in Fig. 5.5 a) ) correspond to greater wavelength and, thus, are equivalent to smaller scattering angles at the monochromator (negative diffraction order, open squares in Fig. 5.5 b) ), and vice versa.

The results of Fig. 5.5 a) and b) are a direct proof of the real space separation of atoms with different wavelengths when diffracted from a surface. For monochromatization via diffraction this spectral shift is the necessary prerequisite. In order to explore the limits of the monochromatization furnished by the Pt(997) monochromator we repeated the measurements of Fig. 5.4 with a primary beam having a velocity spread of  $\Delta\lambda/\lambda = 0.7\%$ . Fig. 5.6 shows the corresponding scattering angle scan from the Pt(997) monochromator (filled rhombuses,  $\lambda = 1.038 \text{ \AA}$ ) together with the matrix-optics fit (straight line) confirming the wavelength spread of 0.7%. The monochromator positions used for the different analyser diffraction scans are again indicated by the large filled circle, the large open square and the large open triangle. The result of the analyser scans at the three different monochromator positions are shown in Fig. 5.7 a). The spectra characterising the detuned monochromator are still shifted with respect to the ideal diffraction angle, but the shift now only amounts to  $0.03^\circ$  in agreement with the reduced wavelength spread of the incoming beam. For the sake of completeness the complementary scans of the total scattering angle at the monochromator performed with the different analyser angular



settings, i.e. the peak maxima of Fig. 5.7 a), are shown in Fig. 5.7 b). They also exhibit the expected shifts.

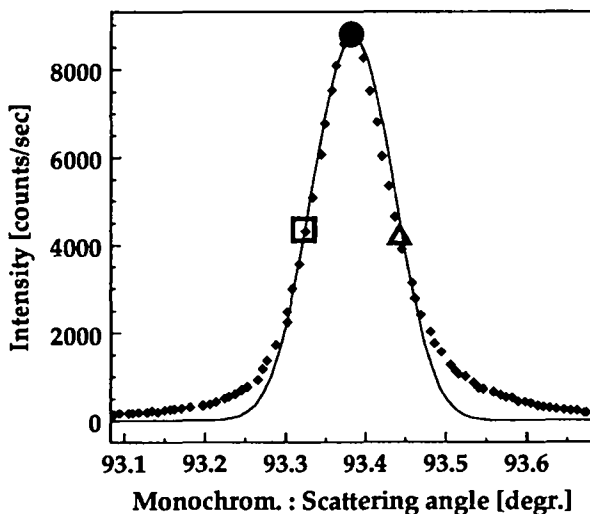


Fig. 5.6 : Scattering angle scan of the  $n = -3$  monochromator diffraction order obtained with a primary beam with  $\Delta\lambda/\lambda = 0.7\%$ . The different monochromator angular settings used in the experiment are indicated by the large symbols (see text).

(next page: Fig. 5.7) )

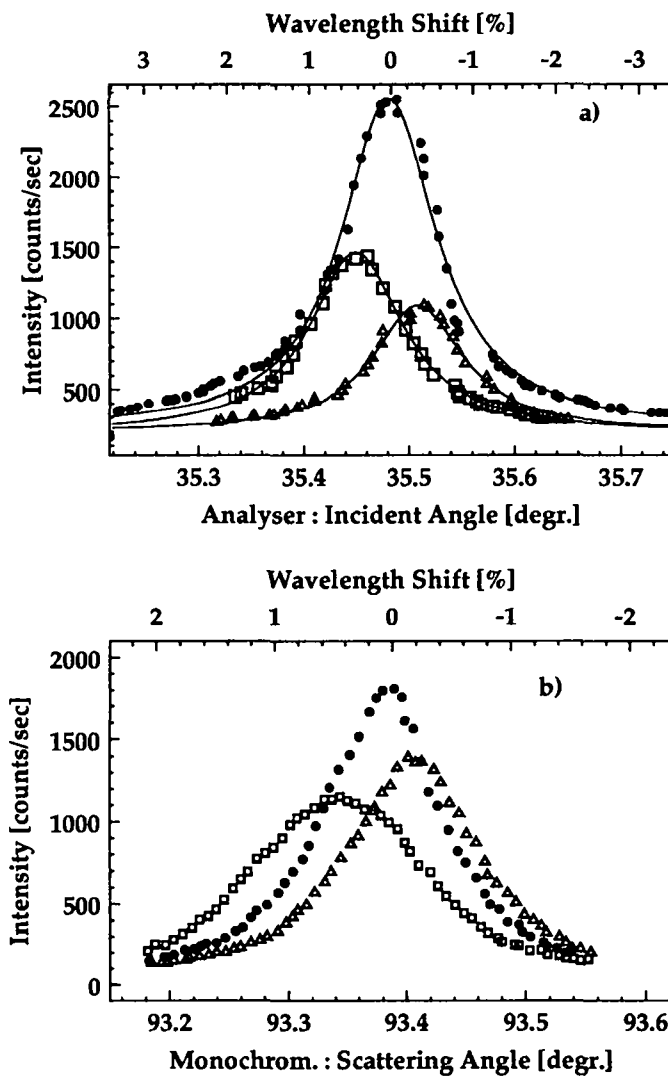


Fig. 5.7 : Demonstration of spatial wavelength separation by diffraction for a beam with  $\Delta\lambda/\lambda = 0.7\%$  a) Analyser diffraction scans obtained at different monochromator positions, b) Scattering angle scans performed with different analyser angular settings.

## 5.2 Monochromatization demonstrated with a Pt(997) analyser

In this chapter we discuss the results of the Pt(997) - Pt(997) double scattering experiment. Here the nanoscopic echelette grating has been used as monochromator and analyser. As primary beam we have used a He nozzle beam of wavelength spread  $\Delta\lambda/\lambda = 2.5\%$  which has been generated by using a 12 bar stagnation pressure at a nozzle temperature of 92 K ( $\lambda = 1.01 \text{ \AA}$ ). The incoming beam divergence has now been reduced to  $0.03^\circ$  giving rise to a monochromator transmission at the  $n = -3$  diffraction order characterised by  $\lambda_{\max} - \lambda_{\min}/\lambda = 0.84\%$  (filled squares in Fig. 5.8). The effective theoretical monochromatization is again the product of the monochromator transmission multiplied with the wavelength distribution of the incoming

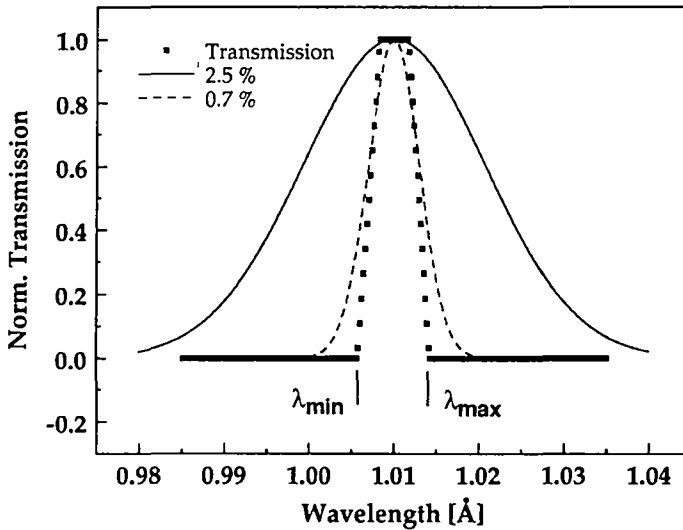


Fig. 5.8 : Monochromator transmission (filled squares) at the  $n = -3$  diffraction order and a pass energy of 19.1 meV. Incoming beam wavelength distributions with  $\Delta\lambda/\lambda = 2.5\%$  and  $0.7\%$  are indicated by the straight line and the dashed line, respectively.

beam (straight line in Fig. 5.8). Thus, the theoretical monochromaticity of the monochromatized beam is about  $\Delta\lambda/\lambda = 0.6 \%$ .

Fig. 5.9 shows the background corrected and normalized spectra obtained from the Pt(997) analyser with (filled circles) and without (open circles) monochromatization. The data have been fitted by a sum of a Gaussian and a Lorentzian in order to correctly describe the peak baseline. The monochromatization results again in a pronounced peak narrowing. Unfortunately, the analyser Pt(997) crystal (Pt(997)B) has a mosaic spread of about  $0.13^\circ$  (see below). Therefore the relative change of the FWHM is smaller than in the case of the above experiment using a  $p(2 \times 2)$  O/Pt(111) analyser surface. Nevertheless, the "monochromatized" curve can be compared to a spectrum that has directly been taken with a good He-beam with  $\Delta\lambda/\lambda = 0.7 \%$  (filled squares in Fig. 5.9). Surprisingly the "monochromatized" curve is broader than the curve directly obtained with a good primary beam of  $\Delta\lambda/\lambda = 0.7\%$ . In a naive view, according to the analysis in Fig. 5.8, we would have expected the inverse situation with the monochromatized spectrum narrower than the spectrum directly obtained with the good beam. In this simple model we have, however, ignored the influence of the double surface scattering of the He-beam. As will become clear below, the active monochromatization by scattering from a monochromator surface increases the "effective" beam divergence of the second scattering process at the analyser crystal resulting in an extra-broadening of the analyser diffraction. The FWHM of the analyser scans after active monochromatization is, thus, not a direct measure of the beam monochromaticity at the monochromator exit aperture.

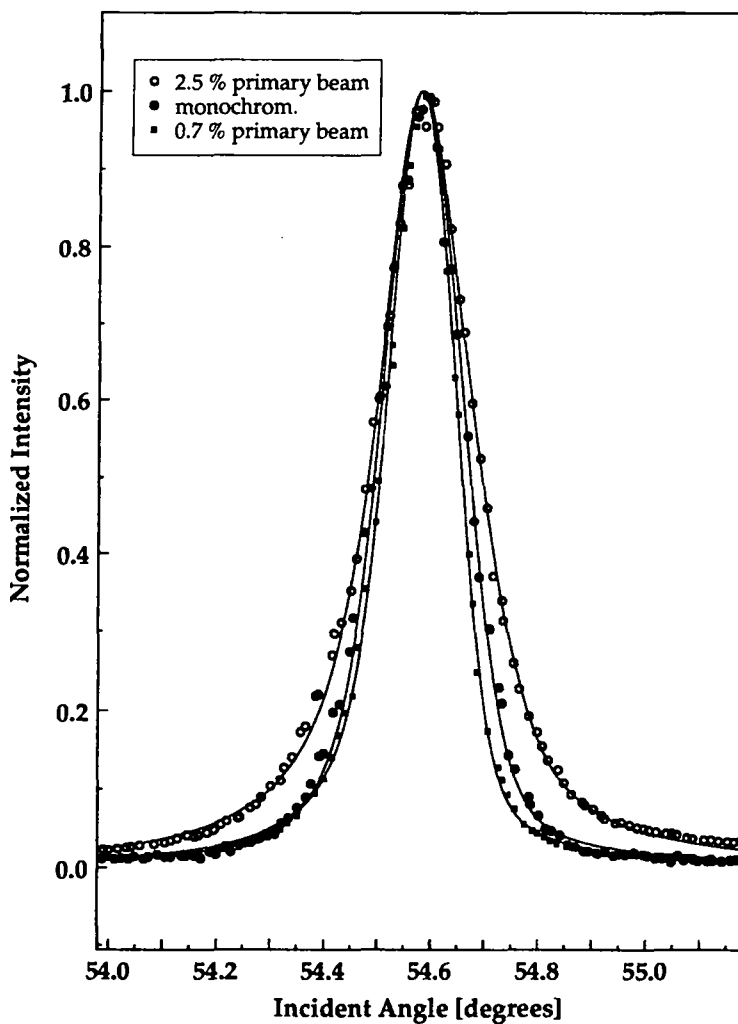


Fig. 5.9 : Comparison of analyser diffraction scans obtained by using a primary beam with  $\Delta\lambda/\lambda = 2.5\%$  with (filled circles) and without (open circles) monochromatization; filled squares: same diffraction scan directly obtained with a good beam with  $\Delta\lambda/\lambda = 0.7\%$ .

We have analysed the double surface scattering process with the help of the matrix-optics technique. The simulations shown in Fig. 5.10 directly correspond to the experimental situation discussed above (Fig. 5.9). The analyser diffraction peak under consideration has been calculated for a directly incoming beam with  $\Delta\lambda/\lambda = 2.5\%$  (open circles) and  $\Delta\lambda/\lambda = 0.7\%$  (filled small squares) and after monochromatization with the first echelette grating using a primary beam divergence of  $0.03^\circ$  (filled circles) and  $0.077^\circ$  (filled triangles). The simulation results are in agreement with the experimental observations.

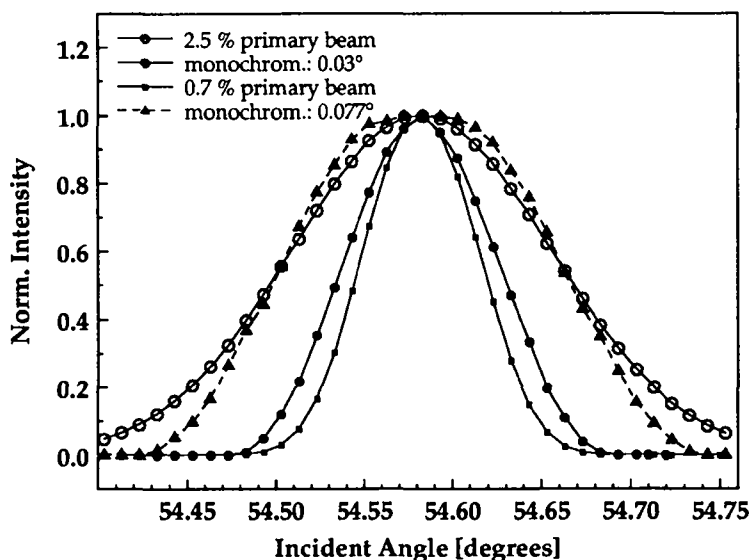


Fig. 5.10 : Simulations of the experimental diffraction peaks from Fig. 5.9; open circles : direct beam with  $\Delta\lambda/\lambda = 2.5\%$ , straight line : direct beam with  $\Delta\lambda/\lambda = 0.7\%$ , filled circles : monochromatized beam with incoming beam divergence of  $0.03^\circ$ , filled triangles : monochromatized beam with incoming beam divergence of  $0.077^\circ$ .

Although the theoretical monochromator set-up creates a highly monochromatized beam with  $\Delta\lambda/\lambda \approx 0.6\%$  the diffraction peak from the second Pt(997) surface remains broader than a diffraction peak directly taken with a beam with  $\Delta\lambda/\lambda = 0.7\%$ .

The explanation for this surprising result can be found by examining the double surface scattering geometry in more detail. In Sec. 2.4.1 the concept of virtual sources in diffraction has been introduced. It has been discussed that the diaphragm behind the surface "sees" an effective divergence given by equation (2.4.6). In the present case this effective divergence is greater than the divergence seen by the same diaphragm when it is located in the primary beam at a scattering angle of  $180^\circ$ . Therefore the peak narrowing due to the higher monochromaticity of the beam is cancelled out by the increased effective divergence of the monochromatized beam. The question whether or not monochromatization results in a peak narrowing depends on the delicate balance between the geometrical experimental arrangement and the amount of monochromatization. This is illustrated by the additional simulation (filled triangles in Fig. 5.10) of an analyser diffraction peak obtained after having monochromatized the same incoming beam with a beam divergence of  $0.077^\circ$ . Although the scattering process at the monochromator provides a monochromatized beam with  $\lambda_{\max} - \lambda_{\min}/\lambda_0 \approx 1.5\%$  no significant peak narrowing can be observed. Contrary the peak becomes even slightly broader in its central part.

The simulations of Fig. 5.10 can be used for a quantitative analysis of the experimental monochromatization results of Fig. 5.9. In addition to the geometric and dispersive peak broadening, the experimental spectra have also to be corrected for the mosaic spread of the analyser crystal. While the monochromator crystal has a mosaic spread far below  $0.05^\circ$ , the mosaic

spread of the analyser crystal is of the order of  $0.1^\circ$  and thus not negligible (see Sec. 4.4). In our analysis we assume that the peak broadening due to the mosaic spread adds to the geometric and dispersion peak broadening as if they were independent Gaussian contributions, allowing a straightforward deconvolution of the experimental data. Tab. 5.1 contains the FWHMs of the different experimental spectra and the FWHMs of the corresponding simulations. The mosaic spread has been determined by comparing the FWHMs of the experimental and simulated spectra that have been obtained with the good He-beam ( $\Delta\lambda/\lambda = 0.7\%$ ) without monochromatization (see the first row in Tab. 5.1). It amounts to  $0.13^\circ$ . Using this mosaic spread leads to the deconvoluted FWHMs of the experimental data shown in the last column of Tab. 5.1.

kind of diffraction scan	FWHM theoret. simulation	FWHM experiment	FWHM exp. deconvoluted
primary beam $\Delta\lambda/\lambda = 0.7\%$	<u>0.075°</u>	<u>0.151°</u>	<u>0.075°</u>
primary beam $\Delta\lambda/\lambda = 2.5\%$	0.172°	0.210°	0.165°
monochrom. $\Delta\lambda/\lambda = 2.5\%$	0.099°	0.178°	0.121°

**Tab. 5.1 :** Theoretical, experimental and deconvoluted experimental FWHMs of the  $n = -3$  analyser diffraction peak.

The deconvoluted experimental FWHMs and the theoretical values for the FWHMs agree within an error of  $0.02^\circ$ . This good agreement is a direct proof that the active monochromatization at the Pt(997) surface furnishes a highly



monochromatic beam with  $\Delta\lambda/\lambda \approx 0.6 \%$ , according to the product of the underlying transmission multiplied with the wavelength distribution of the primary beam (see Fig. 5.8).

In conclusion we have demonstrated that nanoscopic echelette gratings based on the vicinal Pt(997) surface allow a monochromatization of  $\Delta\lambda/\lambda = 0.6\%$  for He-beams. Since its use is not restricted to He-beams, they can generally be considered as molecular beam monochromators. Currently experiments are underway to demonstrate the monochromatization of D<sub>2</sub> molecular beams. The resolution of the nanoscopic echelette monochromator is limited by the finite mosaic spread and the mechanical precision of the diaphragm alignment. Experimental refinements and special crystal preparation methods (see Sec. 4.4, [San92]) should therefore permit an active monochromatization of the order of  $\Delta\lambda/\lambda = 0.1 \%$ .

## 6 Outlook

In this thesis vicinal stepped metal surfaces have been introduced as efficient nanoscopic echelette gratings for atomic and molecular beams. As a first step towards a systematical employment of these atom-optical devices within a surface double (triple) axis spectrometer they have been used for an active monochromatization of  $\Delta\lambda/\lambda = 0.6\%$  of He-waves. Experiments are currently underway to demonstrate the active monochromatization of  $D_2$  beams.

The systematical study of surface phonons with our He-surface double axis spectrometer has been hindered by time-limitations and the pronounced mosaic spread of the Pt(997)**B** crystal that has been mounted as analyser crystal. Pt(997)**B** will soon be replaced by Pt(997)**A** having a mosaic spread far below  $0.05^\circ$ . We will study the surface phonons of Cu(100) allowing a direct comparison with the former results from Mason and Williams [Mas81a, Mas81b] obtained by double axis spectrometry using LiF surfaces and the results obtained by the TOF method [Ben93].

A main focus of future applications of our double axis spectrometer will be the use of grazing incidence scattering conditions. For example, one might expect that grazing incidence can be used for a kind of atomic billiards where the impinging He-atoms cause single jumps of physisorbed rare gas atoms on a surface. Closely related to this is the study of frustrated translations of chemisorbed molecules whose excitation should also be favoured by grazing incidence scattering conditions.

A completely different application of our apparatus would be the study of the diffraction behaviour of different transmission gratings that are installed in the scattering chamber. Scanning the primary beam in the close vicinity of  $180^\circ$  should reveal the corresponding diffraction patterns. For example, we are interested in the question whether or not it is possible to see the diffraction pattern of a single slit. This could be used for a text-book like demonstration of Babinet's principle for atomic wave diffraction by studying the complementary diffraction from a thin wire having the same diameter as the single slit.

## 7 References

- [Ada94] C. S. Adams, M. Sigel and J. Mlynek, *Physis Report* 240, 143 (1994).
- [Aff94] C. Affentauschegg, diploma thesis, EPF Lausanne, Switzerland, 1994.
- [Als87] J. Als-Nielsen, *Structure and dynamics of surfaces II*, W. Schommers, P. Blanckenhagen, Eds., *Topics in Current Physics* 43 (Springer Verlag, Berlin-Heidelberg, 1987).
- [Ash87] N. Ashcroft, N. Mermin, *Solid State Physics* (HRW; 1987).
- [Azi91] R. A. Aziz and M. J. Slaman, *J. Chem. Phys.* 94, 8647 (1991).
- [Bar90] N. C. Bartelt, T. L. Einstein, and E. D. Williams, *Surf. Sci.* 240, L591 (1990).
- [Ben 93] G. Benedek, J. Ellis, N. Luo, A. Reichmuth, P. Ruggerone, and J. P. Toennies, *Phys. Rev. B* 48, 4917 (1993).
- [Ber75] S.L. Bernasek und G.A. Somorjai, *J. Chem. Phys.* 3149 (1975).
- [Ber78] Bergmann - Schaefer, *Lehrbuch der Experimentalphysik*, Bd. III, *Optik* (de Gruyter, 1978).
- [Ber87] S.L. Bernasek, K.L. Lenz, B. Poelsema, G. Comsa, *Surf. Sci.* 183 L319 (1987).
- [Ber89] R. Berndt, B.J. Hinch, J.P. Toennies und Ch. Wöll, *J. Chem. Phys.* 92 ,1435 (1889).
- [Bla95] M. Blanc, *travail de diplôme* , EPFL, (1995).
- [Bor88] V. Bortolani, V. Celli, A. Franchini, J. Idiodi, G. Santoro, K. Kern, B. Poelsema, and G. Comsa, *Surf. Sci.* 208, 1 (1988).

- [Bor89] V. Bortolani, A. Franchini, G. Santoro, J. P. Toennies, C. Wöll, G. Zhang, *Phys. Rev. B* 40 (1989) 3524.
- [Bre84] S. Brennan, P. Eisenberger, *Nucl. Instr. Meth.* 222A, 164 (1984).
- [Bru77] G. Brusdeylins, H. D. Meyer, J. P. Toennies and K. Winkelmann, *Rarefield Gas Dynamics*, 51, ed. J.L. Potter (AIAA, New York, 1977).
- [Bru81] G. Brusdeylins, R. B. Doak, and J. P. Toennies, *Phys. Rev. Lett.* 46, 437 (1981).
- [Bur87] E. Burkel, J. Peisl, and B. Dörner, *Europhys. Lett.* 3, 957 (1987).
- [Car91a] O. Carnal, M. Sigel, T. Sleator, H. Takuma, J. Mlynek, *Phys. Rev. Lett.* 67, 3231 (1991).
- [Car91b] O. Carnal and J. Mlynek, *Phys. Rev. Lett.* 66, 2689 (1991).
- [Car92] O. Carnal and J. Mlynek, *Europhys. News* 23, 149 (1992).
- [Com79a] G. Comsa, G. Mechttersheimer, B. Poelsema, S. Tomoda, *Surf. Sci.* 89, 123 (1979).
- [Com79b] G. Comsa, *Surf. Sci.* 81, 57 (1979)
- [Com80] G. Comsa, G. Mechttersheimer, and B. Poelsema, *Surf. Sci.* 97, L297 (1980).
- [Com82] G. Comsa, G. Mechttersheimer, B. Poelsema, *Surf. Sci.* 119, 159 + 172 (1982)
- [Com91] G. Comsa, private communication.
- [Dav86] R. David, K. Kern, P. Zeppenfeld and G. Comsa, *Rev. Sci. Instrum.* 57, 2771 (1986).
- [Doa81] R. B. Doak, (1981), Bericht 14/1981 Max-Planck-Institut für Strömungsforschung Göttingen (1981).

- [Doa89] R.B. Doak and D.B. Nguyen, in *Rarefied Gas Dynamics: Physical Phenomena* E. P. Muntz, D. B. Weaver and D. H. Campbell, Eds. (AIAA, Washington, DC, 1989).
- [Doa92] R. B. Doak, in: *Helium Atom Scattering from Surfaces*, ed. E. Hulpke, Springer Series in Surface Science 27, (Springer, Berlin-Heidelberg, 1992).
- [Eff95] especially in X-ray optics the term efficiency is used for a characterisation of diffractive optical elements, see for example:  
  
X-Ray Microscopy III, eds. A.G. Michette, G.R. Morrison, C.J. Buckley, Springer Series in optical sciences (Springer Berlin-Heidelberg, 1991)
- [Eng82] T. Engel and K. H. Rieder, Springer Tracts in modern Physics, 91 (Springer Verlag, Heidelberg-Berlin, 1982).
- [Est30] I. Estermann and O. Stern, Z. Phys. 61, 95 (1930).
- [Est31] I. Estermann, R. Frisch, and O. Stern, Z. Phys. 73, 348 (1931).
- [Ern93] A. Ernst, *Digitale Längen- und Winkelmesstechnik*, ed. (verlag moderne industrie AG, 1993).
- [Fis80] G.B. Fisher und J.L. Gland, in Surf. Sci. 94 , 446 (1980).
- [Fra91] T. Franke AG, Aalen (Germany)
- [Fre92] J. W. M. Frenken and B. J. Hinch, in Springer Series in Surface Science 27, ed. E. Hulpke, (Berlin-Heidelberg, 1992).
- [Gar78] N. Garcia, V. Celli, F.O. Goodman, Phys Rev. B 19 (1979), 634.
- [Haa74] P. Haasen, *Physical Metallurgy*, Cambridge University Press (Cambridge-London 1974).
- [Hah90] E. Hahn, Diplomarbeit, Universität Bonn, (1990).
- [Hah93] E. Hahn, A. Fricke, H. Röder, and K. Kern, Surf. Sci. 297, 19 (1993).

- [Hah94] E. Hahn, H. Schief, V. Marsico, A. Fricke, and K. Kern, Phys. Rev. Lett. 72, 3378 (1994).
- [Har82] J. Harris, A. Liebsch, G. Comsa, G. Mechttersheimer. B. Poelsema, S. Tomoda, Surf. Sci. 118 , 279 (1982) .
- [Hec90] E. Hecht, Optics (Adison Wesley, Reading, 1990).
- [Hei93] Dr. Johannes Heidenhain AG, Traunreut (Germany).
- [Hog88] D. Hoge, M. Tüshaus und A.M. Bradshaw, in Surf. Sci. 207, L935 (1988).
- [Hoi91] H. Hoinkes, in Springer Series in Surface Science 27. ed. E. Hulpke, Springer-Verlag (Berlin-Heidelberg, 1992)
- [Hul92] E. Hulpke, ed., Helium Atom Scattering from Surfaces, Springer Series in Surface Science 27 , (Springer-Verlag ,Berlin-Heidelberg, 1992).
- [Kei88] D. W. Keith, M. L. Schattenburg, H. I. Smith, and D. E. Pritchard, Phys. Rev. Lett. 61, 1580 (1988).
- [Kei91] D. W. Keith, C. R. Ekstrom, Q. A. Turchette, and D. E. Pritchard, Phys. Rev. Lett. 66, 2693 (1991).
- [Ker85] K. Kern, R. David, and G. Comsa, Rev. Sci. Instrum. 56, 369 (1985).
- [Ker86] K. Kern, R. David, R. L. Palmer, G. Comsa and S. Rahman, Phys. Rev. Lett. 56, 2064 (1986).
- [Ker89] K. Kern and G. Comsa, Adv. Chem Phys. 76 76, 211 (1989).
- [Kuh91] K. Kuhnke, Berichte des Forschungszentrums Jülich, Jül-2490 (1991)
- [Kuh92] K. Kuhnke, E. Hahn, R. David, P. Zeppenfeld, K. Kern, Surf. Sci. 272 , 118 (1992) .

- [Lah93] A. Lahee und J. P. Toennies, *Physics World*, April 1993, 61 (1993).
- [Lap81] J. Lapujoulade, *Surf. Sci.* 108, 526 (1981).
- [Lee83] J. Lee, J.P. Cowin und L. Wharton, *Surf. Sci.* 130 , 1 (1983) .
- [Leh82] S. Lehwald, H. Ibach and H. Steininger, *Surf. Sci.* 117, 342 (1982).
- [Len87] K. Lenz, Doktorarbeit Universität Bonn, F.R.G. (1987).
- [Liu91] Z.M. Liu, Y. Zhou, F. Solymosi und J.M. White, *Surf. Sci.* 245 , 289 (1991).
- [Luo93] F. Luo, G. C. McBane, G. Kim, C. F. Giese, and W. R. Gentry, *J. Chem. Phys.* 98, 3564 (1993).
- [Mar88] P. J. Martin, B. G. Oldaker, A. H. Miklich, D. E. Pritchard, *Phys. Rev. Lett.* 60, 515 (1988).
- [Mar95] V. E. Marsico, Ph. D. thesis, EPF Lausanne, Switzerland, in preparation.
- [Mas78] B. F. Mason and B. R. Williams, *Rev. Sci. Instrum.* 49, 897 (1978).
- [Mas81a] B. F. Mason and B. R. Williams, *J. Chem. Phys.* 75, 2199 (1981).
- [Mas81b] B. F. Mason and B. R. Williams, *Phys. Rev. Lett.* 46, 1138 (1981).
- [Mas83a] B. F. Mason and B. R. Williams, *Surf. Sci.* 130, 295 (1983).
- [Mas83b] B. F. Mason and B. R. Williams, *Surf. Sci.* 139, 173 (1983).
- [Mas84] B. F. Mason and B. R. Williams, *Surf. Sci.* 148, L686 (1984).
- [Mas86] B. F. Mason and B. R. Williams, *Surf. Sci.* 177, L925 (1986).
- [Meg91] Megatorque Inc., NSK Kugellager GmbH, Ratingen (Germany).



- [Mei88] C. v. d. Meijdenberg, in Atomic and molecular beam methods G. Scoles, Eds. (Oxford University Press, New York Oxford, 1988).
- [Mig88] J. J. d. Miguel, A. Cebollada, M. M. Gallego, J. Ferron, and S. Ferrer, *J. Cryst. Growth* 88, 442 (1988).
- [Mon83] D. E. Moncton and G. S. Brown, *Nucl. Instr. Meth.* 208 , 579 (1983).
- [Neu90] D. Neuhaus, *Phys. Rev. B* 41, 3397 (1990) .
- [Pfa93] T. Pfau, C. Kurtsiefer, C. S. Adams, M. Sigel, and J. Mlynek, *Phys. Rev. Lett.* 71, 3427 (1993).
- [Poe81] B. Poelsema, G. Mechttersheimer, and G. Comsa, *Surf. Sci.* 111, 519 (1981).
- [Poe82a] B. Poelsema, R. L. Palmer, G. Mechttersheimer, and G. Comsa, *Surf. Sci.* 117, 50 (1982).
- Poe82b] B. Poelsema, S. T. d. Zwart und G. Comsa, *Phys. Rev. Lett.* 49 , 578 (1982).
- [Poe86] B. Poelsema, L.S. Brown, K. Lenz, L.K. Verheij und G. Comsa, *Surf. Sci.* 171 , L395 (1986).
- [Poe89] B. Poelsema and G. Comsa, in *Springer Tracts in Modern Physics* (Springer Verlag, Berlin-Heidelberg, 1989).
- [Rie92] K.-H. Rieder, *Springer Series in Surface Science* 27, E. Hulpke, Eds. (Springer, Berlin, Heidelberg, 1992).
- [Rob86] I.K. Robinson, *J. Vac. Techn. A4*, 1311 (1986).
- [San92] A. R. Sandy et al., *Phys. Rev. Lett.* 68 , 2192 (1992).
- [Sch94] W. Schöllkopf and J. P. Toennies, *Science* 266, 1345 (1994).

- [Sch95] J. Schmiedmayer, M.S. Chapmann, C.R. Ekstrom, T.D. Hammond, S. Wehinger, D.E. Pritchard , Phys. Rev. Lett. 74, 1043 (1995).
- [Sco88] G. Scoles, Atomic and Molecular Beam Methods (Oxford University Press, New York oxford, 1988).
- [Smi88] D.-M. Smilgies and J.P. Toennies, Rev. Sci. Instrum. 59, 2185 (1988).
- [Toe87] J. P. Toennies, in Surface Phonons, W. Kress and F. W. d. Wette, Eds., Springer Series in Surface Science 21 (Springer, Berlin-Heidelberg, 1987).
- [Wan88] J. W. Wang, V. A. Shamamian, B. R. Thomas, J. M. Wilkinson, J. Riley, C. F. Giese, and W. R. Gentry, Phys. Rev. Lett. 60, 696 (1988).
- [Wit95] G. Witte, J.Braun, A. Lock, J.P. Toennies, submitted Phys. Rev.B
- [Zan88] A. Zangwill, Physics at surfaces, ed. (Cambridge University Press, Cambridge,1988).



## Appendix A

Important apparatus parameters:

### Distances:

source - target : 753 mm  
target - analyser : 763 - 863 mm  
analyser - detector : 261 mm

### Angles:

Total scattering angle at the target :  $59^\circ - 181^\circ$   
Max. Rotation of the scattering chamber :  $\pm 30.5^\circ$

### Pressures and pumping equipment:

Table 1. pumping stage data

Pumping Stage	Pump Type	Pumping Speed	Background Pressure	Operating Pressure
0 (nozzle)	-	-	-	240 bar
1 (source chamber)	diffusion	6,000 L/s	$10^{-7}$ mbar	$5 \cdot 10^{-4}$ mbar
2 (pumping stage)	turbo	150 L/s	$5 \cdot 10^{-8}$ mbar	$10^{-6}$ mbar
3 (pumping stage)	turbo	150 L/s	$1 \cdot 10^{-9}$ mbar	$10^{-8}$ mbar
4 (scattering chamber)	turbo	340 L/s	$2 \cdot 10^{-10}$ mbar	$6 \cdot 10^{-10}$ mbar
5 (pumping stage)	turbo	140 L/s	$10^{-10}$ mbar	$10^{-10}$ mbar
6 (analyser chamber)	turbo	340 L/s	$10^{-10}$ mbar	$10^{-10}$ mbar
7 (mass spec.)	turbo	380 L/s	$10^{-10}$ mbar	$10^{-10}$ mbar



## Remerciement

Merci beaucoup a tous ceux qui ont contribué à l'élaboration de cette thèse:

au Prof. K. Kern pour m'avoir donné l'occasion de réaliser le travail présent, pour son engagement et les multiples discussions indiquant les points essentiels d'une façon claire et nette;

à K. Kuhnke pour son aide en ce qui concerne quelques aspects théoriques de ce travail;

à Ph. Cordey, C.-L. Bandelier, A. Guisolan et tous les collaborateurs des ateliers de mécanique et d'électronique pour leur précieuse contribution;

à Vittorio Marsico - mon collègue au laboratoire et "prof de français" - pour une collaboration fructueuse profitant en plus de son immense patience face aux travaux mécaniques de précision et ses connaissances extraordinaires sur l'ordinateur;

à tous ceux qui ne sont pas mentionnés ici par nom, surtout mes parents et toute ma famille qui m'a accompagné durant mes études avec intérêt et soutien.



## Curriculum Vitae

Nom: **Hansjörg Schief**  
Adresse: Ch. de Mallieu 9  
CH-1009 Pully  
Suisse

Date de naissance : 30. Septembre 1963  
Lieu de naissance : Tübingen (Allemagne)  
Situation de famille: marié, 2 enfants  
Nationalité : allemande

### Formation

Ecole primaire : 1970 -1974 Reutlingen (Allemagne)  
Gymnase : 1974-1983 Baccalauréat général

Service civile 1983 - 1984 Reutlingen

### Etudes

1984 -1987 Université de Tübingen  
1987 - 1990 Université de Göttingen  
travail de diplôme : 1988 - 1990 Max-Planck-Institut für Strömungs Forschung (Prof. J.P. Toennies)  
Sujet : Physique de surface, croissance des couches minces métalliques

Doctorat 1991 Université de München  
1991 - 1995 Ecole Polytechnique Fédérale de Lausanne (EPFL), sous la direction du Prof. K.Kern







